

INFORMATION TO USERS

This manuscript has been reproduced from the microfilm master. UMI films the text directly from the original or copy submitted. Thus, some thesis and dissertation copies are in typewriter face, while others may be from any type of computer printer.

The quality of this reproduction is dependent upon the quality of the copy submitted. Broken or indistinct print, colored or poor quality illustrations and photographs, print bleedthrough, substandard margins, and improper alignment can adversely affect reproduction.

In the unlikely event that the author did not send UMI a complete manuscript and there are missing pages, these will be noted. Also, if unauthorized copyright material had to be removed, a note will indicate the deletion.

Oversize materials (e.g., maps, drawings, charts) are reproduced by sectioning the original, beginning at the upper left-hand corner and continuing from left to right in equal sections with small overlaps. Each original is also photographed in one exposure and is included in reduced form at the back of the book.

Photographs included in the original manuscript have been reproduced xerographically in this copy. Higher quality 6" x 9" black and white photographic prints are available for any photographs or illustrations appearing in this copy for an additional charge. Contact UMI directly to order.

U·M·I

University Microfilms International
A Bell & Howell Information Company
300 North Zeeb Road, Ann Arbor, MI 48106-1346 USA
313/761-4700 800/521-0600

Order Number 9331353

**The astrophysical S-factor of $^{12}\text{C}(\alpha, \gamma)^{16}\text{O}$ from the beta-delayed
alpha-particle emission of ^{16}N**

Zhao, Zhiping, Ph.D.

Yale University, 1993

U·M·I

300 N. Zeeb Rd.
Ann Arbor, MI 48106

**THE ASTROPHYSICAL S-FACTOR OF $^{12}\text{C}(\alpha, \gamma)^{16}\text{O}$
FROM
THE BETA-DELAYED ALPHA-PARTICLE EMISSION OF ^{16}N**

A Dissertation
Presented to the Faculty of the Graduate School
of
Yale University
in Candidacy for the Degree of
Doctor of Philosophy

by
Zhiping Zhao
May, 1993

ABSTRACT

THE ASTROPHYSICAL S-FACTOR OF $^{12}\text{C}(\alpha, \gamma)^{16}\text{O}$ FROM THE BETA-DELAYED ALPHA-PARTICLE EMISSION OF ^{16}N

Zhiping Zhao
Yale University
1993

Helium burning plays a key role in both the formation of heavy elements and the collapse of massive stars. The result of the helium burning—the $^{12}\text{C}/^{16}\text{O}$ ratio, determines the abundance of heavy elements and the dynamics of a massive star at its final stages before a supernova explosion.

One of the two reactions in the helium burning process, the $^{12}\text{C}(\alpha, \gamma)^{16}\text{O}$ capture reaction, is poorly understood despite intense theoretical and experimental work during the last two decades. The previously extracted p-wave ‘S-factor’ for the $^{12}\text{C}(\alpha, \gamma)^{16}\text{O}$ capture reaction at 300 keV ($S_{E1}(300)$) ranges in value from 0 to 500 keV-barn. On the other hand, the beta-delayed alpha-particle emission spectrum at low energy provides a very sensitive means to determine the reduced alpha-particle width of the bound 1^- state, hence the ‘S-factor’.

The spectrum of low energy beta-delayed alpha-particle emission of ^{16}N , was measured with high sensitivity; e.g., at $E_{\alpha}^L \approx 1$ MeV a sensitivity for a beta-decay branching ratio in the range of 10^{-9} (to 10^{-10}) was achieved. The branching ratio and spectrum of beta-decay of ^{16}N to the relevant broad 1^- resonance were remeasured. The alpha-particle spectra were unfolded to remove effects of finite

energy resolution (foil thickness).

We used previous theoretical work of Ji, Filippone, Humblet and Koonin to extract from these data the astrophysical E1 S-factor for the $^{12}\text{C}(\alpha, \gamma)^{16}\text{O}$ capture reaction and find $S_{E1}(300) = 95 \pm 6$ (stat) ± 28 (syst) keV-barn.

ACKNOWLEDGEMENT

The completion of this thesis was not possible without the help and support of many colleagues and friends.

I thank my thesis committee members and the outside reader: Professors Tom Applequist, Sam Austin, Frank Firk, Moshe Gai, Peter Paker and Mike Zeller for their valuable comments. I thank professor Xiangdong Ji for discussions and providing me the computer programs used for R-matrix fitting.

I am very grateful to have the opportunity to work with Professor Moshe Gai. He has been my thesis adviser for seven years. I thank him for his guidance and patience. I learned a lot of physics from him. It was a great pleasure to work with my colleagues: Ralph France, Steve Rugari and Ed Wilds. I am mostly indebted to Ralph France, who took most of the graveyard shifts while I was taking many weeks of the beam time. I thank Brian Lund and Sumit Sen for their help in the early stages of the experiment.

I thank Professor Peter Parker for his support and encouragement during my stay at Yale, for physics discussions and help. I thank Dr. D.A. Bromley for his support. I enjoyed the discussions with my colleagues at the Wright Nuclear Physics Laboratory, and appreciated all kind of the help they gave me, they are: Dan Blumenthal, Charles Bockelman, Felix Chan, Amir Chishti, Partha Chowdhury, Ben Crowell, Pat Ennis, Joe Germani, Vicki Greene, Kevin Hahn, Al Howard, Richard Hyder, Shiva Kumar, Kim Lister, Craig Levin, Heping Li, Brian Lund, Bernard Philips, Sumit Sen, Sinan Utku.

I thank the staff at the Wright Nuclear Structure Laboratory and the physics department for their help, they are: Jeff Ashenfelter, Tom Barker, John Barris, Sara Batter, Jean Belfonti, Dee Berenda, Rita Bonito, Joe Cimino, Phil Clarkin, Lisa Close, Karen DeFelice, Teddy Duda, Sam Ezeokoli, Walter Garnett, Bob Hamburger, Al Jeddry, Tom Leonard, Bob McGrath, Allen Ouellette, Kenzo Sato, Bill Schief, Mary Anne Schulz, and Dick Wagner.

I thank J.Z. Zhang for developing the method and making targets for me. Very often he had to work in the evenings and weekends to meet my time schedule. I thank Don Mcduff and K.S. Lai for their help in measuring the target properties.

Contents

1 INTRODUCTION	1
1.1 NUCLEOSYNTHESIS	1
1.2 HELIUM BURNING IN MASSIVE STARS	6
2 THEORY	19
2.1 THERMONUCLEAR REACTION RATE	19
2.2 R MATRIX PARAMETRIZATION OF THE $^{12}\text{C}(\alpha, \gamma)^{16}\text{O}$ REAC- TION	20
3 THE EXPERIMENTS	29
3.1 EXPERIMENTS AT YALE UNIVERSITY: The Beta-Delayed Alpha- Particle Emission of ^{16}N	29
3.1.1 EXPERIMENTAL PROCEDURES	30
3.1.2 TARGET PREPARATION	43
3.1.3 EXPERIMENTAL RESULTS	47

3.2	THE EXPERIMENT AT MSU: Precision Measurement Of Beta-delayed Alpha-particle Emission Of ^{16}N To The Broad 1^- State At 9.6 Mev in ^{18}O	67
3.2.1	EXPERIMENTAL PROCEDURES	68
3.2.2	EXPERIMENTAL RESULTS	75
4	EXTRACTION OF THE ASTROPHYSICAL S-FACTOR	82
4.1	UNFOLDING OF THE DATA	82
4.2	R-MATRIX ANALYSIS	94
5	CONCLUSIONS	104
	APPENDIX A	108
	REFERENCES	113

List of Figures

- 1 The evolution of a 25 solar mass star. The burning of hydrogen, helium, carbon, neon, oxygen and silicon yields an onion-shell structure, with Fe central core and shells of mixture of products of various burning stage (Figure taken from [Be85]). 3
- 2 Simplified level scheme for the triple alpha-particle capture reaction (not drawn to scale), the reaction rate is uniquely determined by the width of the resonances and mass differences. 7
- 3 Simplified level scheme for the alpha-particle radiative capture by carbon nuclei (not drawn to scale). The reaction rate is determined by the reduced alpha-particle widths (γ_α^2) of the two subthreshold states at 6.92 MeV and 7.12 MeV. 8
- 4 The extrapolated values of $S_{E1}(300)$ as obtained by various experimental groups over the last two decades (Figure taken from [Ou92]). 11
- 5 Simplified level scheme for the radiative capture of alpha-particles by ^{12}C and the beta-delayed alpha-particle emission (not drawn to scale). The most significant contribution to the astrophysical cross section of $^{12}\text{C}(\alpha, \gamma)^{16}\text{O}$ reaction is from the bound 1^- state at 7.12 MeV. 16

6	The p wave β -delayed α -particle decay spectrum of ^{16}N , predicted by Ji et al. [Ji90]. The solid curve is calculated with the best-fit parameters and $S_{E1}(300)=130$ keV-barn($A_3=0$), and dashed curve with $S_{E1}(300)=90$ keV-barn($A_3 = -7,000$ MeV $^{1/2}$). Figure taken from [Ji90].	17
7	The β -delayed α -particle decay spectrum of ^{16}N from K -matrix analysis, (Figure taken from [Hu91]).	17
8	The beta-delayed alpha-particle emission spectra from microscopic calculation. The predicted yield for a reduced alpha-particle width [i.e. $S_{E1}(300)$] varied by a factor of 2 is shown. Note the scale of the predicted branching ratio, on the order of 10^{-9} . (Figure taken from [Ba88]).	18
9	Schematic diagrams of experimental setup used for the Yale experiment.	31
10	Singles alpha-particles spectrum with beam chopper on (upper panel), and beam chopper off (lower panel).	33
11	Typical range and straggling calculations for recoil ^{16}N nuclei in our target.	35

12	Time resolution for alpha-particles from ^{228}Th source, with a telescope consisting of a Si detector ($25\mu\text{m}$, 25mm^2) and a micro-channel plate assembly (upper panel). The alpha-particle energy deposited in Si detector is shown in lower panel.	38
13	Schematics of Electronics, with nine identical Si detector channels and twelve identical beta-particle detector channels.(Canberra 2003BT≡preamplifier, CFD≡Constant Fraction Discriminator, AD811≡ADC, GG8000≡Gate and Delay Generator.)	41
14	Typical charged particle spectrum from $^{10}\text{B}(n, \alpha)^7\text{Li}^*$ reaction. Fast neutrons, from a Pu-Be neutron source, were thermalized using paraffin, and react with isotopically enriched $^{10}\text{B}_2\text{O}_3$	42
15	The excitation function of the $^{15}\text{N}(p, \alpha\gamma)^{12}\text{C}$ reaction using our Ti^{15}N target. The top panel was measured before the target was exposed to the beam and the lower panel after it was exposed to an integrated beam dose of 1 Coulomb of 9 MeV deuterium. . . .	46
16	Singles alpha-particle spectrum. The peak around channel 20 corresponds to the decay of broad 1^- state at 9.6 MeV and the low energy structure is due to energy deposited by beta-particles. The cutoff at channel 5 is the electronics threshold.	48

17	Beta-delayed alpha-particle spectrum constructed from TOF information in comparison with the singles alpha-particle spectrum. . .	49
18	Time-of-Flight vs the Energy of alpha-particles following beta-decays of ^{16}N and ^8Li	51
19	Spectra of Time-of-Flight of alpha-particles, produced by projecting a 50 keV energy slice onto the TOF axis. Data for ^{16}N with a 250 keV thick target.	53
20	Spectra of Time-of-Flight of alpha-particles, produced by projecting a 50 keV energy slice onto the TOF axis. Data for ^8Li produced in $^7\text{Li}(d,p)^8\text{Li}$	54
21	Spectra of Time-of-Flight of alpha-particles, produced by projecting a 80 keV energy slice onto the TOF axis. Data for ^{16}N with a 400 keV thick target.	55
22	Spectra of Time-of-Flight of alpha-particles. The sum of the two 'cleanest' surface barrier detectors is used, exhibiting a sensitivity for beta-decay branching ratio in the range of 10^{-10}	56

23	Uncorrected beta-delayed alpha-particle decay of ^{16}N , constructed from TOF, for 250 keV thick target. Note the resolution of the experimental system is 250 keV at $E = 1.75\text{MeV}$, the binning of the data is 50 keV. Therefore each data point receive significant contribution from its next neighbor and some contribution from its next to next neighbor.	60
24	Lifetime measurement of beta-delayed alpha-particles. The observed lifetime is consistent with 10 seconds mean lifetime of ^{16}N	61
25	Lifetime measurement of beta-delayed alpha-particles within the low energy secondary maximum. Contribution of background from beta-particles was subtracted. The observed lifetime is consistent with 10 seconds, expected for ^{16}N decay.	62
26	The ratio of number of events from TOF and singles as a function of alpha-particle energy. The high energy cutoff is due to the efficiency of TOF detection. The low energy cutoff shows the background reduction by using TOF.	63

27	Beta-delayed alpha-particel decay spectrum of ^{16}N , for 250keV thick target. Correction fro target thickness and TOF efficiency were applied. Note the resolution of the experimental system is 250keV at $E=1.75\text{MeV}$, the binning of the data is 50keV. Therefore each data point receive significant contribution from its next neighbor and some contribution from its next to next neighbor.	64
28	Beta-delayed alpha-particle decay spectrum of ^{16}N , for 170 keV thick target. Correction for target thickness and TOF efficiency were applied.	65
29	Beta-delayed alpha-particle decay spectrum of ^{16}N , for 400 keV thick target. Correction for target thickness and TOF efficiency were applied.	66
30	The A1200 Isotope Separator at the National Superconducting Cyclotron Laboratory at the Michigan State University (MSU). . . .	71
31	Energy output of PIN diode (ΔE of incoming particles) versus the TOF of incoming particles. This gives particle identification. . . .	72
32	Profile of the secondary ^{16}N beams as measured by the two-dimensional position sensitive PPAC. (a) and (c) are projections onto the vertical and horizontal axis respectively. The edge effects can be seen on the figures.	73

33	Experimental setup for the experiment conducted at MSU.	74
34	Typical two-dimensional spectrum of E2 vs E3 where E2 and E3 are the energies deposited in the second and third detector in the telescope(top), and E2 vs E3 with a veto on E4 as discussed in text(bottom).	76
35	Typical spectrum of beta-delayed alpha-particles from ^{16}N	77
36	Typical spectrum of beta-delayed alpha-particles from ^{16}N , with beta-particle background subtracted.	78
37	Beta-delayed gamma-rays from ^{16}N . Note the small intensity for the second escape peak, due to the large volume of the detector and the collimator. Scattering of gamma-rays from the collimator is noticeable around 6 MeV.	81
38	The experimental data compared with 'zero' target thickness data [Ne74].	83
39	The response function of the system at E=1.75 MeV. Note that the width is energy dependent.	85
40	Convolution of 'zero' target thickness data with square response function ($R(E)\equiv 1$) as compared with obtained data.	86

41	dY/Y as a function of energy as discussed in the text.	89
42	Convolution of 'zero' target thickness data [Ne74] with the response function of our setup as compared to measured data.	90
43	Convolution of theoretical alpha-particle spectrum corresponding to $S_{E_1}(300)=95$ keV-barn as in Fig.46 with the response function, is plotted together with the experimental data.	91
44	Unfolded spectrum of the beta-delayed alpha-particles from ^{16}N	92
45	Ratio of the secondary maximum to the peak of the broad resonance, as a function of foil thickness.	93
46	R-matrix fit to the unfolded data.	96
47	The R-matrix fit to the data with best fit, solid line ($S_{E_1}(300)=95$ keV-barn), and dash lines correspond to $S_{E_1}(300)=101$ keV-barn and 89 keV-barn, as indicated.	99
48	The yield at the secondary maximum for various values of $S_{E_1}(300)$. All other parameters are fixed at their best fit value derived by Ji et al. [Ji90]. The large variation in the yield for the secondary maximum are obtained since A_3 is fixed in these calculations.	101

49	The dependence of the extracted S-factor on the values of the response function $R(E)$ at the secondary maximum ($E_{CM} = 1.1$ MeV). The best fit value $S_{E1} = 95$ keV-barn with its lower and upper bounds ($\pm 30\%$) are shown.	102
50	The ratio of the yield for the unbound 1^- resonance to the yield of the secondary maximum, as a function of $S_{E1}(300)$. The two curves corresponds to $A_3 = -2,000$ and $-10,000$ MeV ^{1/2} , respectively.	103
51	Some of extrapolated values of $S_{E1}(300)$ obtained. The filled circles and upper limits are the extrapolation performed by the experimental groups, the open circles are the reanalysis of the experimental data.	107

List of Tables

1	Uncertainties in our measurement	77
2	Values of $S_{E1}(300)$ obtained by various experiments.	104
3	Experimental data of alpha spectra for the 250 keV thick target, corrected for target thickness and TOF efficiency. The uncertainty of the measured energy is 40 keV.	109
4	Experimental data of alpha spectra for the 170 keV thick target, corrected for target thickness and TOF efficiency. The uncertainty in measured energy is 25 keV.	110
5	Experimental data of alpha spectra for the 400 keV thick target, corrected for target thickness and TOF efficiency. The uncertainty in measured energy is 60 keV.	111
6	Unfolded data, with experimental resolution removed. The uncertainty in the measured energy is 40 keV.	112

1 INTRODUCTION

1.1 NUCLEOSYNTHESIS

One of the ultimate goals of nuclear astrophysics is to understand the production of the elements, under various astrophysical conditions. It is currently believed, that isotopes of hydrogen, helium, and traces of lithium were produced in the big bang [Sc77]. The remainder of the lithium and all of beryllium and boron are produced by the spallation of heavier elements by cosmic rays in the interstellar medium, or by nuclear reactions inside stars, or by neutrino processes. All other elements heavier than boron, are synthesized as the products of nuclear reactions in stars. Stars form, evolve, die and eject the residues of their nuclear reactions into the interstellar space. Those residues eventually form new stars. We can gain information about the evolution of stars by studying the abundance of elements and the nuclear reactions that generate and destroy them [Cl83, Fo84, Be68, Be85].

Stars are formed from interstellar gas by gravitational collapse. When a large mass of gas is compressed to a small volume, self gravitation will cause a collapse. When the pressure builds up in the center of the gas cloud, the collapse slows down, and the energy is converted into thermal energy. As the temperature rises, and reaches approximately a few million degrees Kelvin, nuclear reactions become possible. At the early stage of a (first generation) star's life, approximately 75% of the gas is hydrogen, and the first nuclear reaction to start is the 'hydrogen burning' process. During this process, hydrogen is converted into helium and

energy is released. Hydrogen burning is the main power source in the sun and lasts in stars of one solar mass for approximately 10 billion years. For a massive star, this burning stage is very short; for example it lasts approximately seven million years in a twenty-five solar masses star; see Fig. 1. As the hydrogen inside the core is exhausted, the core contracts under gravitation and heats up. At high temperatures (hundreds of million degrees Kelvin) the 'helium burning' process sets off in the core while the outside shell still burns hydrogen.

There are two major reactions in the 'helium burning' process. One is the triple alpha-particle capture reaction, which converts three alpha-particles to one carbon nucleus; and the other is the radiative capture of an alpha-particle by a carbon nucleus, to form an oxygen nucleus. The process repeats itself when the helium in the core is depleted, the core contracts and the burning of carbon sets off. The carbon, neon and oxygen burning stages produce elements up to ^{28}Si . In the final burning stage, silicon is burned to form ^{56}Fe . Since ^{56}Fe has the highest binding energy per nucleon, the burning process stops at ^{56}Fe , and the core loses its nuclear fuel and begins a very rapid collapse. When the core reaches approximately 1.4 solar masses (the Chandrasekhar limit [Ch84]), a supernovae explosion follows, and the star ejects the majority of its mass into the interstellar space, leaving behind a neutron star or a black hole.

The structure of the star before the explosion resembles an onion-shell, which has an iron core in the center and various elements from different burning stages in the outer shells, as shown in Fig. 1. Clearly, the detailed composition and

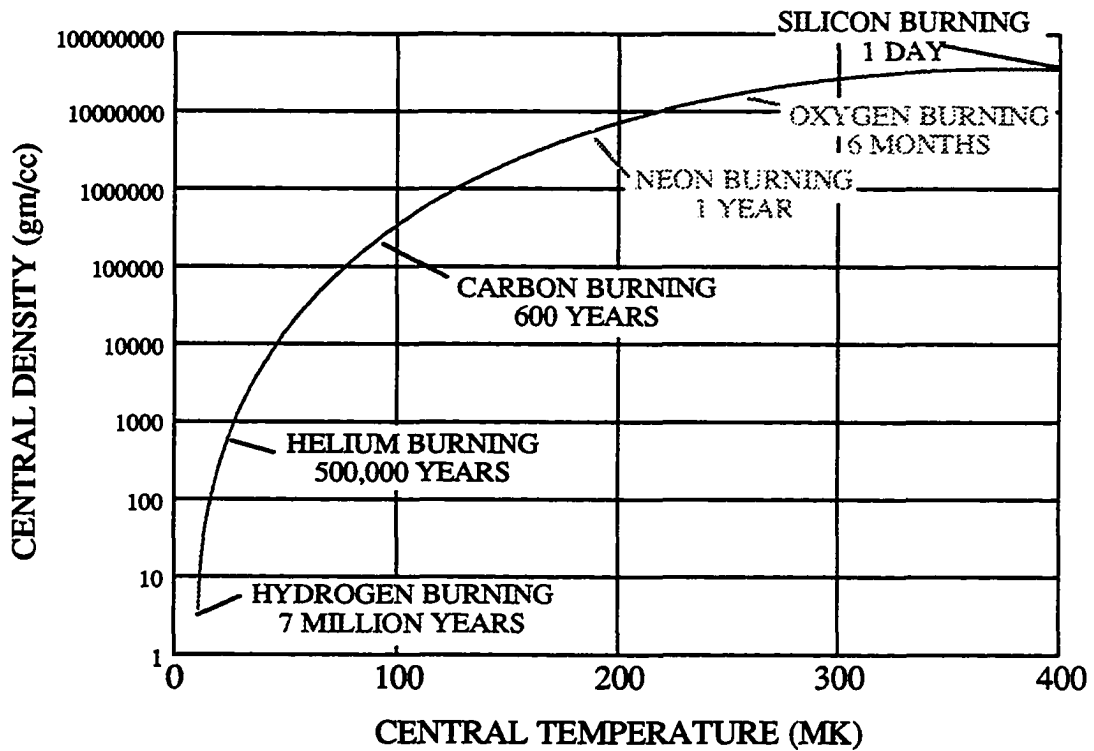
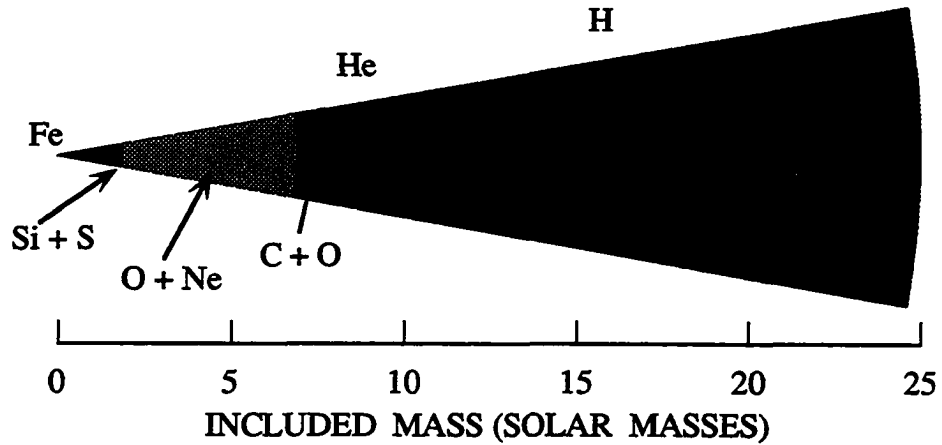


Figure 1: The evolution of a 25 solar mass star. The burning of hydrogen, helium, carbon, neon, oxygen and silicon yields an onion-shell structure, with Fe central core and shells of mixture of products of various burning stage (figure taken from [Be85]).

each shell strongly depend on the outcome of the helium burning process, i.e. the ratio of carbon to oxygen. This ratio depends on the ratio of the cross sections of the triple alpha-particle reaction and the radiative capture of alpha-particles by carbon nuclei. If the $^{12}\text{C}(\alpha, \gamma)^{16}\text{O}$ cross section is large, the main reaction product of helium burning is ^{16}O , and for a ^{12}C mass fraction smaller than 15% a star will directly proceed to oxygen burning and skip the carbon and neon burning [We92]. On the other hand, if the $^{12}\text{C}(\alpha, \gamma)^{16}\text{O}$ cross section is small, then carbon is the dominant reaction product of helium burning and the star will mainly proceed through carbon burning [Be85]. In fact, the rate of burning at the final stages of the life of a massive star and the resultant material in the vicinity of the core, determine the dynamics [We92] of the collapse, and whether the massive star collapses to a black hole or leaves behind a neutron star. In this case, the rate of $^{12}\text{C}(\alpha, \gamma)^{16}\text{O}$ reaction is crucial for determining both the dynamics of the stellar collapse and the final fate of massive stars. It is predicted [We92] that ^{12}C mass fraction drops below the critical value of 15% for an S-factor which is twice the accepted value [Ca88] but not 1.7 times the accepted value.

When the helium core heats up at the end of the hydrogen burning, the increased internal temperatures require the expansion of the stellar radius to keep the temperature gradient at a consistently low level. Therefore the outer layers cool down as a result of the great increase in radius and star reddens. Those stars are called 'red giants'. The most effective energy for helium burning in red giants is approximately 300 keV.

The last stages in the life of a massive star, the heavy elements produced by it, and its final 'death' are all clearly related to the exact value of the cross section for the $^{12}\text{C}(\alpha, \gamma)^{16}\text{O}$ capture reaction. Despite extensive theoretical and experimental work, this cross section is not well understood. In this thesis, we attempt to extract this cross section from the beta-delayed alpha-particle emission of ^{16}N .

1.2 HELIUM BURNING IN MASSIVE STARS

There are no stable mass 5 and 8 nuclei in nature. The bridge to produce elements heavier than mass 4 is the triple alpha-particle capture reaction of helium burning, as discussed in the previous section. In Fig. 2 we show the nuclear levels involved in the triple alpha-particle capture reaction. This reaction is a double resonance process. First, a small concentration of ${}^8\text{Be}$ is formed in thermal equilibrium with ${}^4\text{He}$, the concentration depends critically on the mass difference (91.78 keV) of the ground state of the nucleus ${}^8\text{Be}$ (width 6.8 ± 1.7 eV) and two alpha-particles. Then, the radiative capture of an additional alpha-particle by ${}^8\text{Be}$ forms ${}^{12}\text{C}$. In order to explain the abundance of ${}^{12}\text{C}$ in nature it was first postulated by F. Hoyle [Ho54] that this capture process is a resonant process. The 0^+ state in ${}^{12}\text{C}$ governing the three alpha-particle capture process was indeed found in the laboratory (after its prediction), at 287.7 keV above the alpha-particle threshold (379.48 keV above the three alpha-particle threshold) with a width of 8.5 ± 1.0 eV. Therefore the rate of the triple alpha-particle reaction is uniquely determined by the widths and energies of these two resonances. It is currently assessed that this reaction rate is understood within 10% accuracy.

The second important reaction in the helium burning process, is the alpha-particle capture by ${}^{12}\text{C}$ to form ${}^{16}\text{O}$, shown in Fig. 3. It is dominated by p ($l = 1$) and d ($l = 2$) waves alpha-particle capture, at helium burning energies (300 keV in red giants). The dominant contribution at the relevant energy (300 keV in red giants) comes from the tails of two subthreshold states: the 1^- state at 45 keV

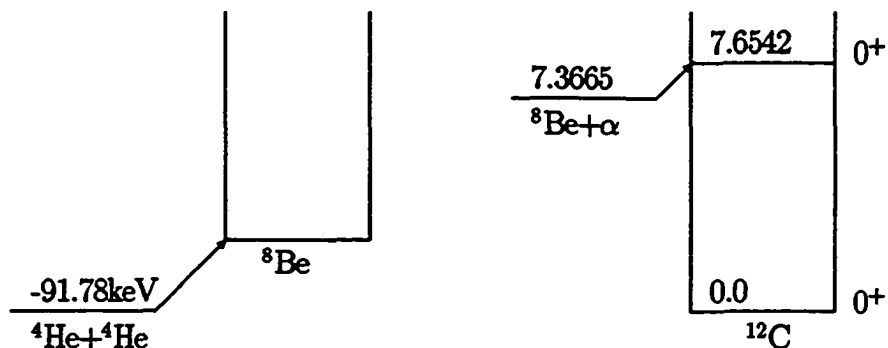


Figure 2: Simplified level scheme for the triple alpha-particle capture reaction (not drawn to scale), the reaction rate is uniquely determined by the width of the resonances and mass differences.

below the alpha-particle threshold, and the 2^+ state at 6.92 MeV (see Fig. 3). The 2^+ state contributes, because the $l = 1$ contribution to the ${}^{12}\text{C}(\alpha, \gamma){}^{16}\text{O}$ radiative capture is suppressed due to isospin selection rules for E1 radiative decays in self conjugate nuclei [Tr52]. In this work we attempt to measure the E1 component of the ${}^{12}\text{C}(\alpha, \gamma){}^{16}\text{O}$ cross section. The $l = 2$ E2 capture rate can be obtained from the extrapolation to low energies of the measured ratio of the E2 contribution to E1 contribution. This ratio can be determined more accurately than each individual $l = 1$ and $l = 2$ component.

The interaction of two particles is proportional to a geometrical factor $\pi \lambda^2 \propto \frac{1}{E}$ where λ is the de Broglie wavelength. While the resonant reaction cross section is given by the Breit-Wigner formula, the non-resonant reaction or direct capture is the process whereby a particle in the continuum interacts with the target nucleus and emits a photon to form a bound system. The non-resonant thermonuclear

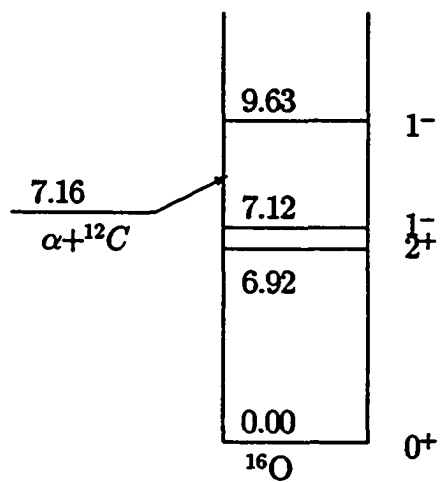


Figure 3: Simplified level scheme for the alpha-particle radiative capture by carbon nuclei (not drawn to scale). The reaction rate is determined by the reduced alpha-particle widths (γ_{α}^2) of the two subthreshold states at 6.92 MeV and 7.12 MeV.

reaction cross section strongly depends on the energy, due to Coulomb penetration factor, and it can be parameterized as:

$$\sigma = \frac{S(E)}{E} e^{-2\pi\eta} \quad (1)$$

where η is the Sommerfield parameter defined as $\eta = \frac{Z_1 Z_2 e^2}{\hbar v}$, and $S(E)$ is called the S-factor. The S-factor varies with energy much more slowly than the cross section. Consequently the extrapolation of the S-factor from existing laboratory measurements to the astrophysical energies, can be carried out with higher confidence than the direct extrapolation of the cross section.

The thermonuclear reaction rate is proportional to the Maxwellian average of the product σv , as we discuss in chapter 2. The convolution of the two functions, $e^{-\frac{E}{kT}}$ (the Maxwell-Boltzman velocity distribution) and $e^{(-2\pi\eta)}$ that governs the cross section (see equation 1), yields a peak [Cl83] at energy $E_0 = 1.22 (Z_1^2 Z_2^2 \frac{A_1 A_2}{A_1 + A_2} T_6^2)^{\frac{1}{3}}$ MeV, where T_6 is the temperature in millions of degrees. This energy is the most effective energy for the thermonuclear reaction, approximately 300 keV for helium burning in red giants. Note that while helium burning occurs at approximately 100-200 million degrees Kelvin ($kT \approx 10-20$ keV), the effective energy (E_0) is at approximately 300 keV.

At the astrophysical energy, the E1 S-factor ($S_{E1}(300)$) for the reaction $^{12}\text{C}(\alpha, \gamma)^{16}\text{O}$ is determined by the reduced alpha-particle width and energy of the subthreshold 1^- state at 7.12 MeV [Ko74]. Laboratory measurements of this cross section,

which extend as low as $E_{CM} = 900$ keV incident energy, are dominated by the contribution of the broad 1^- state at 9.6 MeV, that lies at 2.45 MeV above the alpha-particle threshold. It is impossible to measure directly the cross section of $^{12}\text{C}(\alpha, \gamma)^{16}\text{O}$ radiative capture reaction at $E_{CM}=300$ keV in the laboratory, due to the fact that it is estimated to be on the order of 10^{-8} nbarn. Furthermore the (virtual) reduced alpha-particle width (γ_α^2) of the subthreshold 1^- state can not be measured directly via alpha-particle decay, since it is energetically forbidden. The phase shift analysis of elastic scattering of alpha-particles of ^{12}C is very insensitive to this particular width and also can not be used to extract the alpha-particle reduced width of the bound 1^- state.

Over the last two decades many attempts, both experimental and theoretical, were directed at determining this S-factor [Fo84]. The cross section of $^{12}\text{C}(\alpha, \gamma)^{16}\text{O}$ reaction has been measured at higher energies by several groups, and $S_{E_1}(300)$ was determined by extrapolation. All the laboratory measurements of the cross section of $^{12}\text{C}(\alpha, \gamma)^{16}\text{O}$ reaction are governed by the broad 1^- state at 9.6 MeV, while the cross section at 300 keV is dominated by the 1^- subthreshold state at 7.12 MeV. All those determination have large uncertainties due to this large extrapolation and due to the interference between the bound 1^- state at 7.12 MeV and the unbound 1^- state at 9.6 MeV. Current extrapolated values range from 0 to 500 keV-barn (see Fig. 4 for several of the values obtained), with a compiled value of $S_{E_1}(300) = 60_{-30}^{+60}$ keV-barn and $S_{E_2}(300) = 40_{-20}^{+40}$ keV-barn [Ca88, Ba91].

In addition, Weaver and Woosley [We92] attempted to deduce this S-factor by

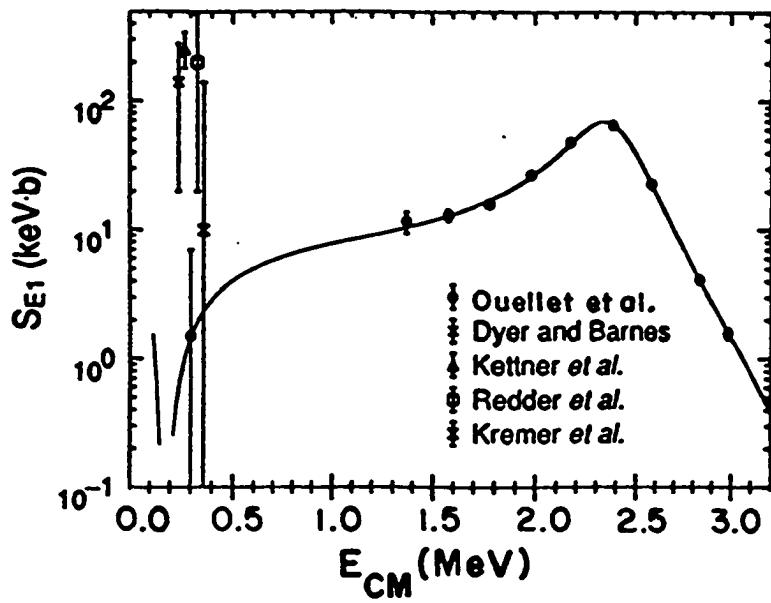


Figure 4: The extrapolated values of $S_{E1}(300)$ as obtained by various experimental groups over the last two decades (Figure taken from [Ou92]).

comparing predicted and observed abundances of heavy elements produced in massive stars. Weaver and Woosley claim that the only unknown parameter in their stellar model(s) is the rate for the $^{12}\text{C}(\alpha, \gamma)^{16}\text{O}$ reaction. They found that the mass distribution is in excellent agreement with the observed solar abundances of virtually all the intermediate mass isotopes if and only if the S-factor of the $^{12}\text{C}(\alpha, \gamma)^{16}\text{O}$ reaction to be a factor of 1.7 larger than the previously accepted value, or 100 keV-barn for the E1 S-factor. We, however, emphasize that such a rate must be deduced from laboratory measurements.

It was suggested that the beta-delayed alpha-particle emission of ^{16}N can place a constraint on the value of $S_{E1}(300)$ of $^{12}\text{C}(\alpha, \gamma)^{16}\text{O}$ reaction [Ba71]. The beta-decay of ^{16}N is particularly useful as it yields an enhanced sensitivity to measuring $S_{E1}(300)$. Since the phase space factor in beta-decay is proportional to the energy to the fifth power, the beta-decay of ^{16}N strongly favors the emission of low energy beta-delayed alpha-particles. Furthermore, the beta-decay branching ratios for the bound 1^- state at 7.12 MeV and unbound 1^- state at 9.6 MeV, see Fig. 5, indicate that the matrix element for the beta-decay to the bound 1^- state, is approximately a factor of 4 larger than the one for the unbound 1^- state. This provides further sensitivity of the beta-delayed alpha-particle emission, to the reduced alpha-particle width of the bound 1^- state.

The ground state of ^{16}N has spin and parity 2^- . The beta-decay selection rules [Kr87] for allowed beta-decay determine that states with spin and parity $1^-, 2^-, 3^-$ in ^{16}O are populated. Note the alpha-particle decay from 2^- states is parity forbid-

den. Therefore the beta-delayed alpha-particle emission spectrum of ^{16}N contains contributions from 1^- ($l = 1$) and 3^- ($l = 3$) states. Only the p-wave ($l = 1$) component is useful in constraining the $S_{E1}(300)$. The shape and the magnitude of the $l = 3$ contribution to the beta-delayed alpha-particle spectrum are still open questions and being investigated [Ji92].

To use the beta-delayed alpha-particle spectrum to constrain $S_{E1}(300)$ was developed in detail by F.C. Barker using R-matrix theory [Ba71]. Barker used the measurement of the beta-delayed alpha-particle emission of ^{16}N [Ne74], together with the direct measurement of the $^{12}\text{C}(\alpha, \gamma)^{16}\text{O}$ cross section [Dy74], and phase shift of alpha-particle elastic scattering [Jo62, Cl68, Pl87], to extract $S_{E1}(300)$. Unfortunately, the data of the beta-delayed alpha-particle emission from [Ne74] didn't allow for a further constraint on the value of $S_{E1}(300)$, due to the fact that the alpha-particle spectra was measured only in the region of the broad 1^- resonance, where the fit is not sensitive to the subthreshold 1^- state.

More recently, Baye and Descouvemont [Ba88] calculated microscopically the beta-delayed alpha-particle spectrum of ^{16}N ; Ji et al. repeated the R-matrix fit using Barker's parameterization [Ji90]; and Humblet et al. used a K-matrix analysis for the same data set [Hu91]. They all predicted that the low energy part of the beta-delayed alpha-particle decay spectrum of ^{16}N should reveal a secondary maximum, due to the destructive interference between the bound and unbound 1^- states at the vicinity of 1.4 MeV and also the reduction of alpha-

particle penetration. The relative magnitude of the secondary maximum is directly related to the reduced alpha-particle width of the bound 1^- state at 7.1 MeV and hence allows for a measurement of $S_{E1}(300)$. In Fig. 6 (taken from [Ji90]) we show the p-wave beta-delayed alpha-particle spectrum of ^{16}N predicted by the R-matrix theory. Note the p-wave beta-delayed alpha-particle spectrum was obtained by subtracting a theoretical ‘pseudo’ $l = 3$ component [Ba71, Ji92] from the experimental data [Ne74]. Here we emphasize this theoretical ‘pseudo’ $l = 3$ contribution is fairly arbitrary, the true $l = 3$ contribution remains an open question and needs to be investigated. The broad peak at 2.35 MeV corresponds to the alpha-particle decay of the unbound 1^- state at 9.6 MeV. Note the predicted secondary maximum around 1.1 MeV and a minimum in the vicinity of 1.4 MeV, due to the destructive interference between the bound and unbound 1^- states. The solid and dashed lines correspond to different $S_{E1}(300)$ values. The secondary maximum is very sensitive to the value of $S_{E1}(300)$, or the reduced alpha-particle width of the bound 1^- state. The K-matrix analysis yields the same results [Hu91], as shown in Fig. 7 (taken from [Hu91]). The microscopic calculations [Ba88] agree with the results of both R-matrix [Ji90] and K-matrix [Hu91] analyses, and it shows a strong dependence of the secondary maximum on the value of $S_{E1}(300)$; see Fig. 8.

The beta-delayed alpha-particle emission of ^{16}N measured with high sensitivity at low energy, is predicted by these three theories to be a good tool for measuring $S_{E1}(300)$. We, however, note that the beta-decay of ^{16}N has to be measured with a sensitivity for a branching ratio, on the order of 10^{-9} at low energies. In this thesis,

we discuss an experiment that allows for such a high sensitivity measurement and the extraction of the value of $S_{E1}(300)$.

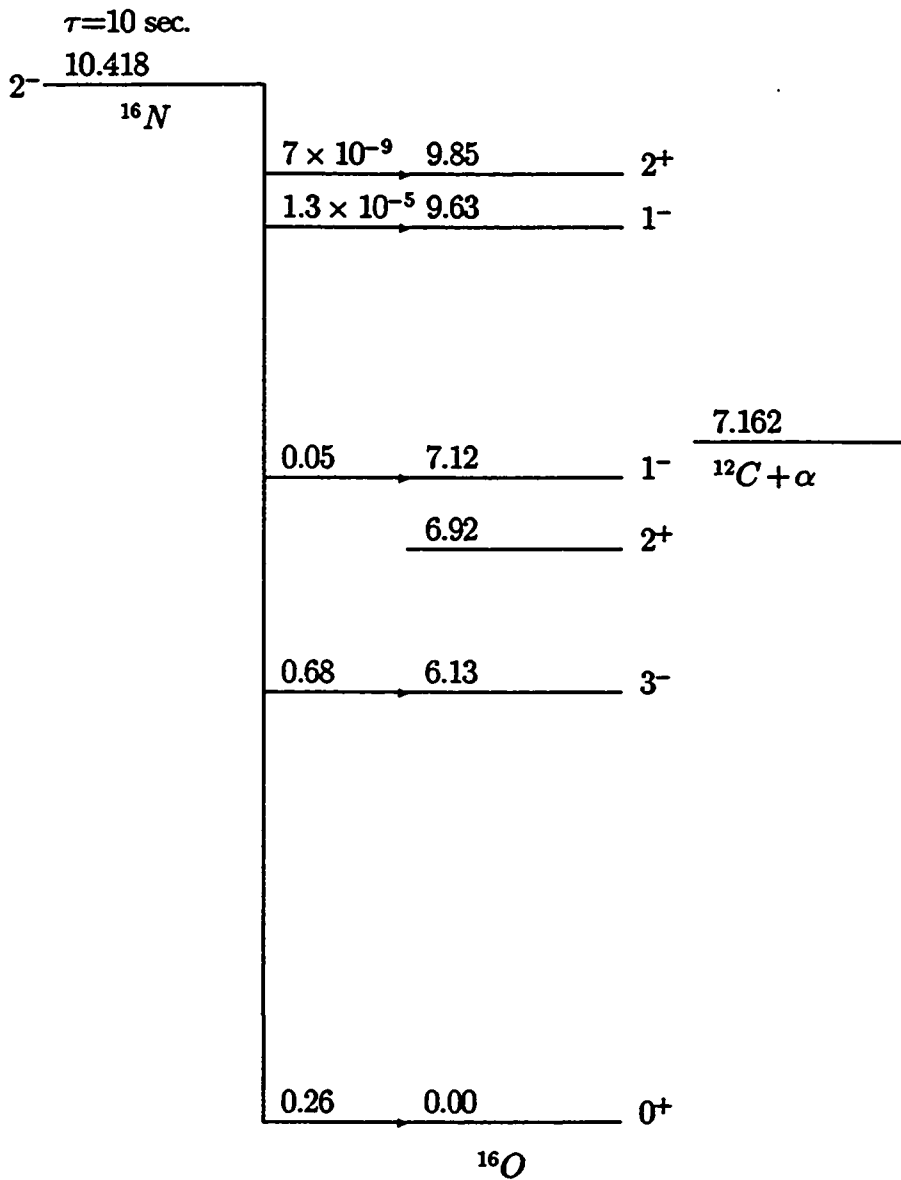


Figure 5: Simplified level scheme for the radiative capture of alpha-particles by ^{12}C and the beta-delayed alpha-particle emission (not drawn to scale). The most significant contribution to the astrophysical cross section of $^{12}\text{C}(\alpha, \gamma)^{16}\text{O}$ reaction is from the bound 1^- state at 7.12 MeV.

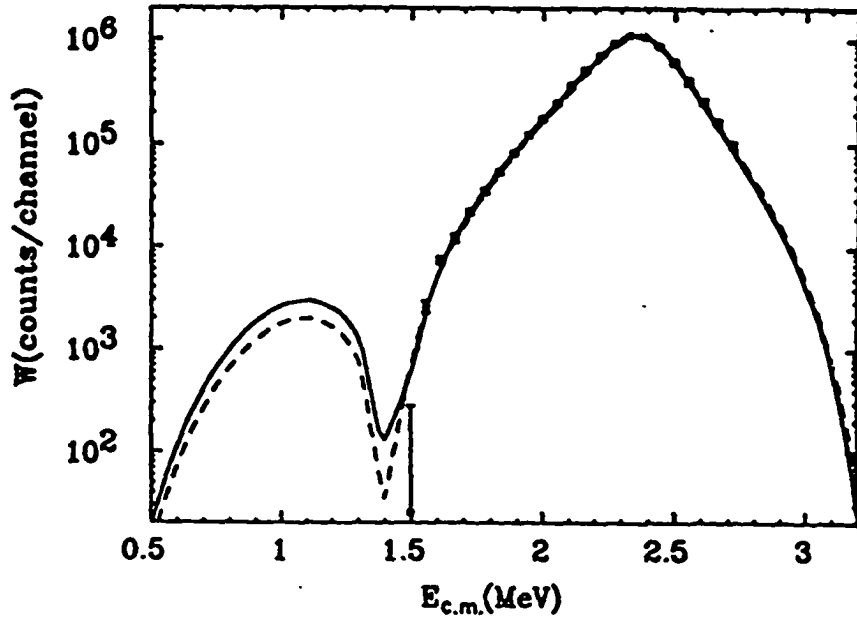


Figure 6: The p wave β -delayed α -particle decay spectrum of ^{16}N , predicted by Ji et al. [Ji90]. The solid curve is calculated with the best-fit parameters and $S_{E1}(300)=130$ keV-barn($A_3=0$), and dashed curve with $S_{E1}(300)=90$ keV-barn($A_3 = -7,000$ MeV $^{1/2}$). Figure taken from [Ji90].

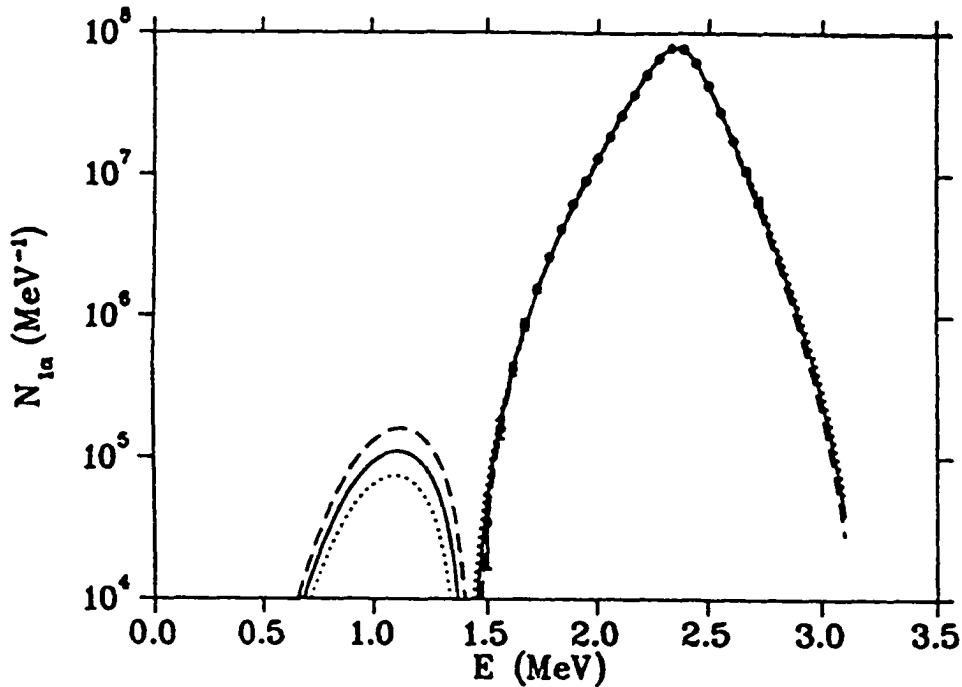


Figure 7: The β -delayed α -particle decay spectrum of ^{16}N from K -matrix analysis. Dashed, solid and dotted lines correspond to $S_{E1}(300) = 63, 43, 27$ keV-barn, respectively. (Figure taken from [Hu91].)

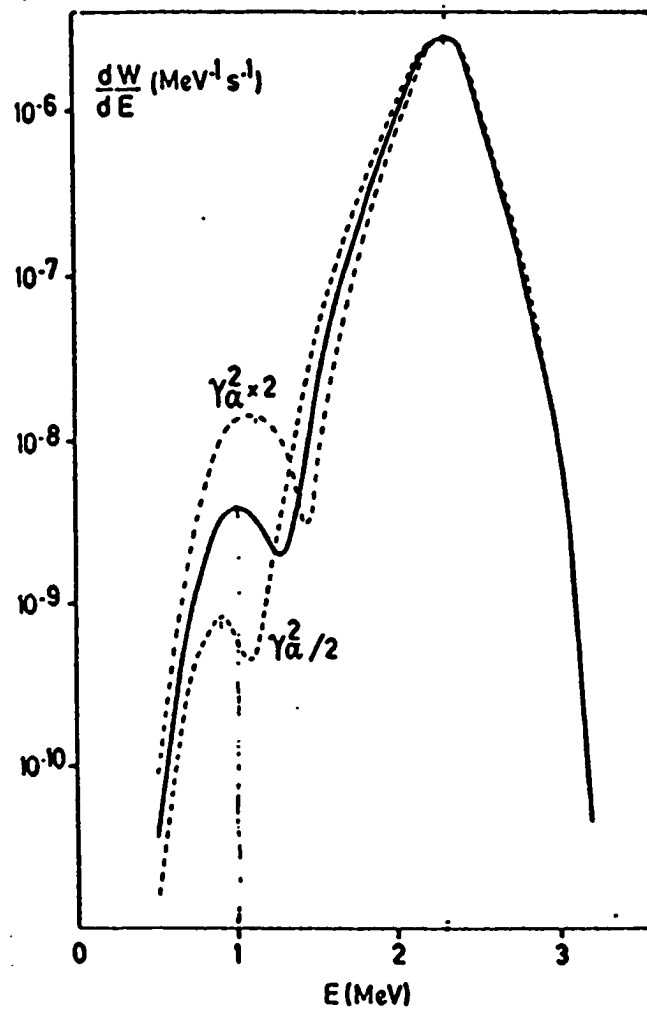


Figure 8: The beta-delayed alpha-particle emission spectra from microscopic calculation. The predicted yield for a reduced alpha-particle width [i.e. $S_{E1}(300)$] varied by a factor of 2 is shown. Note the scale of the predicted branching ratio, on the order of 10^{-9} . Figure taken from [Ba88]).

2 THEORY

2.1 THERMONUCLEAR REACTION RATE

The classical Coulomb barrier between two charged particles is given by:

$$V = \frac{Z_1 Z_2 e^2}{R} \approx \frac{Z_1 Z_2}{A_1^{1/3} + A_2^{1/3}} (MeV) \quad (2)$$

where Z_1 , Z_2 are the atomic numbers of the charged particles, A_1 and A_2 their mass numbers, and R the distance between the two charged particles. The kinetic energy of particles in stars, determined by thermal energy $kT=8.62 \times 10^{-8} T$ keV, is very small compared to the Coulomb barrier. Nuclear reactions in stars are, however, possible due to the penetration through the Coulomb barrier and the tail of the Maxwell-Boltzmann velocity distribution of the charged particles. In general, the thermonuclear reaction rate (R in sec^{-1}) between two charged particles, is given by the products of number densities (N_1 and N_2) of the two species, the average of the products of cross section, and the relative velocity over the Maxwell-Boltzmann distribution:

$$R = \frac{N_1 N_2}{1 + \delta_{12}} \langle \sigma v \rangle (\text{sec}^{-1}) \quad (3)$$

where δ_{12} is the Kronecker delta; v is the relative velocity of two particles, and $\sigma(E)$ the energy dependent cross section.

2.2 R MATRIX PARAMETRIZATION OF THE $^{12}\text{C}(\alpha, \gamma)^{16}\text{O}$ REACTION

The foundation of the R-matrix theory were developed by E.P. Wigner and L. Eisenbud [Wi47], and a discussion of this theory can be found, for example, in [Te52, La58]. The following discussion follows [Bo77, Br70, La58].

For the exterior region of the nuclear reaction, the wave function can be written as,

$$\psi = \phi^I \phi^{II} \varphi(\bar{r}) \quad (4)$$

where ϕ^I and ϕ^{II} are the wave functions of two fragments respectively, involving their internal coordinates only. $\varphi(\bar{r})$ is the wave function of relative motion of their respective center of masses, and is a solution to the problem of a free particle or a particle in Coulomb potential.

In the internal region, a set of states (labeled by λ) of all nucleons is defined. The interior wave function can be expanded in terms of this complete set of states. The interior wave functions have to satisfy the nuclear Schrödinger equation, and are defined by boundary conditions (B) on the logarithmic derivatives of their radial parts at channel radius (a). The R matrix is then introduced to take into accounts all interactions inside nuclei. In addition to dependence on E and the a, this matrix also depends on the boundary condition parameter (B). Wigner and

Eisenbud [Wi47] have shown that the energy dependence of any element of R can be expressed in the following form,

$$R_{cc'}(E) = \sum_{\lambda} \frac{\gamma_{\lambda c} \gamma_{\lambda c'}}{E_{\lambda} - E} \quad (5)$$

where λ is labels the members of this complete set of states. The $\gamma_{\lambda c}$ are the reduced width amplitudes, and depend on a, B. The E_{λ} are the energy eigenvalues of the states λ . By matching the logarithmic derivatives of the internal and external wave functions at the nuclear surface, one obtains a relation between collision function U and the R function, [Bo77]

$$U = e^{-2i\phi_l} \left[\frac{1 - R(S_l - B - iP_l)}{1 - R(S_l - B + iP_l)} \right] \quad (6)$$

where ϕ , P_l and S_l are the hard sphere phase shift, the penetration factor and the shift factor.

The scattering cross section is then given by [La58],

$$\sigma(\theta) = \frac{1}{4} \left| \sum_l (2l+1)(1-U_l)P_l(\cos\theta) \right|^2 \quad (7)$$

here $P_l(\cos\theta)$ is the Legendre polynomial.

In the early 70's, Barker first developed [Ba71] the R-matrix theory for the anal-

yses of the $^{12}\text{C}(\alpha, \gamma)^{16}\text{O}$ reaction using three sets of data that existed at that time:

- a) The cross section of $^{12}\text{C}(\alpha, \gamma)^{16}\text{O}$ at energies as low as 1.3 MeV.
- b) The phase shift of elastic scattering of alpha-particles from ^{12}C .
- c) The beta-delayed alpha-particle spectrum of ^{16}N .

The following discussion follows reference [Ba71].

As we discuss below, the data on the beta-delayed alpha-particle emission of ^{16}N available at that time [Ne74] was only sufficient to lay the foundation of the R-matrix analysis, and not good enough to allow any further constraint on the value of $S_{E1}(300)$.

For the relative $l = 1$ motion of an alpha-particle and ^{12}C , Barker used a three-level approximation for the R matrix. The first level corresponds to the 7.12 MeV 1^- state of ^{16}O , which is 45 keV below the α - ^{12}C threshold; its radiation width is well known, see Fig. 5. The second level is the broad 1^- resonance at 9.6 MeV in ^{16}O , with total width of approximately 400 keV. The third level is a background level, representing contributions from all higher lying 1^- states in ^{16}O .

The α - ^{12}C elastic scattering phase shift in the ($l = 1$) 1^- channel at center-of-mass energy E , is parameterized in the R-matrix theory as:

$$\delta^{1-}(E) = -\phi(E) + \arctan \left[\frac{P(E)}{R^{-1}(E) - S(E) + B} \right] \quad (8)$$

where,

$$R(E) = \sum_{i=1}^3 \frac{\gamma_{i\alpha}^2}{E_i - E} \quad (9)$$

is the R function associated with the alpha-particle elastic scattering channel, $\phi(E)$ is the hard-sphere scattering phase shift, $P(E)$ is the energy-dependent penetration factor, $S(E)$ is the shift factor, which is calculated with Coulomb functions at channel radius a . E_i is the pole energy (related to the resonance energy by a shift $\gamma_{i\alpha}^2 S_i$) [La58]. $\gamma_{i\alpha}^2$ is the alpha-particle reduced width of the i th level, given by $\frac{\Gamma_{i\alpha}}{2P}$ with $\Gamma_{i\alpha}$ to be the level width [La58]. B is the constant boundary condition parameter. Barker [Ba71] used arguments based on shell model descriptions of the ^{16}O states. Therefore the R-matrix eigenstate in the internal region should most nearly resemble a shell model state for B_i equal to S_i :

$$B = S(E_i) \quad (10)$$

$P(E)$ is energy dependent penetration factor, can be written as [Bl79],

$$P_i(E) = \frac{ka}{F_l^2(a) + G_l^2(a)} \quad (11)$$

where $F_l(r)$ and $G_l(r)$ are the ‘regular’ and ‘irregular’ solutions of Schrödinger equation for Coulomb field, see [Bl79] for more detail.

Because the lowest level is bound and its energy accurately known, the parameters of this level are restricted. Hence Barker [Ba71, Ba87] and Ji et al. [Ji90] used the following fitting parameters: the energy of the unbound 1^- state (E_2) and its reduced alpha-particle width ($\gamma_{2\alpha}$), as well as the reduced width of background level ($\gamma_{3\alpha}$) with its energy fixed at 23 MeV (since the energy and width are correlated). The quality of the fit is obtained by minimizing the quantity:

$$\chi^2 = \frac{1}{N} \sum_{i=1}^N \left| \frac{\delta^{exp}(E_i) - \delta(E_i)}{\varepsilon(E_i)} \right|^2 \quad (12)$$

where E_i are the energies of the N data points and $\delta(E_i)$ and $\delta(E_i)^{exp}$ the calculated and measured phase shifts at E_i respectively. $\varepsilon(E_i)$ are the errors for elastic scattering phase shift.

The contribution to the $^{12}\text{C}(\alpha, \gamma)^{16}\text{O}$ cross section from 1^- intermediate states of ^{16}O is given by:

$$\sigma^{(1-)}(\alpha\gamma) = \frac{6\pi}{k_\alpha^2} P_1 \left| \frac{\sum_{i=1}^3 [\gamma_{i\alpha} \Gamma_{i\gamma}^{\frac{1}{2}} / (E_i - E)]}{1 - (S_1 - B + iP_1) \sum_{i=1}^3 [\gamma_{i\alpha}^2 / (E_i - E)]} \right|^2 \quad (13)$$

where $\Gamma_{i\gamma}$ is the radiation width of level i . P_1 is the penetration factor. The measured width of the 7.12 MeV level $\Gamma_{1\gamma}^{obs}$ is related to the formal width $\Gamma_{1\gamma}$ by

the following relation:

$$\Gamma_{1\gamma} = \Gamma_{1\gamma}^{obs} \left[1 + \gamma_{1\alpha}^2 \frac{dS(E)}{dE} \Big|_{E=E_1} \right] \quad (14)$$

here the difference is due to the energy dependence of the level shift in the alpha-particle channel [Ba71]. $\Gamma_{1\gamma}$ is taken to be 55 meV [Ji90].

Clearly the knowledge of the (virtual) reduced alpha-particle width of the bound 1^- state ($\gamma_{1\alpha}^2$) allows us to determine the cross section of $^{12}C(\alpha, \gamma)^{16}O$ reaction using equation 13. Note this equation involves other free parameters that can be fixed from available data. The parameter $\gamma_{1\alpha}^2$ is most crucial due to the small $(E_1 - E)$ denominator. This parameter $\gamma_{1\alpha}^2$ could not be determined thus far. In this thesis, we attempt to deduce this reduced alpha-particle width and thus provide the cross section for $^{12}C(\alpha, \gamma)^{16}O$ reaction, see equation 13. This cross section is in turn related to the S-factor by equation 1. Hence the measurement of the cross section for $^{12}C(\alpha, \gamma)^{16}O$ reaction, the reduced alpha-particle width of the bound 1^- state, and the S-factor are all intimately connected.

The quality of the fit is again measured by the χ^2 test:

$$\chi^2 = \frac{1}{N} \sum_{i=1}^N \left| \frac{\sigma^{exp}(E_i) - \sigma(E_i)}{\eta(E_i)} \right|^2 \quad (15)$$

where N is number of points and $\sigma^{exp}(E_i)$ and $\sigma(E_i)$ are the measured and calcu-

lated cross section at energy E_i respectively. $\eta(E_i)$ are the errors.

The ground state of ^{16}N has spin and parity 2^- (see Fig. 5), while the alpha-particle and ^{12}C both have 0^+ . The beta-decay selection rules for a Gamow-Teller transition, determine that the allowed beta-decays populate 1^- , 2^- and 3^- states in ^{16}O . While the alpha-decay from 2^- is parity forbidden, the beta-delayed alpha-decay spectrum of ^{16}N contains $l = 1$ (p wave) and $l = 3$ (f wave) components, added incoherently. Clearly only the p wave component is useful in constraining $S_{E1}(300)$.

The calculated 1^- alpha-particle spectrum $W^{(1^-)}(E)$, the number of alpha-particles per unit energy for a total center-of-mass energy E in the 1^- channel, is parameterized in the R-matrix theory as:

$$W^{(1^-)}(E) = f_\beta(E)P(E) \left| \frac{\sum_{i=1}^3 [A_i / (E_i - E)]}{1 - [S(E) - B + iP(E)]R(E)} \right|^2 \quad (16)$$

where $f_\beta(E)$ is the integrated Fermi function $F(W,Z)$, with $W=(3.768-E)/m_e$ and $Z=8$.

The beta-decay amplitude A_i in equation 16 is proportional to the hadronic matrix element of the Gamow-Teller operator between initial and final hadronic states.

For the 7.12 MeV bound state, A_1 is given by [Ba71]:

$$A_1^2 = \frac{NY(7.12)\gamma_{1\alpha}^2(1 + \gamma_{1\alpha}^2 \frac{dS}{dE}|_{E=E_i})}{\pi Y(9.6)F(7.46, 8)} \quad (17)$$

where N is total number of alpha-particles and Y(7.12) and Y(9.6) are the experimental beta-decay branching ratios to 7.12 MeV and 9.6 MeV states respectively.

There are two extra fitting parameters here, the beta-decay amplitude for the unbound state(A_2) and the background level(A_3).

Again the quality of the fits is measured by the χ^2 test:

$$\chi^2 = \frac{1}{N} \sum_{i=1}^N \left| \frac{W^{exp}(E_i) - W(E_i)}{\eta(E_i)} \right|^2 \quad (18)$$

where N is number of points and $W^{exp}(E_i)$ and $W(E_i)$ are the measured and calculated number of decays at energy E_i respectively. We emphasize that all χ^2 (equations 12, 15, 18) are minimized simultaneously for the three data sets that we discussed earlier.

Barker and Kajino [Ba91] studied in details the dependence of the extracted value of $S_{E1}(300)$ on the model parameter space. In particular they studied the dependence on the channel radius (a). The channel radius used in this work is 5.5 fm, very close to the radius defined by $a = 1.4(A_1^{\frac{1}{3}} + A_2^{\frac{1}{3}})$ fm. In this work, we do not intend to study in depth such effects, instead we use the parameter space used by Ji et al [Ji90] for the best fit, and leave such detailed studies for future theoretical

analyses of our data.

3 THE EXPERIMENTS

In Fig. 5 of the previous chapter, we show the levels of ^{16}O relevant for the beta-delayed alpha-particle decay of ^{16}N . The major component of this alpha-particle spectrum is the decay from the broad 1^- state at 9.6 MeV ($\Gamma \approx 400$ keV). The beta-decay branching ratio to this state was measured to be $1.20(5) \times 10^{-5}$ [Ne74]. As discussed in the previous chapter, the secondary maximum at lower energy, is predicted to be approximately 1,000 to 10,000 smaller relative to the decay from this broad state. Therefore the observation of the secondary maximum requires the experimental sensitivity for beta-decay branching ratio to be on the order of 10^{-9} . We discuss in this chapter our measurements of spectra of alpha-particles extended to low energy. The experiment was conducted at the A.W. Wright Nuclear Structure Laboratory at Yale University using the ESTU tandem accelerator. In addition we discuss a remeasurement of the branching ratio of the beta-decay to the broad 1^- state, conducted at the National Superconducting Cyclotron Laboratory at Michigan State University, using the superconducting K1200 cyclotron and the A1200 isotope separator.

3.1 EXPERIMENTS AT YALE UNIVERSITY: The Beta-Delayed Alpha-Particle Emission of ^{16}N

The objective of the experiments conducted at the A.W. Wright Nuclear Structure Laboratory was to measure the beta-delayed alpha-particle decay at low energies with a high sensitivity. This measurement posed two major challenges:

a) One needs to measure low energy alpha-particles, which requires a very thin catcher foil, and at the same time one needs a reasonable production yield of ^{16}N , which requires a thick target.

b) One needs to reduce the background caused by beta-particles, since there are approximately 10^9 beta-particles for each alpha-particle decay over the region of interest.

3.1.1 EXPERIMENTAL PROCEDURES

The experimental setup of the Yale experiment is shown in Fig. 9. A beam of 9 MeV deuterium was produced by the ESTU tandem accelerator at the A.W. Wright Nuclear Structure Laboratory at Yale University, with typical beam intensity of $2\text{-}5\mu\text{Amp}$. While the beam was on, the target was exposed to the beam for 10 seconds, ^{16}N nuclei were produced in the target, and a large portion of the recoiling ^{16}N nuclei stopped inside the target. When the beam was off, the arm was rotated 180 degrees, to the counting area. An array consisting of 9 silicon surface barrier detectors Si(SB) was used at one side of the foil to detect the alpha particles and another array of 12 plastic scintillator detectors on the other side, to detect the beta-particles.

By tilting the target at approximately 7° with respect to the beam (see Fig. 9), we have been able to use a thin foil but at the same time obtain a reasonable yield for the production and stopping of ^{16}N nuclei. The energy of the alpha-particles of interest were overdetermined by measuring both the energy and the time-of-

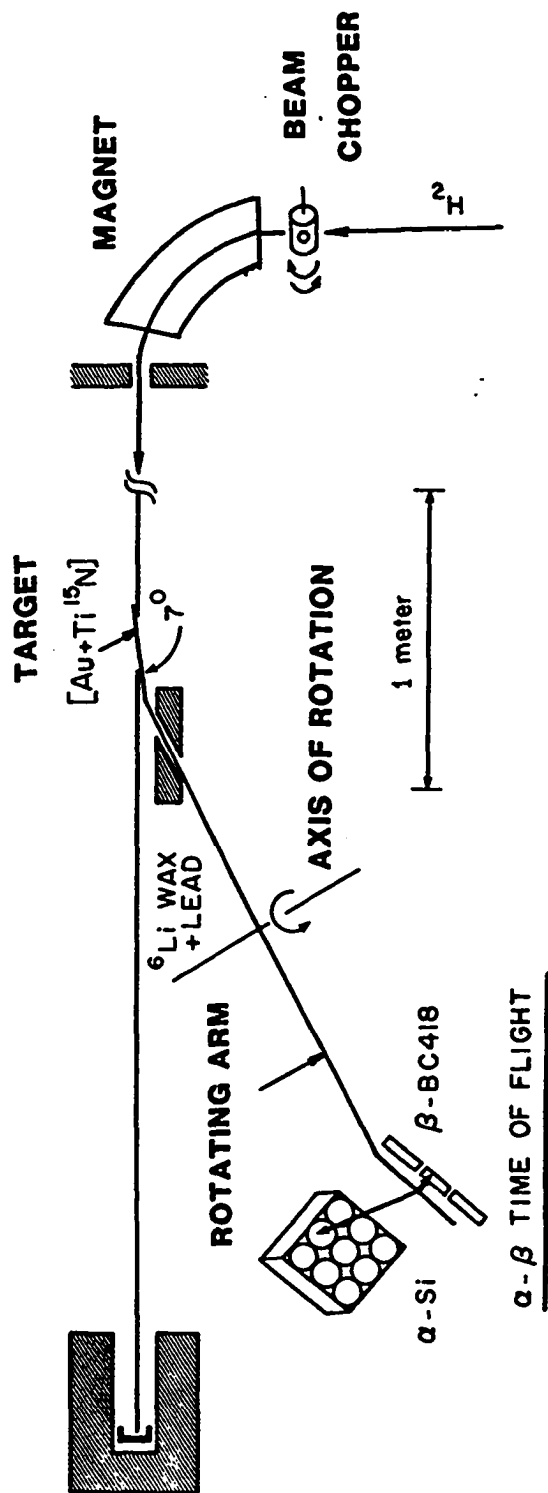


Figure 9: Schematic diagrams of experimental setup used for the Yale experiment.

flight of the alpha-particles. In this way we were able to significantly reduce the background from beta-particles (which had a very different time of flight for the same energy) and obtain the required sensitivity for a beta-decay branching ratio in the range of $\leq 10^{-9}$.

The reaction $^{15}\text{N}(d,p)^{16}\text{N}$ was chosen for the production of ^{16}N nuclei, due to its large cross section of approximately 250mb [Bo72]. The large (d,n) cross section produces a large neutron flux that significantly contributed to the background in the silicon surface barrier detectors. Consequently a beam chopper was used, which intercepted the beam approximately 20 meters away. We recorded decay events during beam-off periods only. In Fig. 10 we show the comparison of the singles alpha-particle spectra as recorded in the surface barrier detectors, when the beam chopper was used (events recorded during beam-off period) and when the chopper was not used (lower panel). The background from neutrons, when the beam chopper was not in use, is clearly shown in this figure. The beam-on and beam-off cycles were controlled by an up-down counter fed from a fixed frequency pulser. A mechanical beam chopper, placed at the high energy end of the ESTU accelerator, was controlled by this up-down counter.

The Ti^{15}N targets were mounted on both ends of a rotating arm (with only one target exposed to the beam). By tilting the target, at 7° with respect to the beam, the effective target thickness was increased approximately by a factor of 8 which allows for an increase in the yield as well as stopping of the recoiling ^{16}N nuclei. The rotating arm, of approximately 1 meter diameter, was stepped 180 degrees at

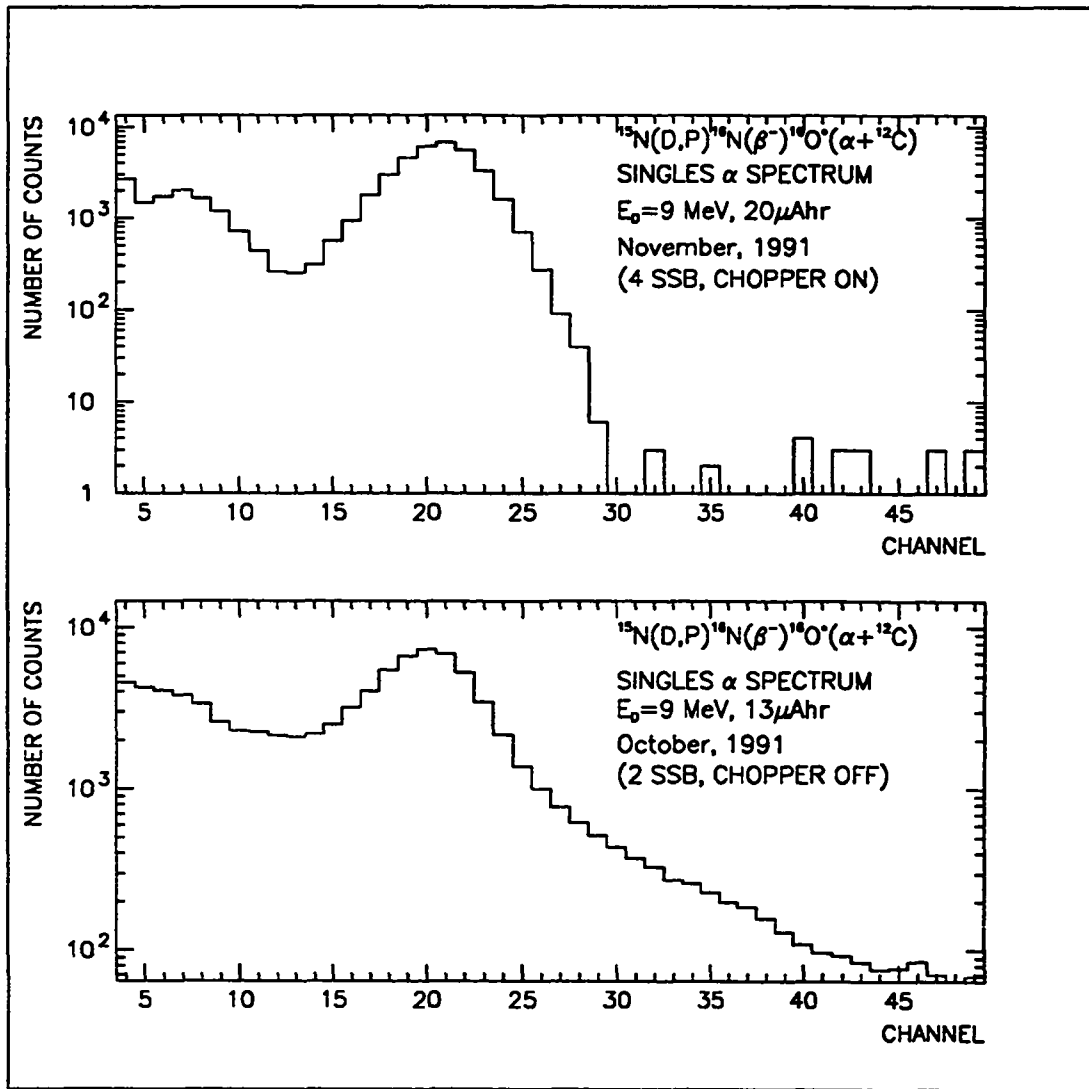


Figure 10: Singles alpha-particles spectrum with beam chopper on (upper panel), and beam chopper off (lower panel).

each time, by a stepping motor controlled from the same pulser which controlled the chopper. The travel time of the rotating arm was adjusted to 4 seconds to allow the decay of short lived contaminants. The stepping motor was controlled by an IBM-PC/80386 with CAMAC interface, produced by DSP-Technologies. The use of the beam chopper yields a duty cycle of 32%.

For 9 MeV deuterium beams, the differential cross section of $^{15}\text{N}(\text{d,p})^{16}\text{N}$ is mainly forward peaked [Bo72]. The recoil ^{16}N nuclei are distributed in a 45° forward angle cone, with kinetic energies up to 2.9 MeV. The range of ^{16}N nuclei in the Ti^{15}N target (Au backing), was calculated using the Monte Carlo code TRIM'91 [Zi91]. These Monte Carlo calculations demonstrate that a large fraction of the recoiling ^{16}N nuclei stop inside our target. In Fig. 11 we show the results of these Monte Carlo calculations for 700 keV recoiling ^{16}N nuclei.

The nine silicon surface barrier detectors have active area of 450 mm^2 each and have thicknesses of $50\text{ }\mu\text{m}$. The large area detectors were chosen to achieve the large solid angle coverage with reasonable cost of the detectors and electronics. We chose to use thin Si(SB) detectors to minimize the energy deposited in the detectors from beta-particles. We were unable to obtain even thinner detectors at such large area, due to the limitation in manufacturing. The detectors were purchased from EG&G ORTEC. The array of silicon surface barrier detectors was situated inside the vacuum chamber, 9 cm away from the target, and covered 6% of 4π . The Si detectors were cooled by flowing alcohol at a temperature of approximately -20°C . Typical energy resolution of the silicon detectors was

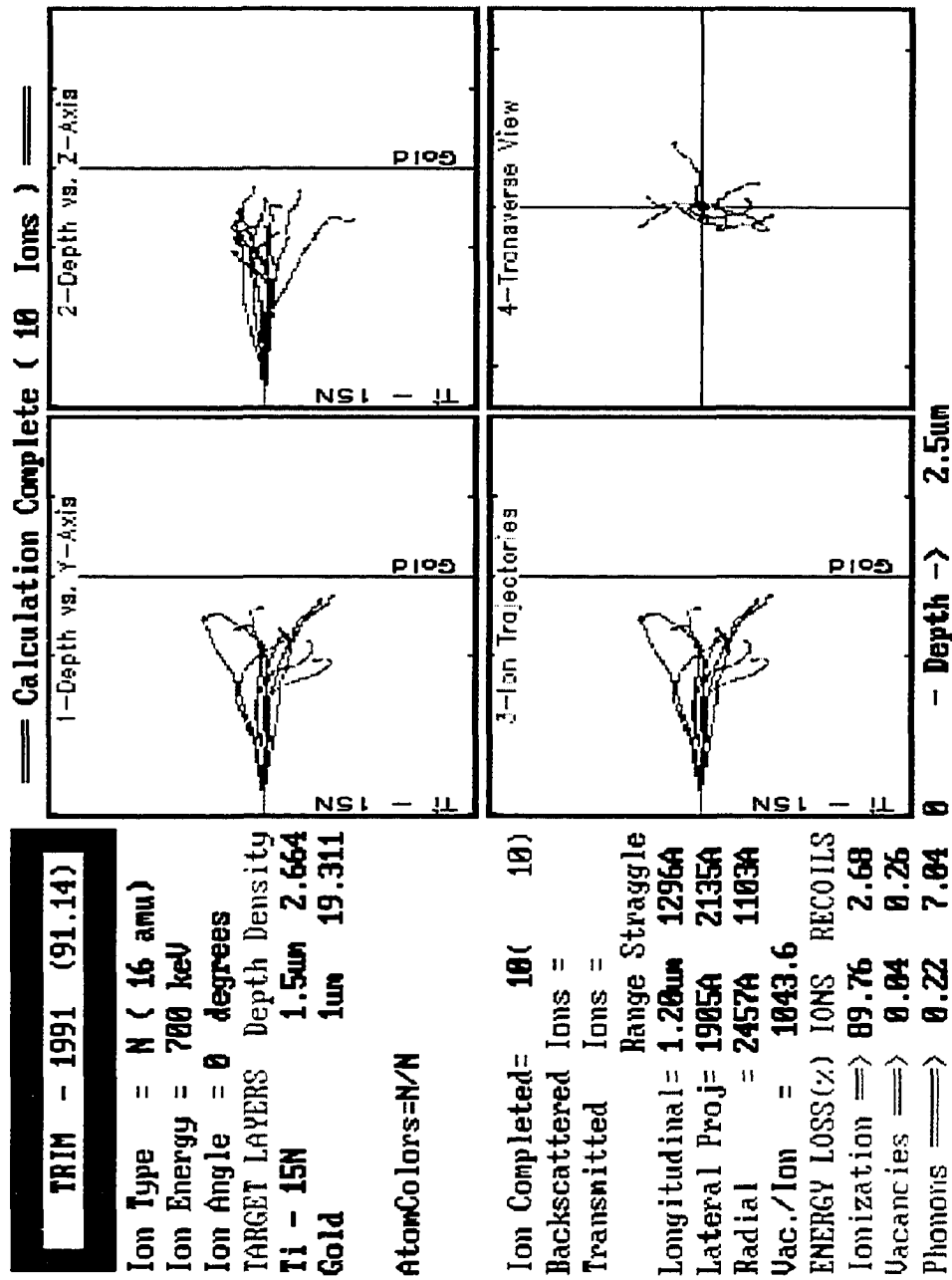


Figure 11: Typical range and straggling calculations for recoiling ^{16}N nuclei in our target.

measured to be 50-75 keV. The electronic thresholds for the Si(SB) detectors were set at 300-400 keV. Alpha-particle counting rates for individual surface barrier detectors was approximately 0.02 Hz. The counting rates were kept very low, to reduce accidental coincidences, as well as minimize pile-up of beta-particles and alpha-particles in the Si detectors.

The beta-particle detectors were constructed from BC418 plastic scintillator, situated inside the vacuum chamber, 2 cm away from the foil, and optically coupled to photomultiplier tubes outside the vacuum chamber. The photomultiplier tubes were Hamamatsu H3165 and H3171. Twelve beta-particle detectors were closely packed (six had dimension 1 inch \times 1 inch \times 1/4 inch, and six had dimension 2 inch \times 2 inch \times 1/4 inch). The beta-particle detectors were optically insulated from each other, and cover geometric solid angle of 35% of 4π . The threshold of the beta-particle detectors were set (using gamma-ray sources) approximately at 100 keV. Typical counting rate for each beta-particle detector was 100-200 kHz. The total efficiency (solid angle times the intrinsic efficiency) of the beta-particle detector array was approximately 25% and the time resolution of alpha-beta time of flight (TOF) was $\sigma \approx 1$ ns for 1 MeV alpha-particles. Note that low energy alpha-particles are expected to have worse time resolution. In addition, the large capacity of our Si detector contributed significantly to the time resolution. However, this time resolution was sufficient to remove the large background due to β - γ coincidences in the time-of-flight spectra. In addition, it was sufficient to remove low energy signals from alpha-particles that deposited a fraction of their energy in the detector, due to partial charge collection in the surface barrier detector.

The detection of low energy alpha-particles with good time resolution is a formidable task. Hence we have conducted extensive time resolution tests for different designs of preamplifiers using a ^{228}Th source and a $\Delta\text{E-E}$ system consisting of a thin ($25\ \mu\text{m}$, $25\ \text{mm}^2$) silicon surface barrier detector (ΔE) and a micro-channel plate assembly (E) (see Fig. 12). The Canberra 2003BT preamplifiers were chosen as a result of these extensive tests for their high performance of good energy and the time resolution and low noise level. In Fig. 12, we show the $\Delta\text{E-E}$ coincidence (upper panel) and the energy deposited in ΔE detector from the ^{228}Th source (lower panel). Typical time resolution obtained for small Si detector (i.e. small capacity), using Canberra 2003BT preamplifiers, was $\sigma \approx 120\ \text{ps}$ for 2.9 MeV energy deposited by alpha-particle. We have also studied the time resolution of the large area Si detectors as a function of incident alpha-particle energies, by replacing the micro-channel plate E detector with our large area Si detector in the $\Delta\text{E-E}$ telescope, see Fig. 12. The preamplifiers were then modified to match the large capacitance of the Si detectors, in order to obtain the best timing output response. The typical time resolution for large area detectors ($450\ \text{mm}^2$, $50\ \mu\text{m}$) is $\sigma \approx 520\ \text{ps}$ for 5.5 MeV energy deposit by alpha-particles.

The electronics schematics of the experiment is shown in Fig. 13. The time-of-flight (TOF) was measured using a TDC with alpha-particles as the start and beta-particles as a stop in order to minimize the dead time. The time resolution of alpha-beta TOF was optimized for the choice of electronics modules and adjustments, including the choice of time delay for the constant fraction discriminator. The data acquisition system was triggered by signals from any alpha-particle de-

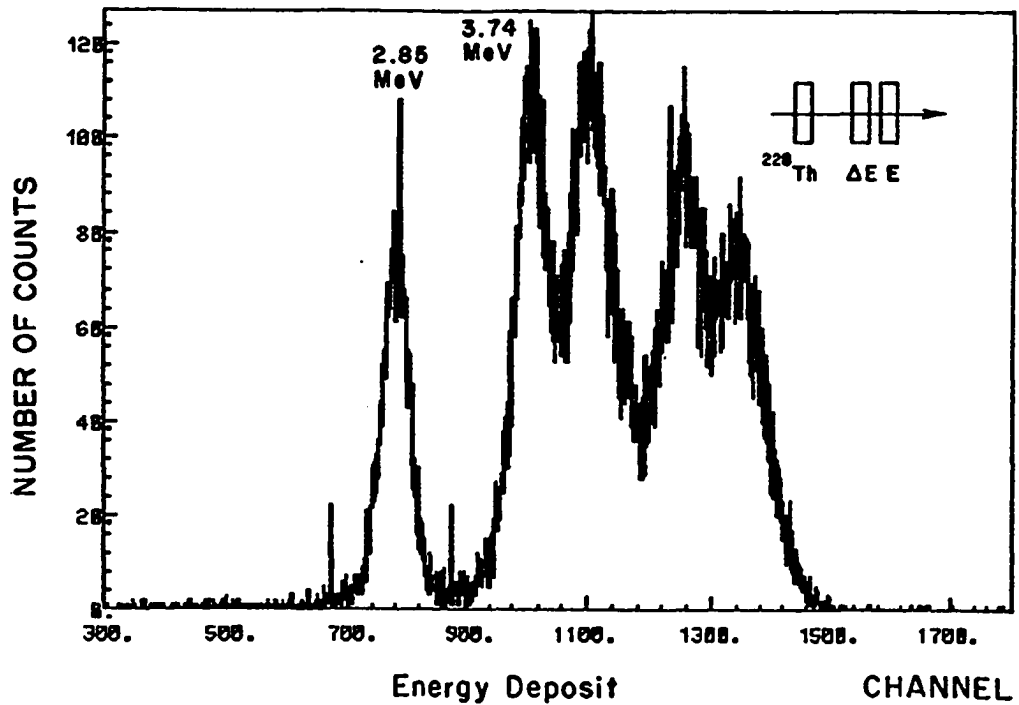
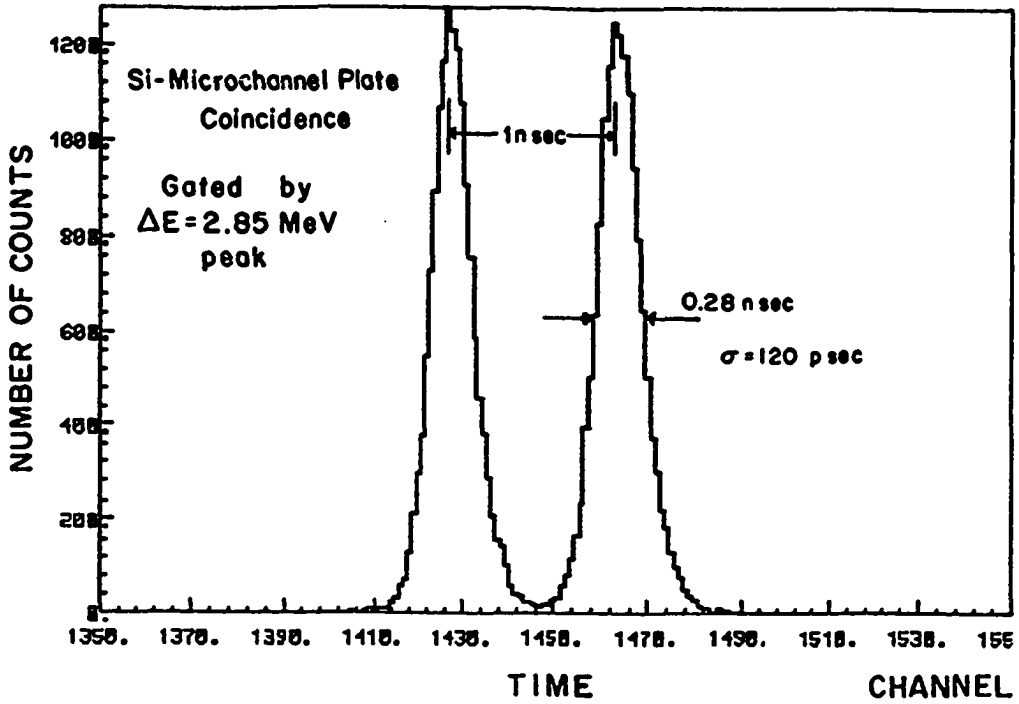


Figure 12: Time resolution for alpha-particles from ^{228}Th source, with a telescope consisting of a Si detector ($25\mu\text{m}$, 25mm^2) and a micro-channel plate assembly (upper panel). The alpha-particle energy deposited in Si detector is shown in lower panel.

tectors, and the energy of the alpha-particles (ADCs) and alpha-beta TOF (TDCs) were recorded onto magnetic tapes in an event-by-event format, for offline data analysis. Each individual alpha-beta pairs were separated in software, using the information from the pattern register.

The TOF for alpha-beta's, were measured using ~ 5 MeV alpha-particles from an ^{227}Ac source that yields $\gamma - \alpha$ coincidences. The TOF line shape for 0.5-5 MeV alpha-particles was measured using the beta-delayed alpha-particle emission from ^8Li . We ensured that ^8Li nuclei were produced in the same setup (via $^7\text{Li}(d,p)^8\text{Li}$ reaction) and we used similar 9 MeV deuterium beams. In this way the time response function of our system (i.e. centroid and width) was measured for alpha-particles that were originated in the target. As we discuss later, this control experiment with the beta-delayed alpha-particle emission of ^8Li was essential for the data analysis and reduction.

The energy calibration of the Si surface barrier detectors were performed using ^{241}Am (5.486 MeV), $^{208,209}\text{Po}$ (5.074 MeV, 4.838 MeV), and ^{148}Gd (3.183 MeV) sources. We monitored gain shifts in the detectors every six to seven hours, using these sources. The response of the surface barrier detectors to low energy alpha-particles was measured with the $^{10}\text{B}(n,\alpha)^7\text{Li}$ reaction. These measurements were carried out every four or five days to check the low energy response of the detectors. This source was prepared in the following way: a thin layer ($\sim 5\mu\text{g}/\text{cm}^2$) of $^{10}\text{B}_2\text{O}_3$ was evaporated onto a 0.13 mm thick tungsten foil. A 3 inch thick paraffin was placed inside the vacuum chamber, to thermalize fast neutrons from a Pu-Be

source, situated outside the vacuum chamber. The tungsten foil was located in front of the detector with $^{10}\text{B}_2\text{O}_3$ side facing the surface barrier detectors. Alpha-particles and ^7Li nuclei were detected. This reaction [Aj84, Aj85] produces alpha-particle lines of 1.471 MeV (93%), and 1.775 MeV (7%), and ^7Li lines of 0.841 MeV (93%), and 1.014 MeV (7%), spanning the region of interest, as shown in Fig. 14.

The total counting time for the duration of these experiments is approximately three weeks for the 250 keV thick targets (for 1.75 MeV alpha-particles), four weeks for the 170 keV thick target, and two weeks for 400 keV thick targets.

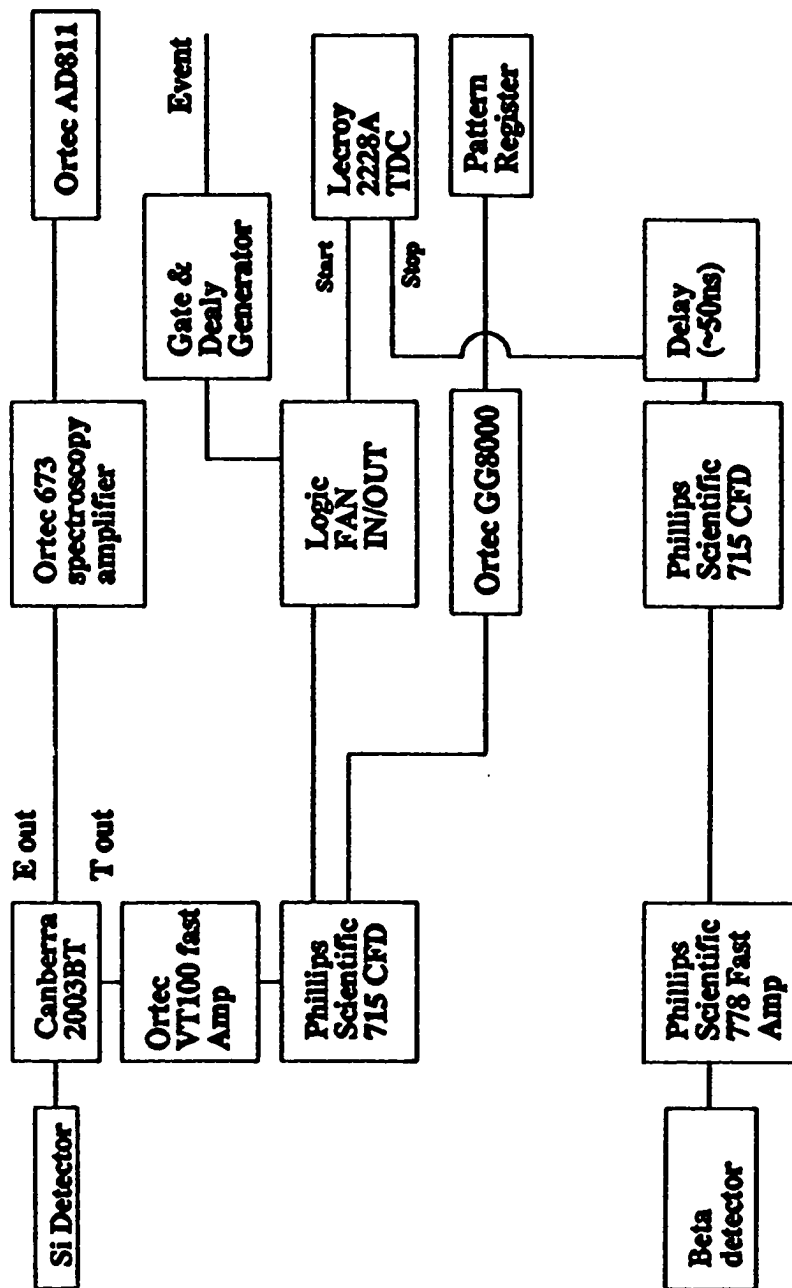


Figure 13: Schematics of Electronics, with nine identical Si detector channels and twelve identical beta-particle detector channels. (Canberra 2003BT≡preamplifier, CFD≡Constant Fraction Discriminator, AD811≡ADC, GG8000≡Gate and Delay Generator.)

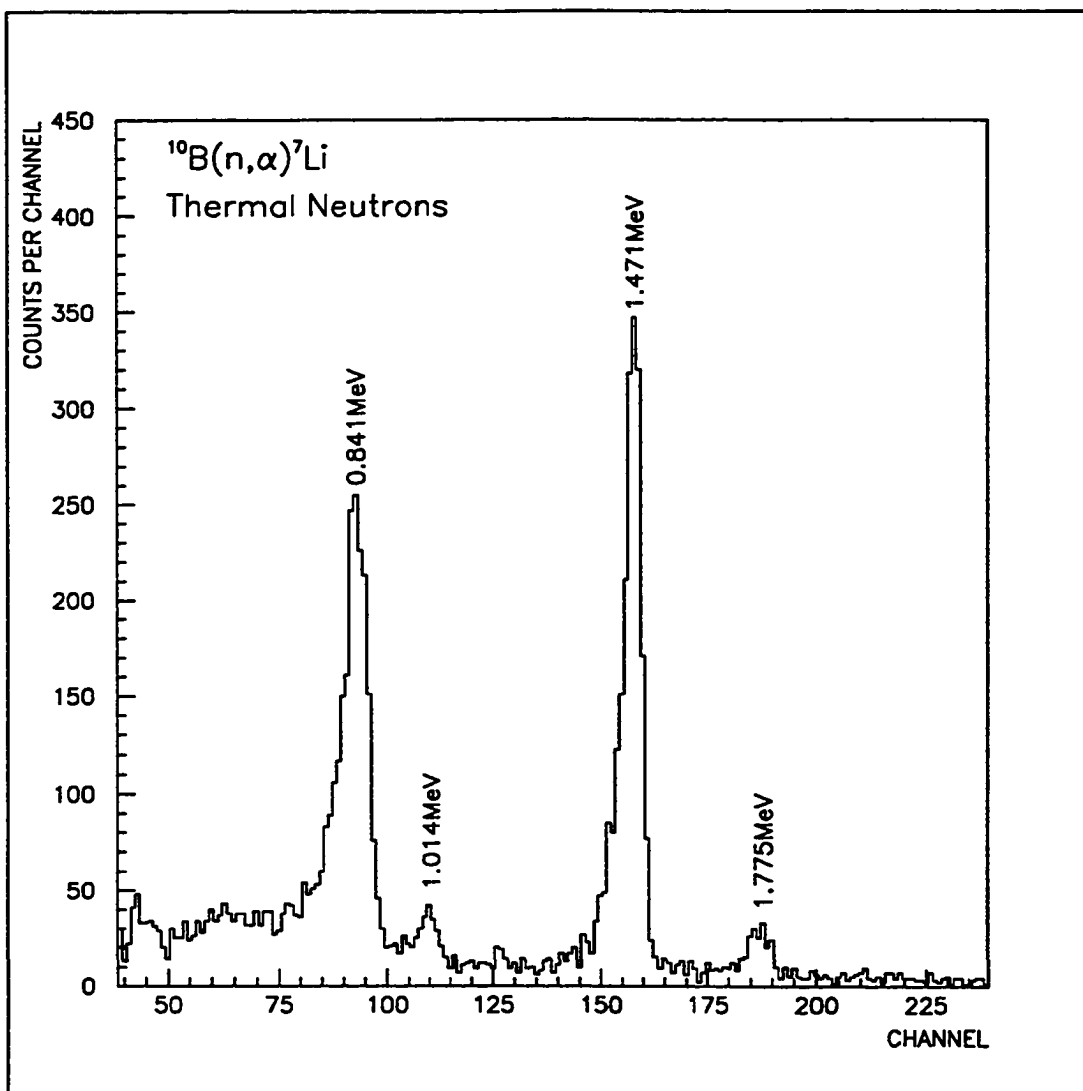


Figure 14: Typical charged particle spectrum from $^{10}\text{B}(n, \alpha)^7\text{Li}^*$ reaction. Fast neutrons, from a Pu-Be neutron source, were thermalized using paraffin, and react with isotopically enriched $^{10}\text{B}_2\text{O}_3$.

3.1.2 TARGET PREPARATION

The ^{15}N targets were prepared by Jet Process Laboratory Inc, Science Park, New Haven. The targets were prepared by sputtering Ti metal onto backing substrates, with isotopically enriched ^{15}N gas introduced into the chamber at the same time. During the sputtering process, Ti metal combines with the ^{15}N gas and Ti^{15}N are deposited on the electrically conductive substrate. Three type of targets were used:

1) Ti^{15}N on Au and C backing, with total target thickness of 400 keV for 1.75 MeV alpha-particles, and 480 keV for 0.9 MeV alpha-particles.

2) Ti^{15}N on Au and C backing, with total target thickness of 250 keV for 1.75 MeV alpha-particles, and 300 keV for 0.9 MeV alpha-particles.

3) Ti^{15}N on Au backing, with total target thickness of 170 keV for 1.75 MeV alpha-particles, and 200 keV for 0.9 MeV alpha-particles.

The thickness of Ti^{15}N and its gold backing were determined by measuring the excitation function of the 429 keV resonance of the $^{15}\text{N}(p, \alpha\gamma)^{12}\text{C}$ reaction. Proton beams were produced by a 1 MV model JN van de Graaff accelerator of the Sloane Physics Laboratory at Yale University. The thickness of the gold backing was measured by determining the shift of resonance energy, when the target was reversed relative to the proton beam (i.e the gold facing the beam). The 429

keV resonance corresponds to the $J^\pi=2^+$ state in ^{16}O at $E_x=12.530$ MeV, which decays into $^{12}\text{C} + \alpha + \gamma$. The target thickness measurements were performed before and after the targets were used in our experiment. In Fig. 15 we show four typical excitation curves for the targets. The top two panels are the measurements made before the target was exposed to the intense deuteron beam, and lower panels are after they were exposed to about 1 Coulomb of 9 MeV deuteron beam (about one week of beam time). No significant deterioration of the target was observed. A 10-15% increase in both Ti^{15}N and Au thickness, between the measurements before and after it was exposed to the beam, was observed. This is attributed to the combined effect of measurement accuracy, the non-uniformity in the target, and the existence of a slight ripple in the target. It was not enough to disturb the outcome of the experiments.

The empirical stopping power formula of protons discussed by Ziegler [Zi77b, Zi77a] is given by:

$$S = \frac{S_1 S_2}{S_1 + S_2} \quad (19)$$

where S is the stopping power in unit of $\text{ev}/(10^{15} \text{ atoms}/\text{cm}^2)$, for example, $S_1 = 3.35E_p^{0.45}$ and $S_2 = \frac{1683}{E_p} \ln \left[1 + \frac{1900}{E_p} + 0.02513E_p \right]$ for protons in nitrogen, where E_p is the energy of incident of protons in unit of keV; $S_1 = 2E_\alpha^{0.548}$ and $S_2 = \frac{2.982 \times 10^4}{E_\alpha} \ln \left[1 + \frac{1.811 \times 10^4}{E_\alpha} + 0.00437E_\alpha \right]$ for alpha-particles in nitrogen, and E_α the energy of incident alpha-particles in unit of keV. From this formula, it is

straightforward to calculate the ratio of energy loss for 1 MeV alpha-particles in $Ti_xN_yO_z$ and 430 keV protons to be:

$$\frac{\Delta E_\alpha}{\Delta E_p} = 5.22 \frac{x + 0.992y + 1.811z}{x + 1.072y + 1.966z} \quad (20)$$

Due to oxygen impurity in the nitrogen gas (0.01%) and the active nature of titanium to combine with oxygen, a slight portion of Ti was in the oxide form. We determined the stoichiometry (percentage of oxygen) for the target material, by using Rutherford backscattering of alpha-particles; $x=1.0\pm0.3$, and $y=0\pm0.3$. The alpha-particles were again produced by the 1 MV model JN van de Graaff accelerator of the Sloane Physics Laboratory at Yale University. In the thin target case (170 keV thickness), we found that it was necessary to introduced approximately 20% of oxygen in the target (i.e. $y=0.2$) to give the thin foil extra strength. However the total target thickness for alpha-particles is very insensitive to the exact stoichiometry of the target, as demonstrated in equation 20. It leads to only 5% fluctuation in estimating energy loss, due to different choices of stoichiometry. Therefore the target thickness for alpha-particles was determined from equation 20 and was estimated to be accurate to better than 10%.

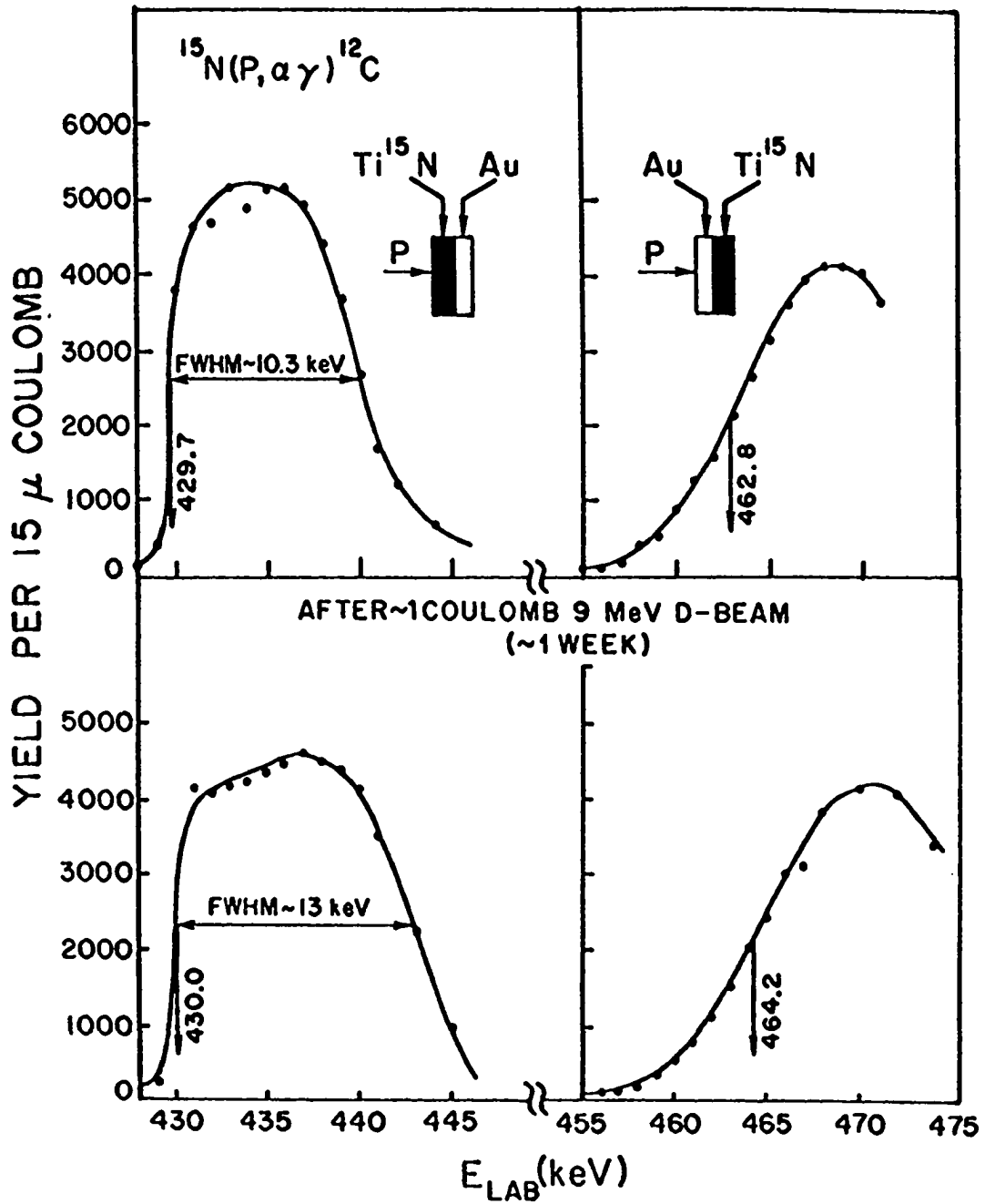


Figure 15: The excitation function of the $^{15}\text{N}(p, \alpha \gamma)^{12}\text{C}$ reaction using our Ti^{15}N target. The top panel was measured before the target was exposed to the beam and the lower panel after it was exposed to an integrated beam dose of 1 Coulomb of 9 MeV deuterium.

3.1.3 EXPERIMENTAL RESULTS

In Fig. 16 we show a typical singles alpha-particle spectrum, exhibiting the decay of the broad 1^- state at 9.6 MeV, and a low energy tail from the beta-particles that dominates the region of interest. Consequently, we used TOF information to reduce the large background from beta-particles. The spectrum constructed from TOF information is plotted together with singles data in Fig. 17. The use of the TOF information clearly enables us to significantly reduce the background from the beta-particles, as can be seen in Fig. 17. The detailed procedure for data analysis is discussed below.

There are 9 alpha-particle detectors and 12 beta-particle detectors, with total of 108 pairs of $\alpha - \beta$ coincidence. The energy gain matching of the Si detectors, was performed using the calibration spectra discussed in the previous section. And the TOF of all 108 pairs were matched using the beta-delayed alpha-particle decay from ^8Li . After matching, all 108 pairs were summed to a one 2-dimensional histogram as shown in Fig. 18 (TOF vs Energy of alpha-particles). It was found that the exact matching of detectors in energy and TOF was essential for reducing the level of background. And in this case the time calibration spectra of ^8Li and energy calibration spectra of the $^{10}\text{B}(n,\alpha)^7\text{Li}$ reaction were essential. Note the TOF axis has the usual reversed direction, since TOF starts with the slow alpha-particles and stops with the fast beta-particles. The broad peak at around channel 165 of energy and channel 140 of TOF is from the decay of the broad 1^- state at 9.6 MeV. The band across the TOF direction arises from random coincidence,

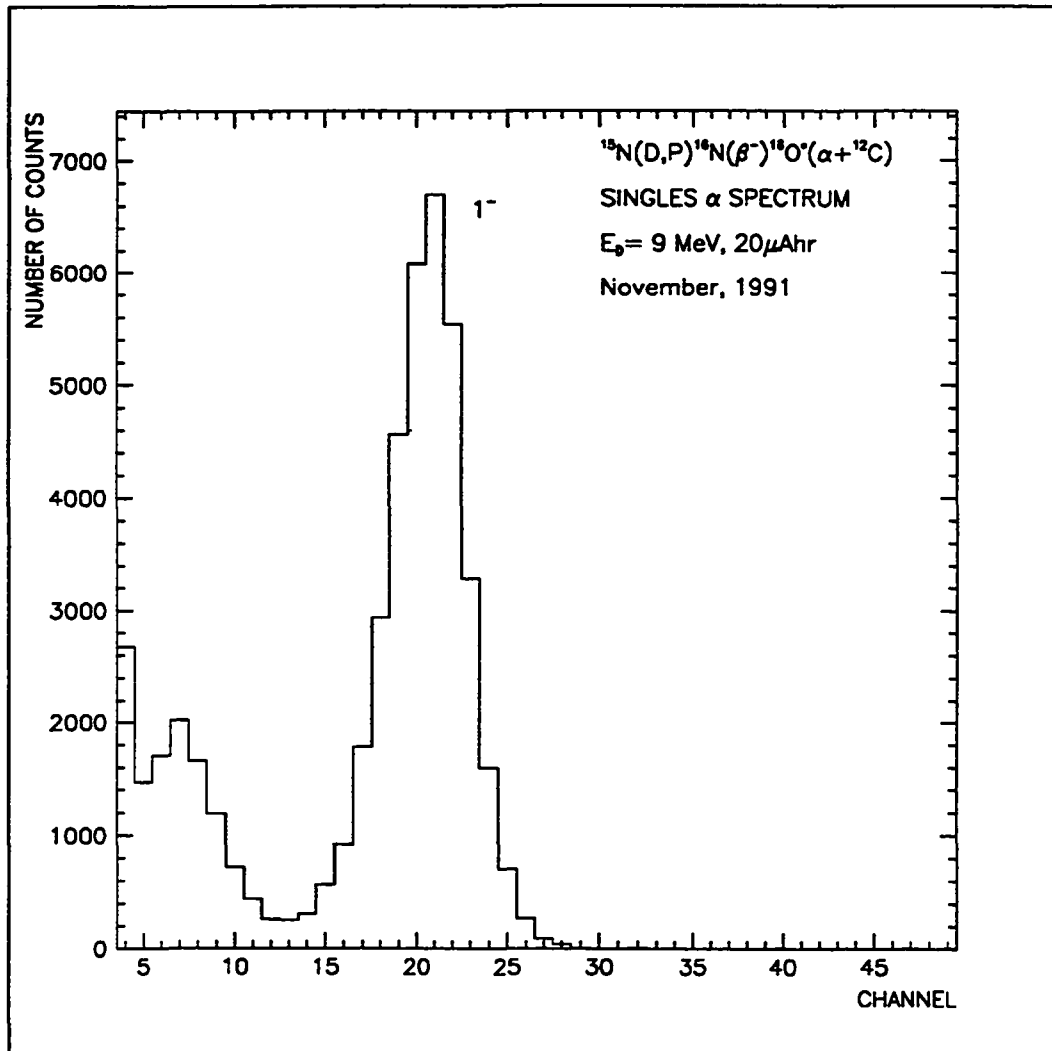


Figure 16: Singles alpha-particle spectrum. The peak around channel 20 corresponds to the decay of broad 1^- state at 9.6 MeV and the low energy structure is due to energy deposited by beta-particles. The cutoff at channel 5 is the electronics threshold.

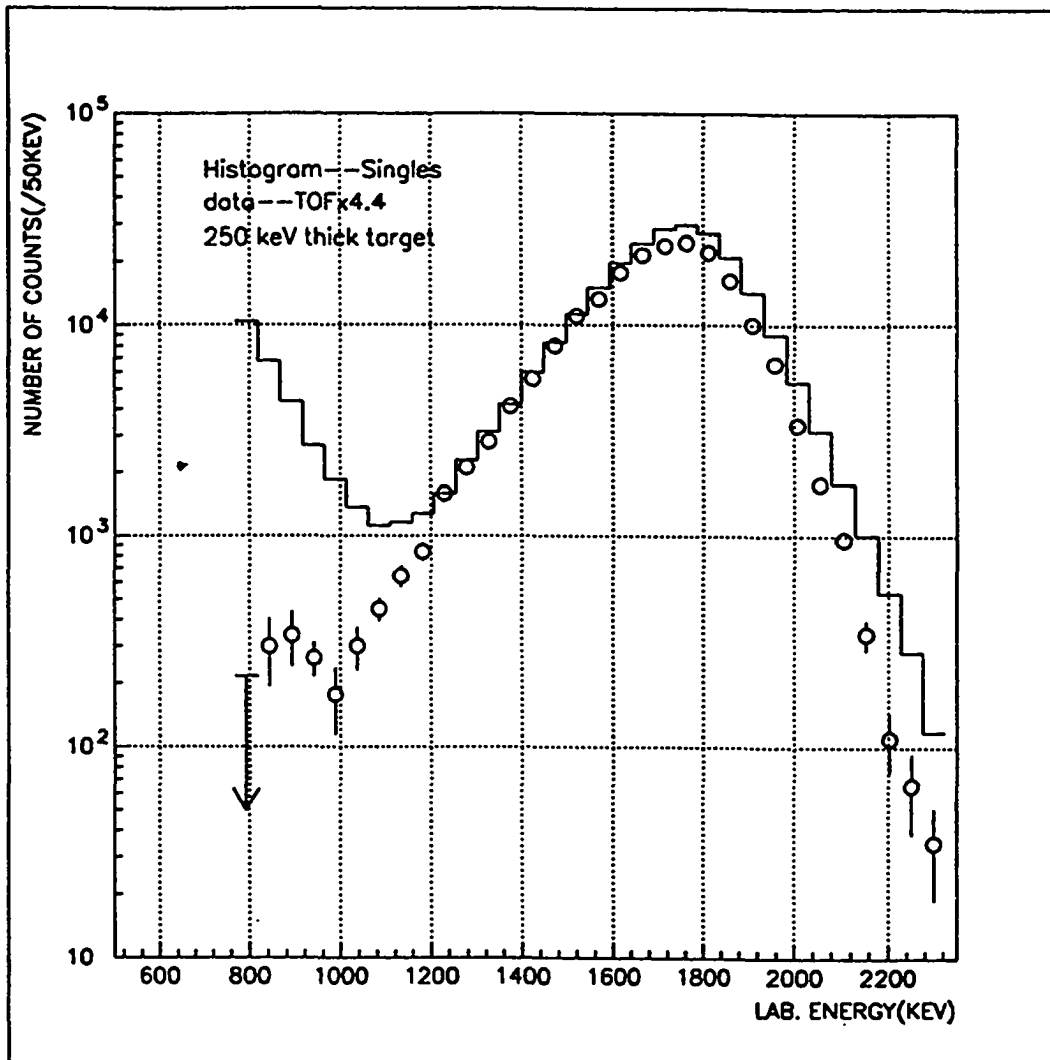


Figure 17: Beta-delayed alpha-particle spectrum constructed from TOF information in comparison with the singles alpha-particle spectrum.

since the beta-particle detection efficiency is not 100%. The events below channel 70 of energy are from beta-particles, which deposit enough energy in the surface barrier detectors. The structure at low energy and around channel 160 of TOF, is from coincidences between beta-particles and gamma-rays. In this case, the beta-particles deposited enough energy in the surface barrier detector and beta-delayed gamma-rays were detected in the plastic scintillators. This peak defines the prompt time ($t=0$) for our system. In the lower panel of the same figure we show the same two-dimensional histogram for the beta-delayed alpha-particle decay of ^8Li . The time-of-flight trajectory defined by the decay of ^8Li yields a time-of-flight calibration of the system. Hence the position and the width of the TOF trajectory were defined for alpha-particles originating in the target with energies of 0.5-5 MeV.

To further reduce the background, we have sliced this 2-dimensional histogram in energy bins, and projected onto the TOF axis. The TOF projection spectra, for all energy bins, were fitted according to the position and width defined by the ^8Li data. The binning of the 2-dimensional spectra were in 50 keV for 250 keV thick target, 80 keV for 400 keV thick target and 120 keV for 170 keV thick target. The bin size was varied so as to increase the statistical significance of the data. In Fig. 19 we show an example of 6 such slices with 50 keV energy bin, for the 250 keV thick target.

In Fig. 19 (top panel), we show the TOF projection for the energy slice at the maximum of the broad 1^- resonance. The TOF projection, as expected, shifts

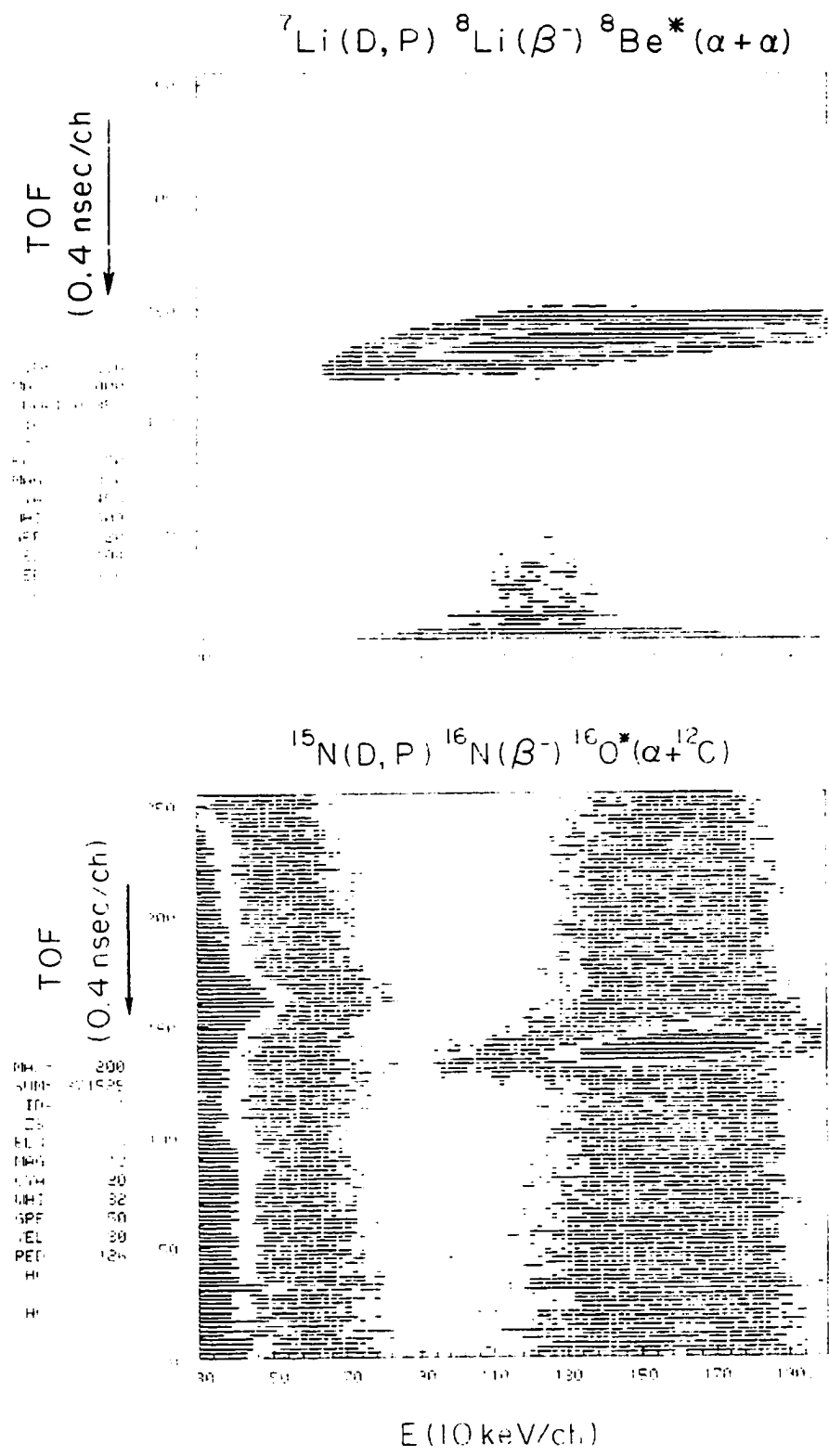


Figure 18: Time-of-Flight vs the Energy of alpha-particles following beta-decays of ${}^{16}\text{N}$ and ${}^8\text{Li}$. Data for ${}^{16}\text{N}$ with a 250 keV thick target.

to the left (longer times) when the energy decreases. In the lower panels, the structure around channel 42 is due to $\beta-\gamma$ coincidence, which defines the $t = 0$ of the system (also seen on the 2-dimensional histogram). Note that the low energy tail in the Si detector due to partial charge collection (dashed line), is well resolved from the true low energy signal. The position of TOF projection for each energy slice, follows the line shape of TOF as defined by time-of-flight of decays following ${}^8\text{Li}$, as shown in Fig. 20. In Fig. 21, we show an example of 6 such slices with 80 keV energy bin, for the 400 keV thickness target.

For the data measured with the 250 keV thick target, at the broad resonance region, the signal to background ratio of the TOF spectra is significantly better than 10 to 1, while at the low energy region, the signal to background ratio is typically of 2 or 3 to 1 (see Fig. 19). The sensitivity of our experiment, as defined by the background, displayed in Fig. 19, is for a branching ratio for a beta-decay at the level of 2×10^{-9} around 1 MeV. In Fig. 22 we show one such TOF projection around 1 MeV, for the sum of the two ‘cleanest’ surface barrier detectors where we achieved the sensitivity for a branching ratio of the beta-decay of better than 7×10^{-10} .

The beta-delayed alpha-decay spectrum was constructed by integrating the appropriate peak in TOF projection spectra (as defined by the ${}^8\text{Li}$ data) for each energy slices. In Fig. 23 we show the extracted spectrum for data taken with the 250 keV thick target. Note that the signal to background ratio for data point at $E = 940$ keV is approximately 9 to 1, 1.5 to 1 for data point at $E = 890$ keV, 2

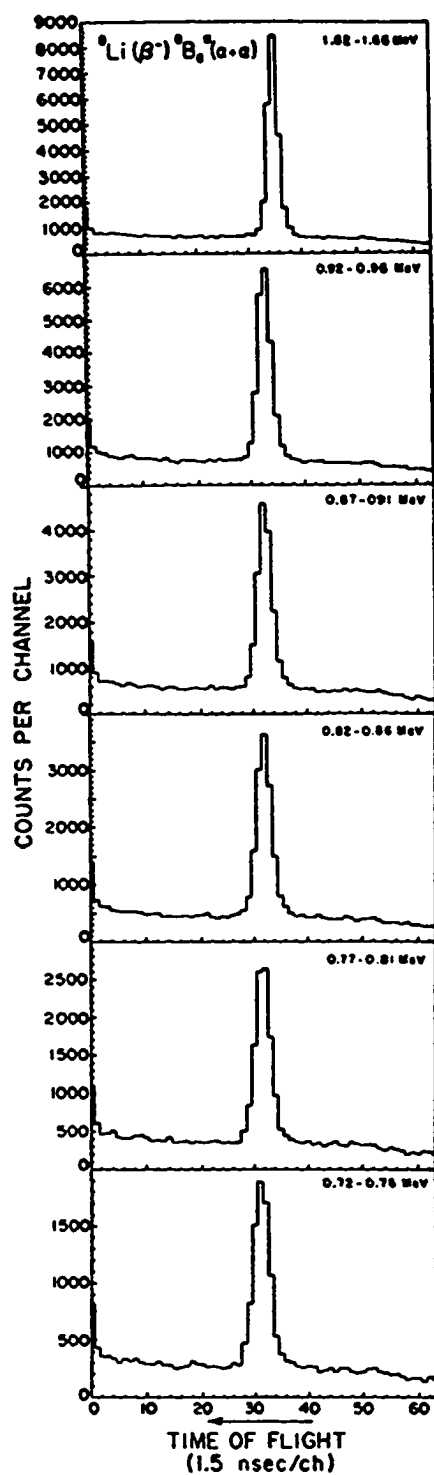


Figure 20: Spectra of Time-of-Flight of alpha-particles, produced by projecting a 50 keV energy slice onto the TOF axis. Data for ${}^8\text{Li}$ produced in ${}^7\text{Li}(d,p){}^8\text{Li}$.

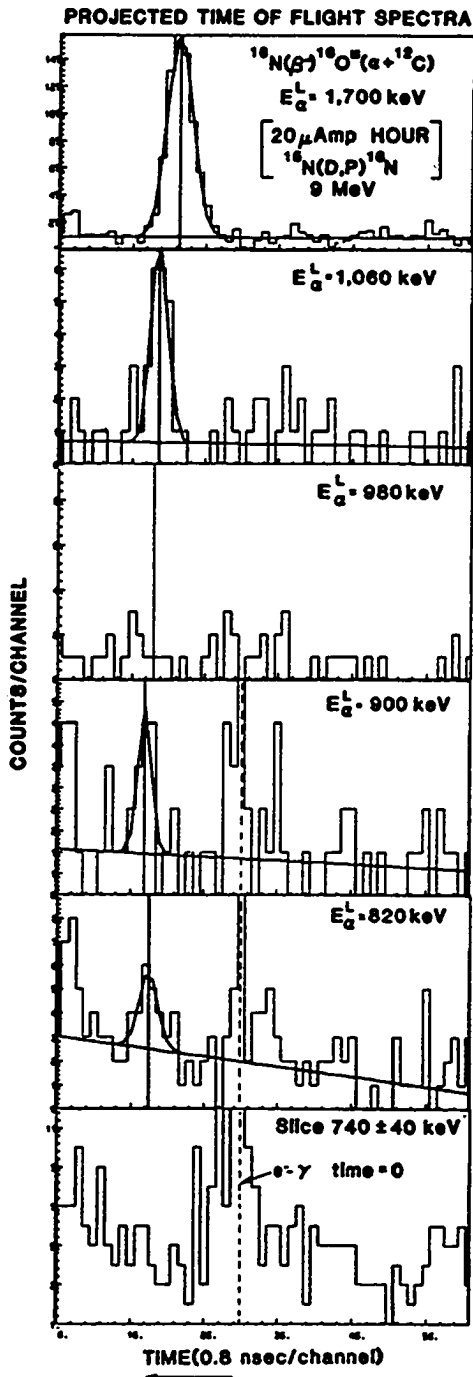


Figure 21: Spectra of Time-of-Flight of alpha-particles, produced by projecting a 80 keV energy slice onto the TOF axis. Data for ^{16}N with a 400 keV thick target.

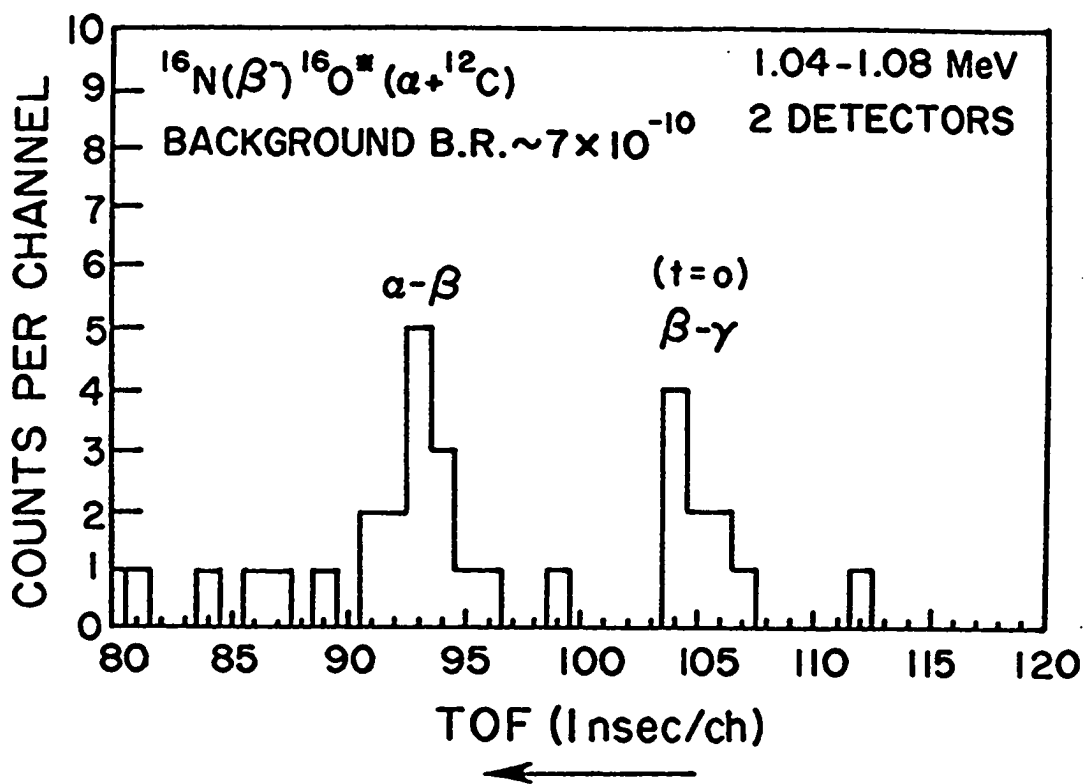


Figure 22: Spectra of Time-of-Flight of alpha-particles. The sum of the two 'cleanest' surface barrier detectors is used, exhibiting a sensitivity for beta-decay branching ratio in the range of 10^{-10} .

to 1 at $E = 840$ keV, 1.5 to 1 at $E = 790$ keV and 1 to 1 at 740 keV. The signal at $E = 690$ keV is consistent with zero, therefore we assign an upper limit at $E_L = 640$ keV according to the fluctuation in background. This upper limit at $E = 640$ keV is a 2σ limit (90% confidence).

To further identify whether the alpha-particle decay was associated with ^{16}N , we performed two measurements. First, we have performed the same measurement using target with natural nitrogen (99.63% of ^{14}N). After approximately 2 days we observed only beta-particles up to $E_L=600$ keV. In addition we measured the lifetime of the beta-delayed alpha-particle emission. The lifetimes for alpha-particles of energy higher than $E_L = 1.1$ MeV, are shown in Fig. 24, exhibiting the characteristic 10 seconds lifetime of ^{16}N . The lifetime of the secondary peak was also measured and is shown in Fig. 25. It is also consistent with the mean lifetime of ^{16}N of 10 seconds. Note that the small number of counts observed at the beginning of the lifetime curves is associated with oscillation in the arm before it comes to rest.

Several corrections were applied to the beta-delayed alpha-particle spectrum due to our experimental techniques. The major contributions to the line shape of the raw spectrum arise from the energy loss in the target. Another correction is due to the energy dependence of the efficiency of our beta-particle detectors, caused by the finite threshold.

First, as discussed earlier, the thickness of the targets were measured individually and the energy loss for alpha-particles in our target was calculated according to

Ziegler's semi-empirical formulae [Zi77b, Zi77a]. The beta-delayed alpha-particle spectrum was then corrected for the energy loss of alpha-particles in the target. In section 3.2 we discuss an experiment at Michigan State University that allowed us to extract this energy loss from data. Note that the energy loss varies over the region of interest by approximately 20%. Second, a correction at the higher energy end ($E_L \geq 1.25$ MeV) was applied, due to the threshold of beta-particle detectors (~ 100 keV) and the energy dependence of the efficiency of TOF. This correction was obtained by comparing the singles spectrum and the spectrum obtained from TOF. In Fig. 26, we plot the ratio of the two spectra (i.e. TOF divided by the singles). The high energy cutoff is due to the threshold of the beta-particle detectors, and the low energy cutoff reflects the reduction of the background from the beta-particles.

The beta-delayed alpha-particle spectrum of ^{16}N , after the correction for energy loss in the target and the TOF efficiency, is shown in Fig. 27, for the 250 keV thick target. In Fig. 28, it is shown for the 170 keV thick target, and in Fig. 29 for the 400 keV thick target. The experimental data are listed in Appendix A. The uncertainties in determining the energy of the alpha-particles is 40 keV for the 250 keV thick target, 60 keV for the 400 keV thick target and 25 keV for the 170 keV thick target, respectively.

A quick inspection of the measured three spectra shown in Figs. 27- 29, indicates that the observed line shape is asymmetric, much more than would be expected from a decay of an isolated state (see Figs. 6- 8). This line shape is due to the

energy resolution (foil thickness) of our experiment. In the following section, we discuss measurements and data reduction that we employed to understand this effect and correct for it.

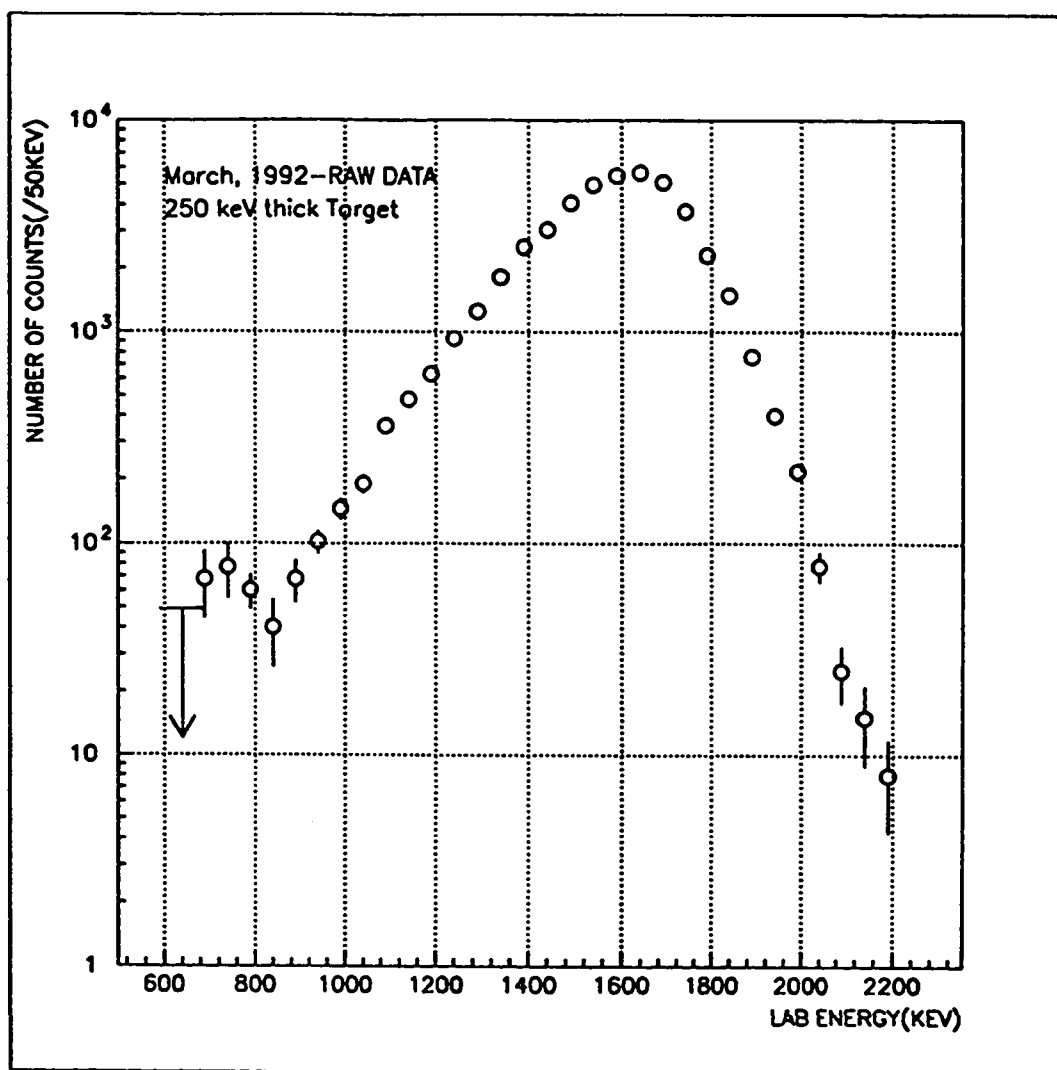


Figure 23: Uncorrected Beta-delayed alpha-particle decay of ^{16}N , constructed from TOF, for 250keV thick target. Note the resolution of the experimental system is 250keV at $E=1.75$ MeV, the binning of the data is 50keV. Therefore each data point receive significant contribution from its next neighbor and some contribution from its next to next neighbor.

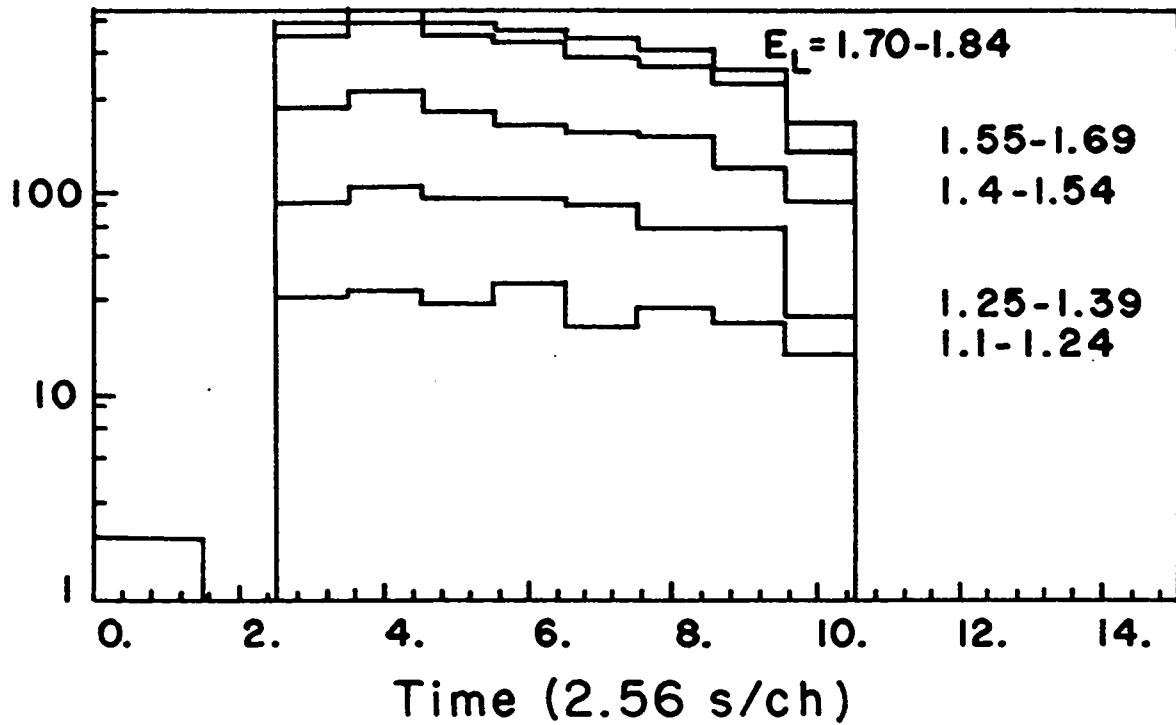


Figure 24: Lifetime measurement of beta-delayed alpha-particles. The observed lifetime is consistent with 10 seconds mean lifetime of ^{16}N .

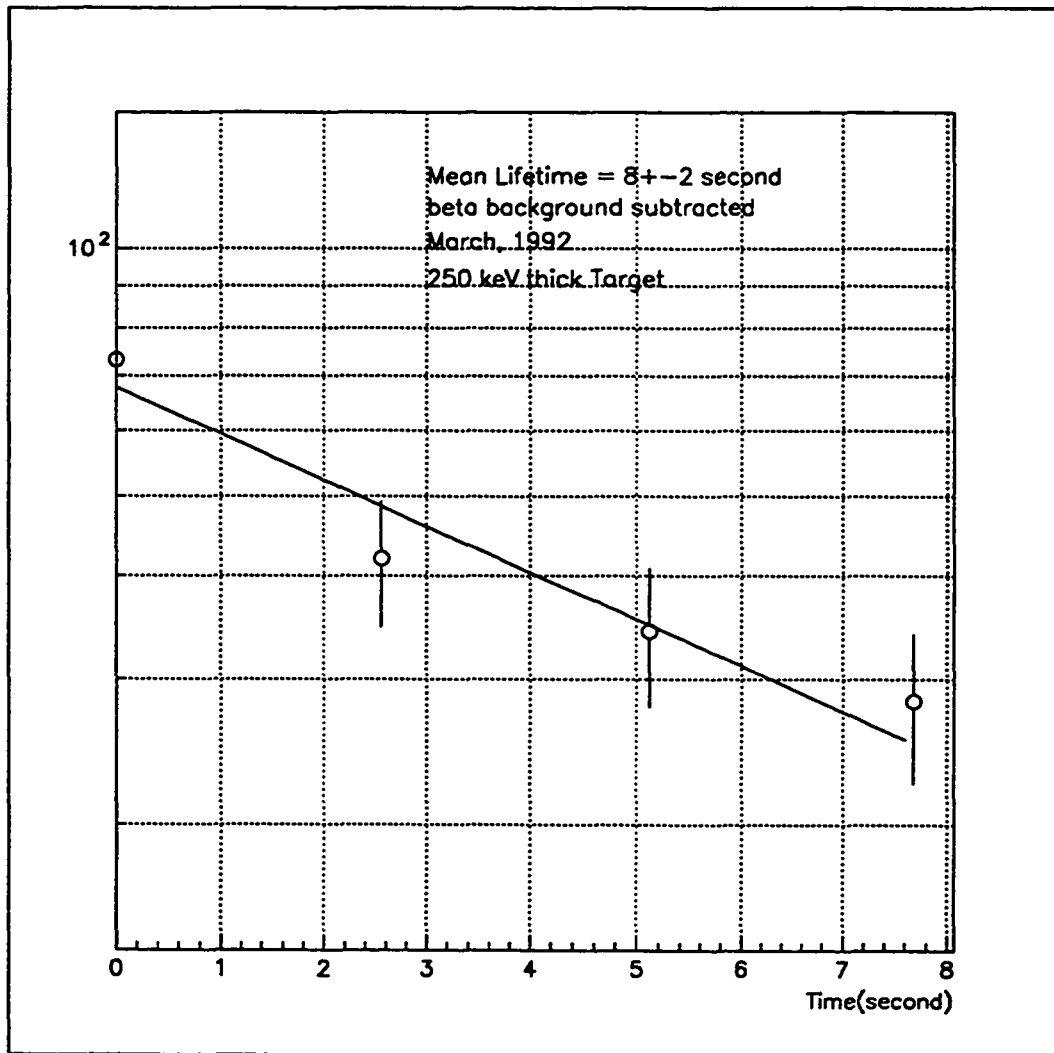


Figure 25: Lifetime measurement of beta-delayed alpha-particles within the low energy secondary maximum. Contribution of background from beta-particles was subtracted. The observed lifetime is consistent with 10 seconds, expected for ^{16}N decay.

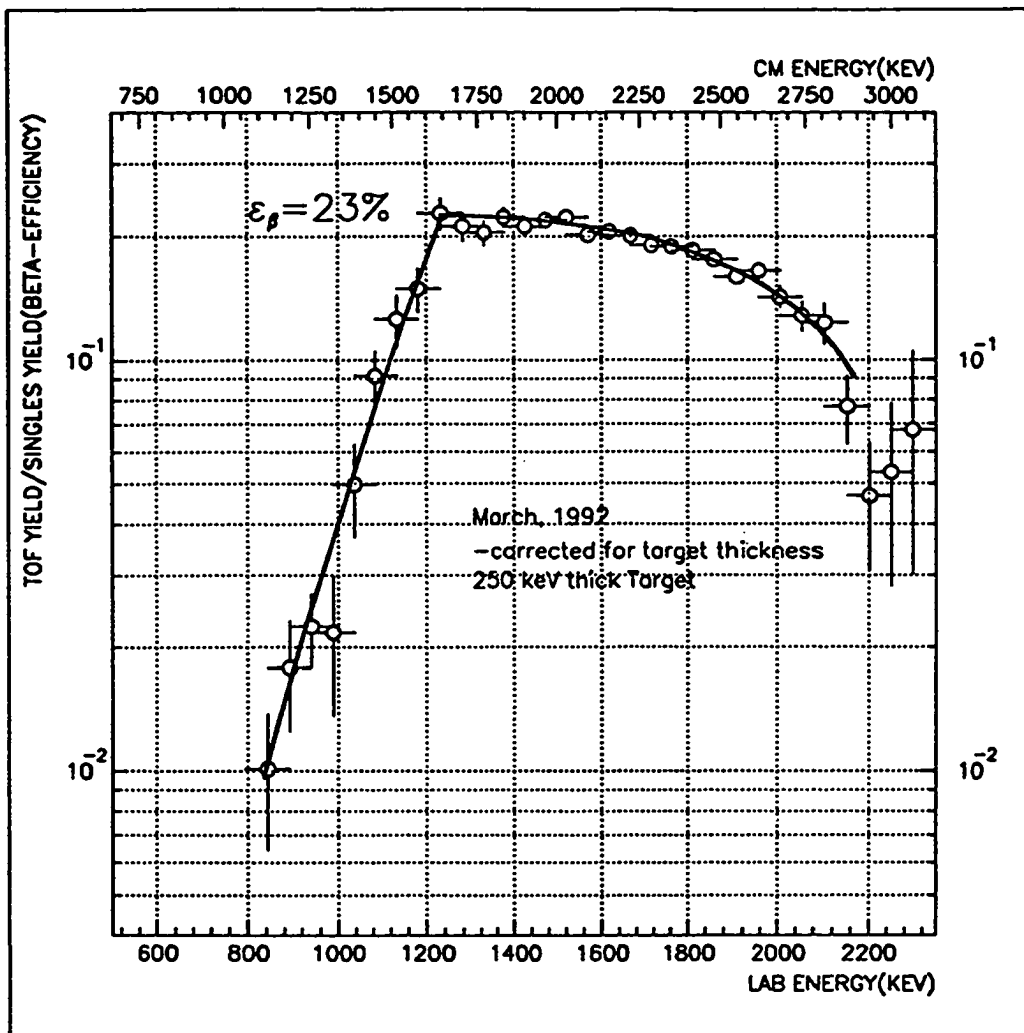


Figure 26: The ratio of number of events from TOF and singles as a function of alpha-particle energy. The high energy cutoff is due to the efficiency of TOF detection. The low energy cutoff shows the background reduction by using TOF.

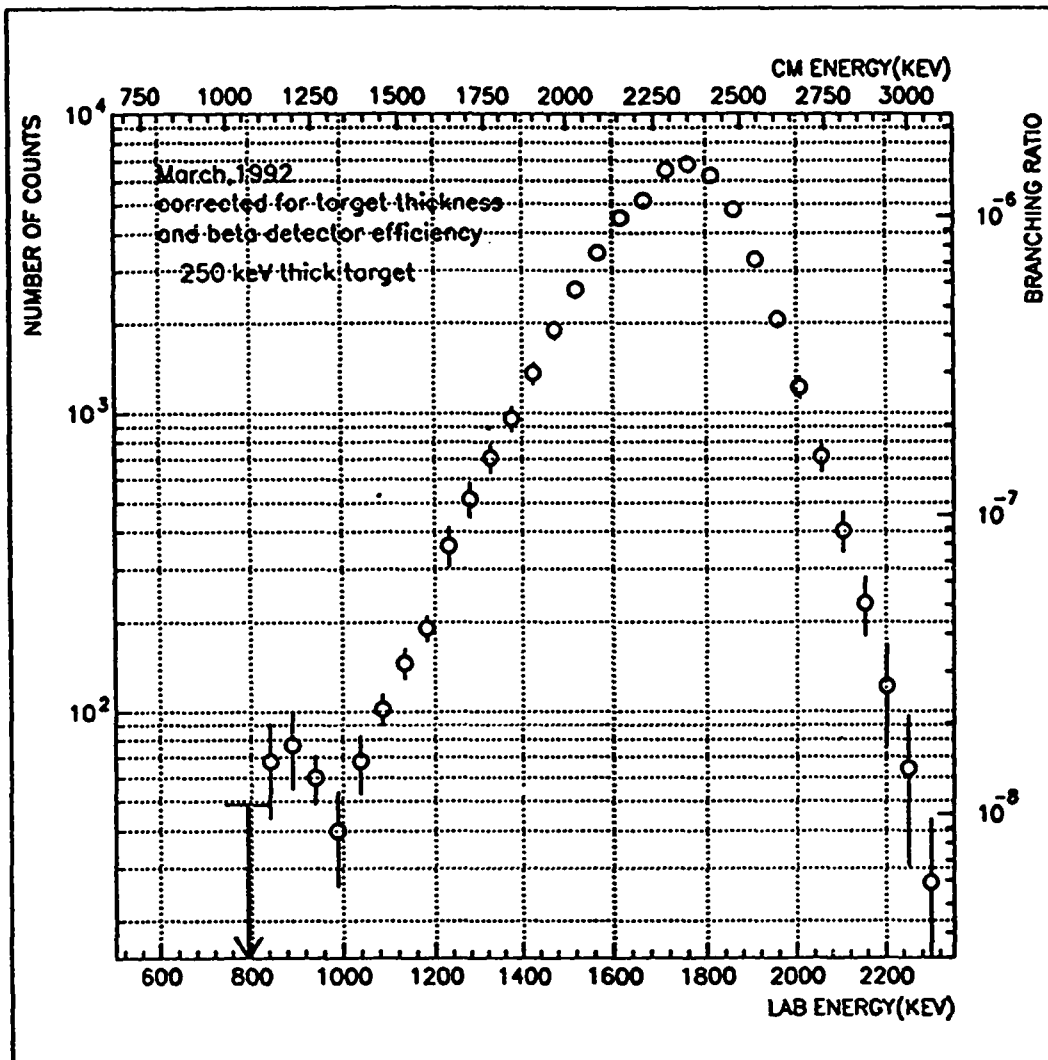


Figure 27: Beta-delayed alpha-particle decay spectrum of ^{16}N , for 250 keV thick target. Correction for target thickness and TOF efficiency were applied. Note the resolution of the experimental system is 250keV at $E=1.75\text{MeV}$, the binning of the data is 50 keV. Therefore each data point receive significant contribution from its next neighbor and some contribution from its next to next neighbor.

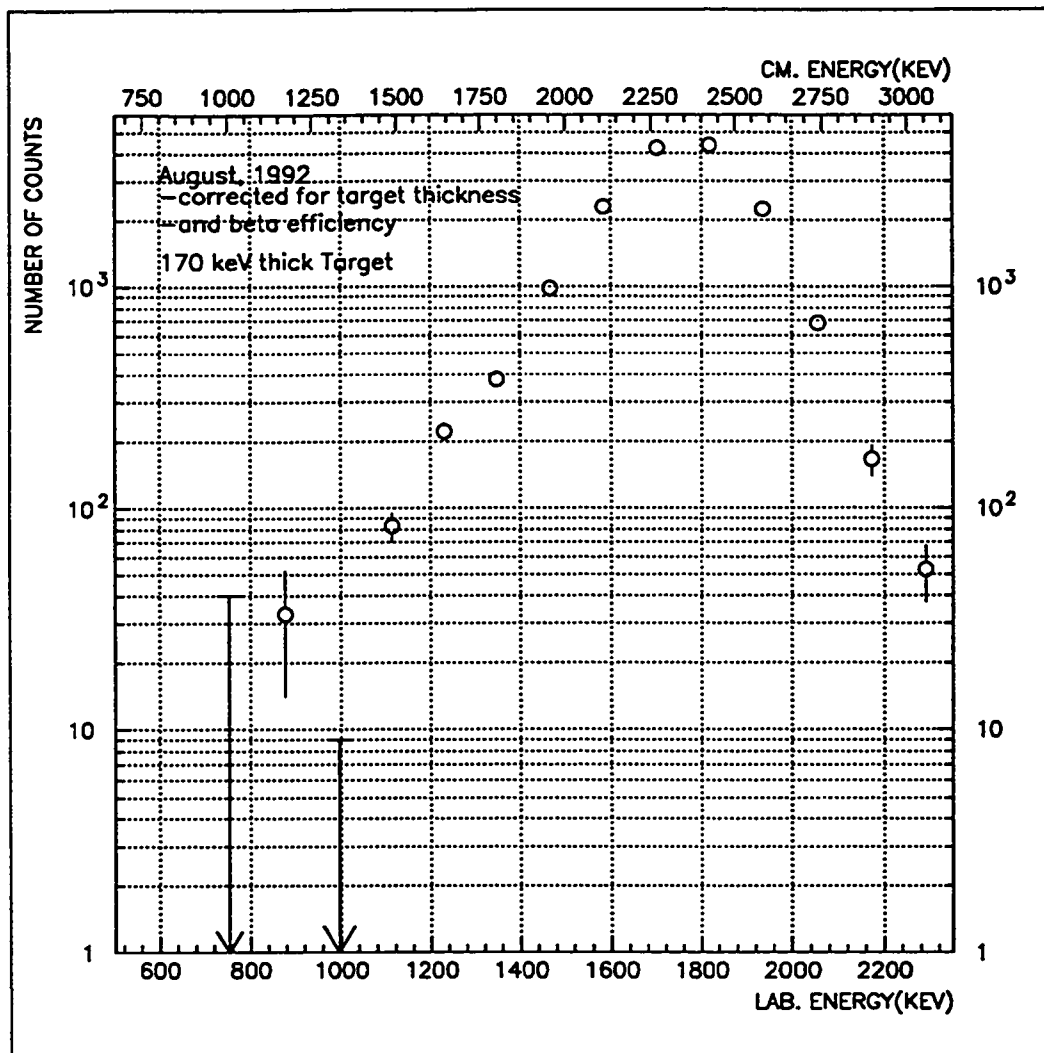


Figure 28: Beta-delayed alpha-particle decay spectrum of ^{16}N , for 170 keV thick target. Correction for target thickness and TOF efficiency were applied.

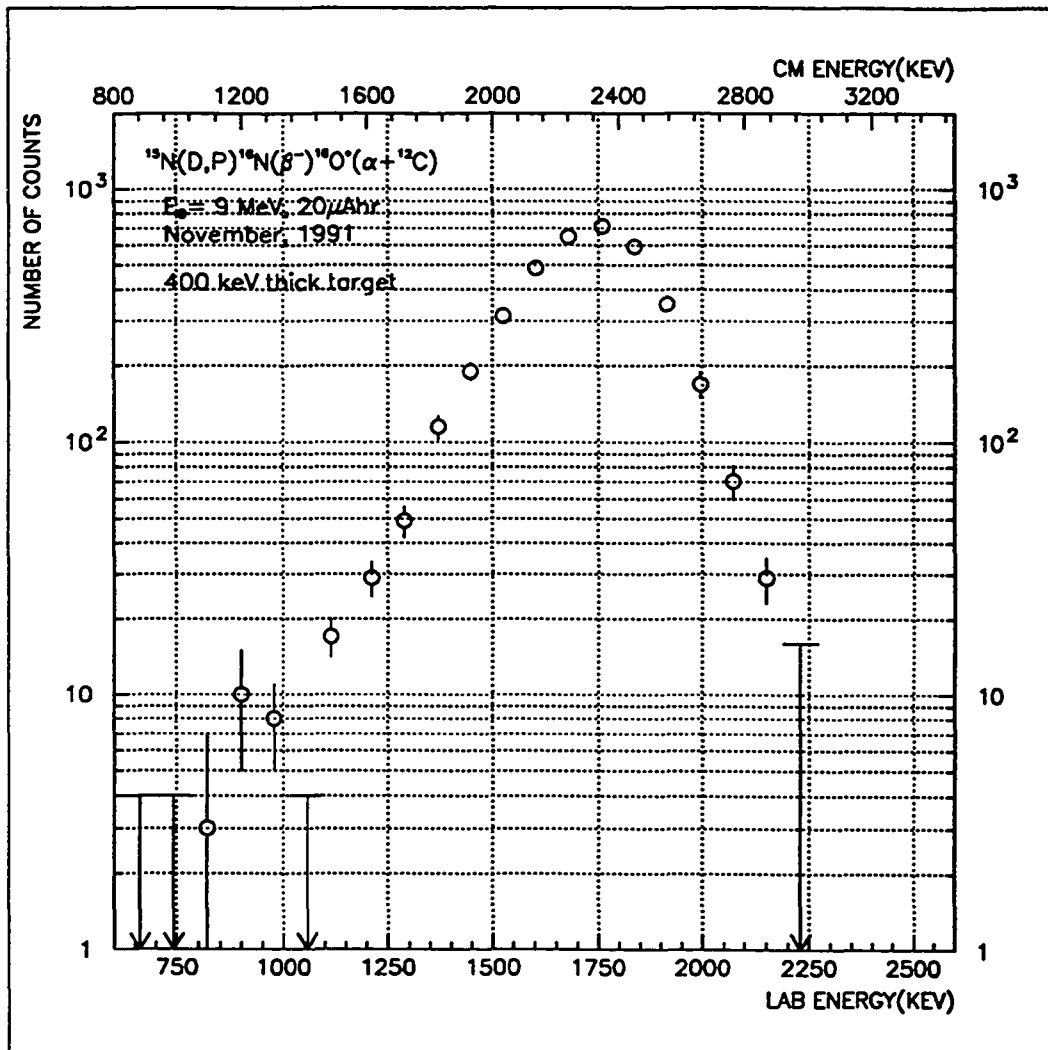


Figure 29: Beta-delayed alpha-particle decay spectrum of ^{16}N , for 400 keV thick target. Correction for target thickness and TOF efficiency were applied.

3.2 THE EXPERIMENT AT MSU: Precision Measurement Of Beta-delayed Alpha-particle Emission Of ^{16}N To The Broad 1^- State At 9.6 Mev in ^{18}O

As discussed in the previous section, we have been able to measure the low energy beta-delayed alpha-particles emission of ^{16}N at Yale University, with a sensitivity sufficient to exhibit the low energy secondary maximum. The Yale experiment however, leaves a few open questions.

The centroid of the decay from the unbound 1^- state was shifted at the Yale experiment due to the energy loss in the target. In order to determine experimentally the unshifted peak position, we have measured it in the absence of a foil. This measurement is essential in order to confirm our calculated energy loss in the foil and the correction that we apply to our data due to energy loss in the foil. We were also unable to measure, in the Yale experiment, the beta-decay branching ratio to this broad 1^- state.

In order to address these questions, we performed an experiment, at the National Superconducting Cyclotron Laboratory at Michigan State University. In the MSU experiment, the centroid of the beta-delayed alpha-particle spectrum and the beta-decay branching ratio were accurately measured. The centroid of the beta-delayed alpha-particle spectrum was measured by implanting ^{16}N nuclei in Si detectors. In this way, a 'zero' target thickness experiment is performed as the decay of alpha-particles is measured inside the detector. In addition, in this procedure the

background due to neutrons associated with the beam is low, which allowed us to employ gamma-ray detectors and measure the absolute branching ratio of beta-delayed alpha-particle emission of ^{16}N . The experimental technique is very similar to an experiment that we performed earlier at MSU to measure the beta-delayed alpha-particle emission of ^{18}N [Zh89].

3.2.1 EXPERIMENTAL PROCEDURES

The ^{16}N nuclei were produced using 80 MeV/u ^{18}O beams, from the Michigan State University (MSU) K1200 superconducting cyclotron, on ^9Be targets. The secondary nuclei were mass analyzed and separated from the rest of the reaction products using the A1200 isotope separator (see Fig. 30), and transported into the focal plane of the isotope separator. The secondary nuclei were then implanted into an array consisting of four silicon surface barrier detectors. The efficiency for the beta-delayed alpha-particles decaying inside the detector is nearly 100% and the losses, due to edge effects, are estimated to be below 1.5% [Zh89].

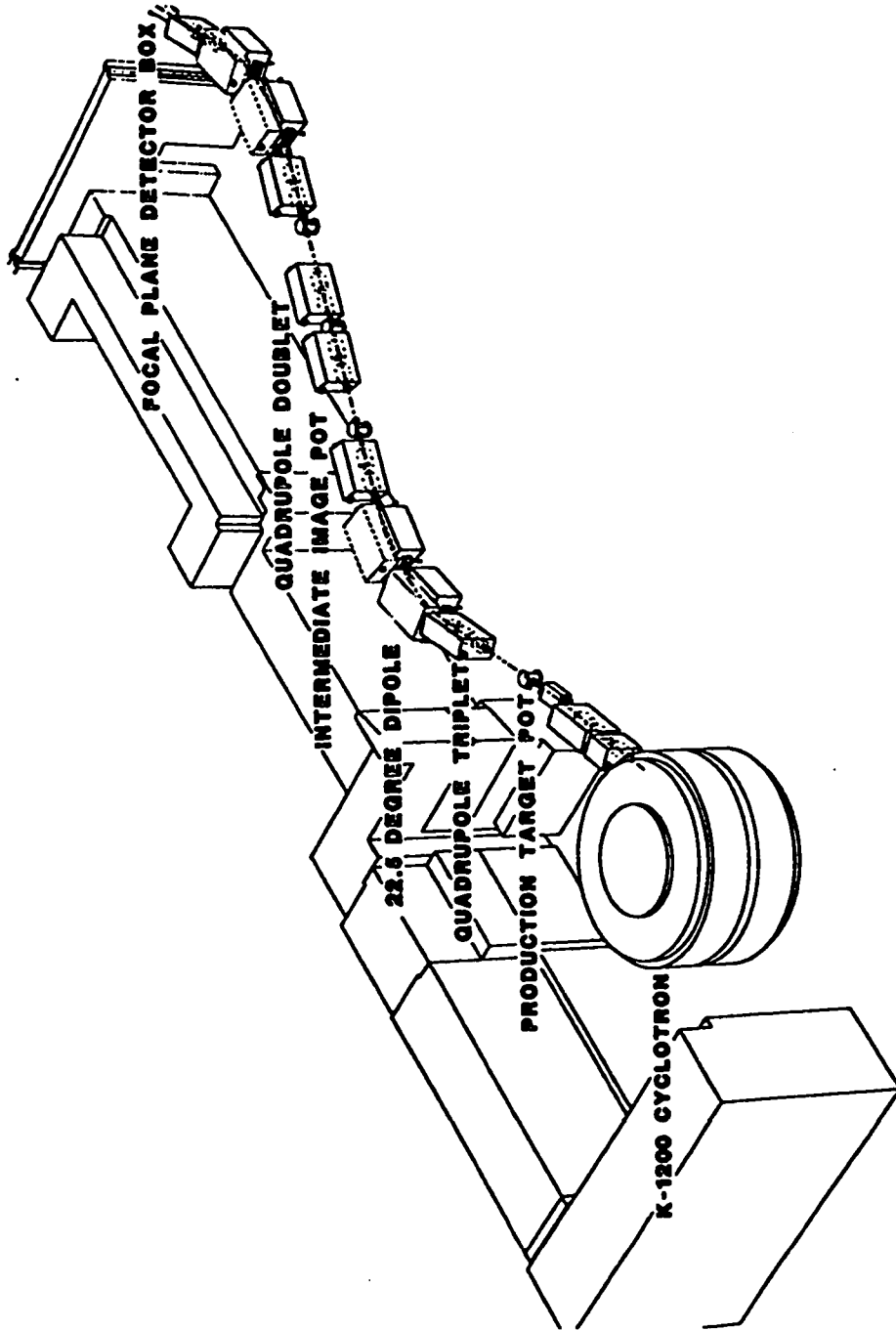
The tuning of the A1200 isotope separator was achieved by measuring the time-of-flight of the particles traversing several thin plastic scintillator detectors along the beam line in combination with a 2-dimensional position sensitive parallel-plate avalanche counter (PPAC) and a PIN-diode (ΔE for incoming particles), placed in front of the silicon telescope. In Fig. 31 we show a two-dimensional histogram of energy output from PIN diode versus the time-of-flight (TOF) of the secondary beams. In Fig. 32 we show the profile of incoming secondary beam and

its projections along the horizontal and vertical axis. The obtained beam spot size was on the order of 1-2 cm. The PPAC edge effects are observed in the figures (the size of the PPAC detector is 10cm×10cm).

In Fig. 33, we show the focal plane detector system. It consists of a two-dimensional position sensitive PPAC and PIN diode as discussed earlier, a silicon telescope and a high purity high efficiency Ge gamma-ray detector. Note that the efficiency of the Ge detector, for the full energy peak at 1.3 MeV, is 120% with respect to a 3" NAI(Tl) cylindrical detector. The silicon telescope consists of four thin (25-50 μm) silicon surface barrier detectors tilted at 45° to the incident beam, in order to increase the effective thickness of the thin Si detectors and to stop the ^{16}N nuclei. The incoming ^{16}N beam was degraded using aluminum foils before entering the telescope. The beam was collimated in order to remove edge effects in the silicon detectors. The Ge detector was collimated by a 4 inch lead collimator, see Fig. 33, so the Ge detector viewed the telescope array only. The absolute and relative efficiencies of Ge detector were measured using calibrated ^{65}Zn (1.116 MeV), ^{228}Th (2.614 MeV) and ^{152}Eu sources. The efficiency was measured at the location of each Si detector, with typical absolute efficiency for 1 MeV gamma-rays of 0.1%. The Ge detector collimation efficiency was measured and found to be better than 99% at 1 MeV.

The beam-on and beam-off cycles were controlled by 2 gate and delay generators in a loop and with a period of 10.00 seconds. The signals from each alpha-particle detector were sent into two different spectroscopy amplifiers and two separate

channels on different ADC modules. The signals for beam-on and beam-off cycles were recorded by a bit-pattern register. The data were recorded, event by event, onto magnetic tapes and analyzed offline at the A.W. Wright Nuclear Structure Laboratory at Yale University.



A1200 Isotope Separator

Figure 30: The A1200 Isotope Separator at the National Superconducting Cyclotron Laboratory at the Michigan State University (MSU).

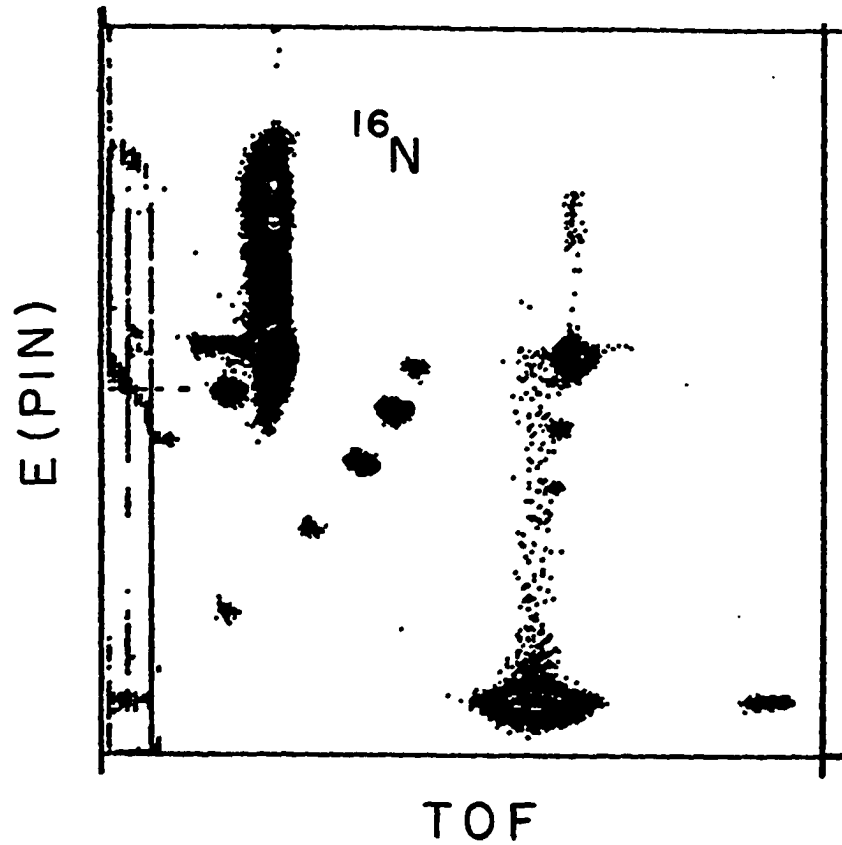


Figure 31: Energy output of PIN diode (ΔE of incoming particles) versus the TOF of incoming particles. This gives particle identification.

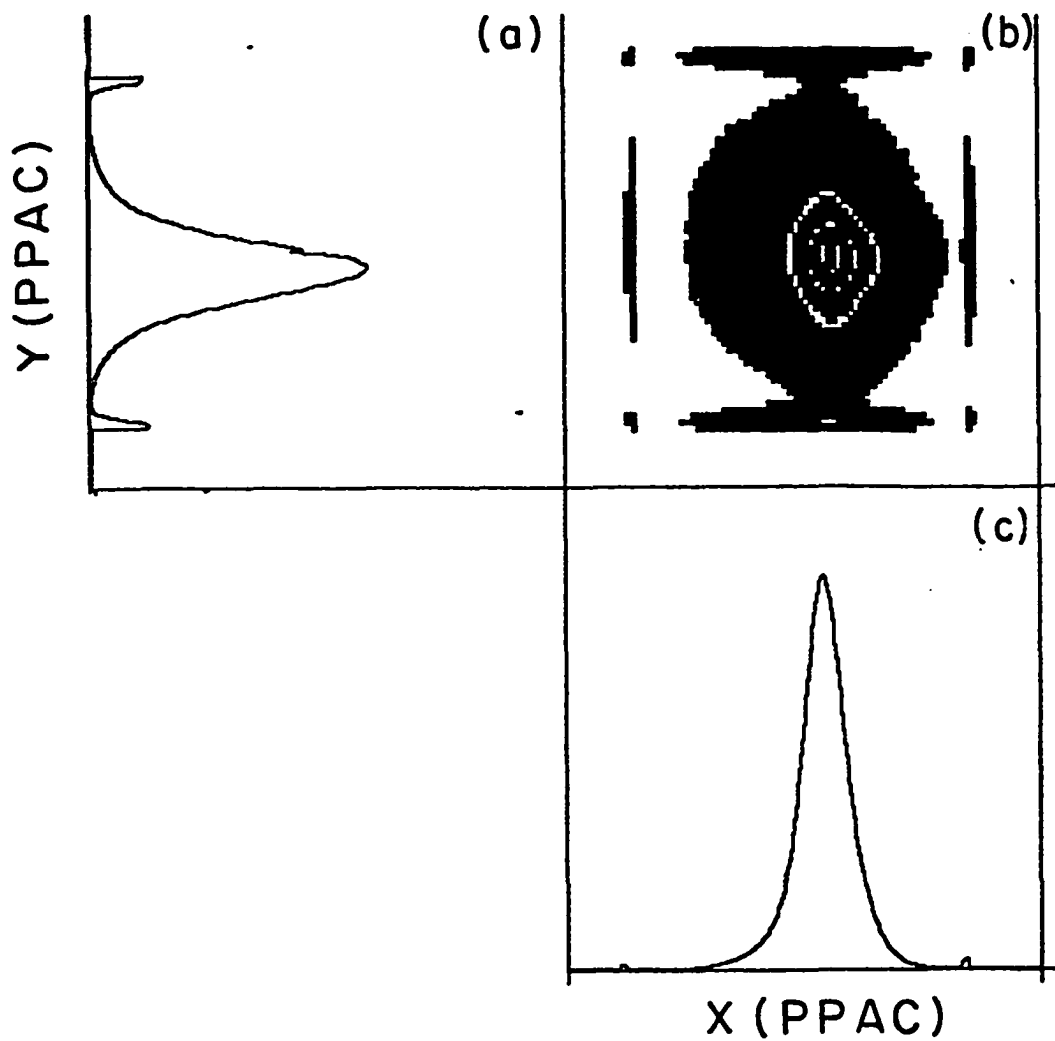


Figure 32: Profile of the secondary ^{16}N beams as measured by the two-dimensional position sensitive PPAC, (a) and (c) are projections onto the vertical and horizontal axis respectively. The edge effects can be seen on the figures.

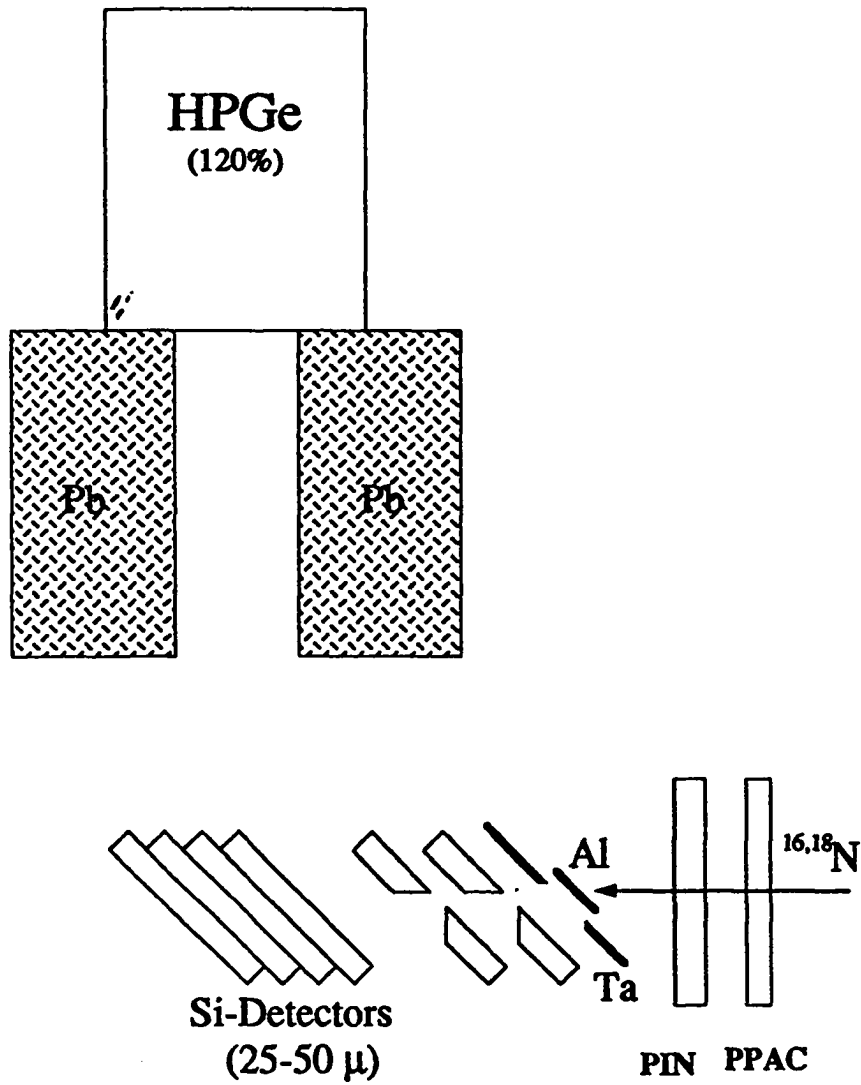


Figure 33: Experimental setup for the experiment conducted at MSU.

3.2.2 EXPERIMENTAL RESULTS

The energy spectra of secondary beams were measured during the beam-on period. In Fig. 34 we show a resulting two-dimensional histogram of E2 vs E3, where E2 and E3 are energy signals from the second and third Si detectors in the telescope array, see Fig. 33. In the lower panel of the same figure, we also show the same data with a veto imposed by the output of the subsequent detector E4, the fourth detector in the telescope. The number of ^{16}N nuclei stopped in the detector E3 was deduced from Fig. 34.

During the beam-off period, the beta-delayed alpha-particle decay spectrum was collected for each detector. Energy calibration of Si detectors, in the beam-off mode, was achieved by examining the beta-delayed alpha-particle emission from ^{18}N [Zh89]. The spectrum of the beta-delayed alpha-particle emission of ^{18}N includes two narrow-width lines at 1.40 and 1.82 MeV and one broad line at 2.8 MeV [Zh89].

In Fig. 35 we show the beta-delayed alpha-particle spectrum from ^{16}N , measured in this experiment. The beta tail at low energies was fitted with a smooth function. The spectrum with background from beta-particles subtracted, is shown in Fig. 36. The centroid energy for the broad distribution is measured to be (2.35 ± 0.05) MeV, confirming our calculated energy loss in our foils. Note that the beta-delayed alpha-particle spectrum measured at MSU exhibits a more symmetric line-shape than the one obtained at the Yale experiment, with a target of finite

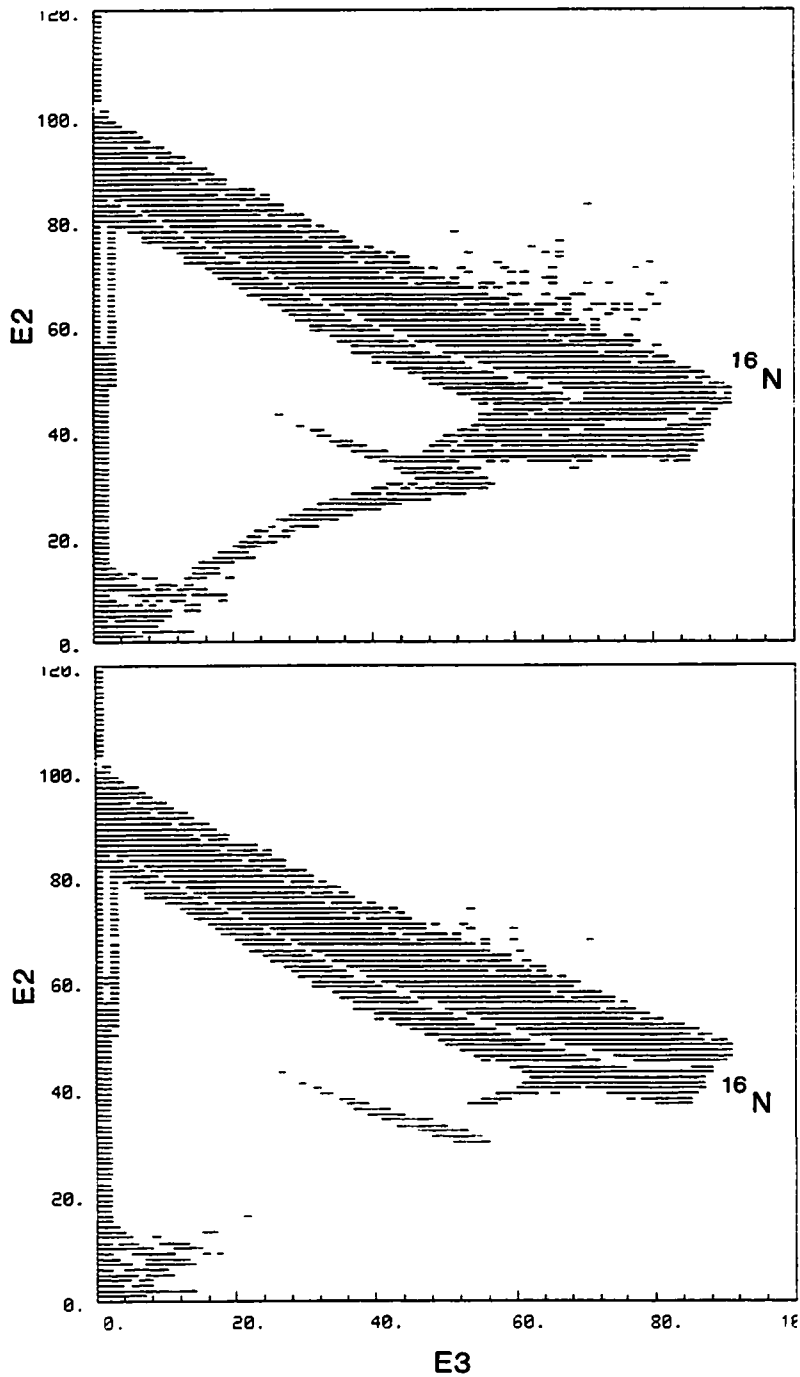


Figure 34: Typical two-dimensional spectrum of E2 vs E3 where E2 and E3 are the energies deposited in the second and third detector in the telescope(top), and E2 vs E3 with a veto on E4 as discussed in text(bottom).

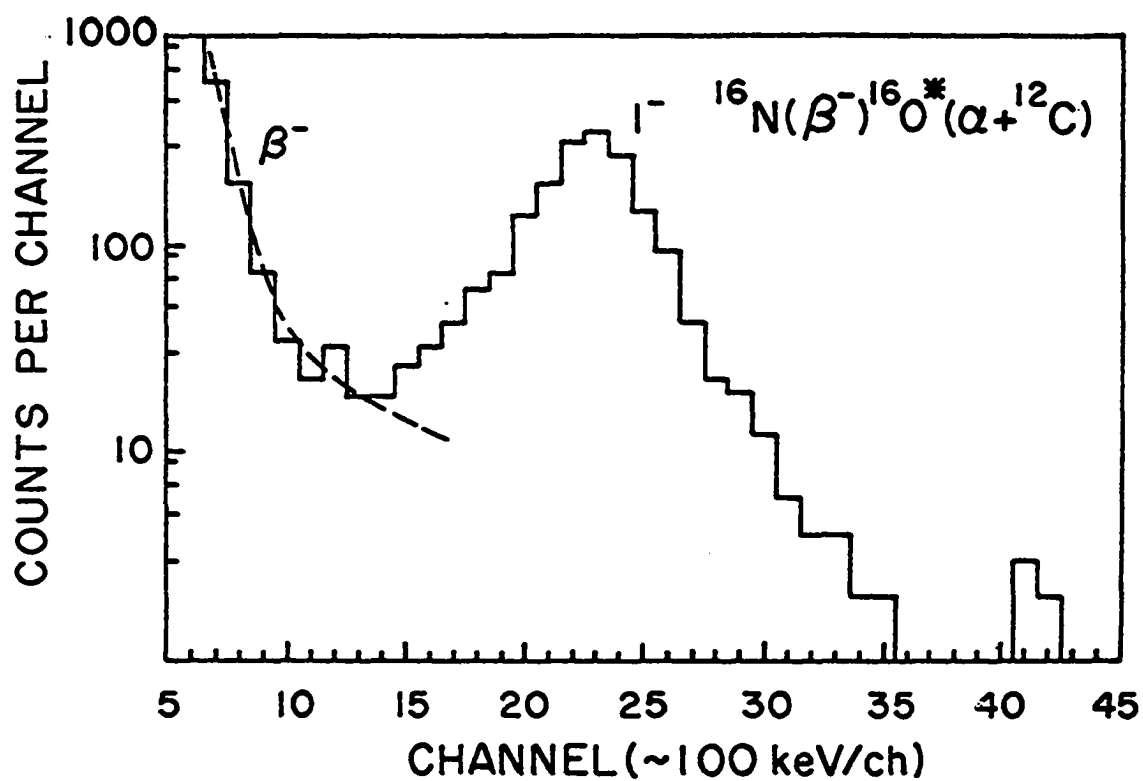


Figure 35: Typical spectrum of beta-delayed alpha-particles from ^{16}N .

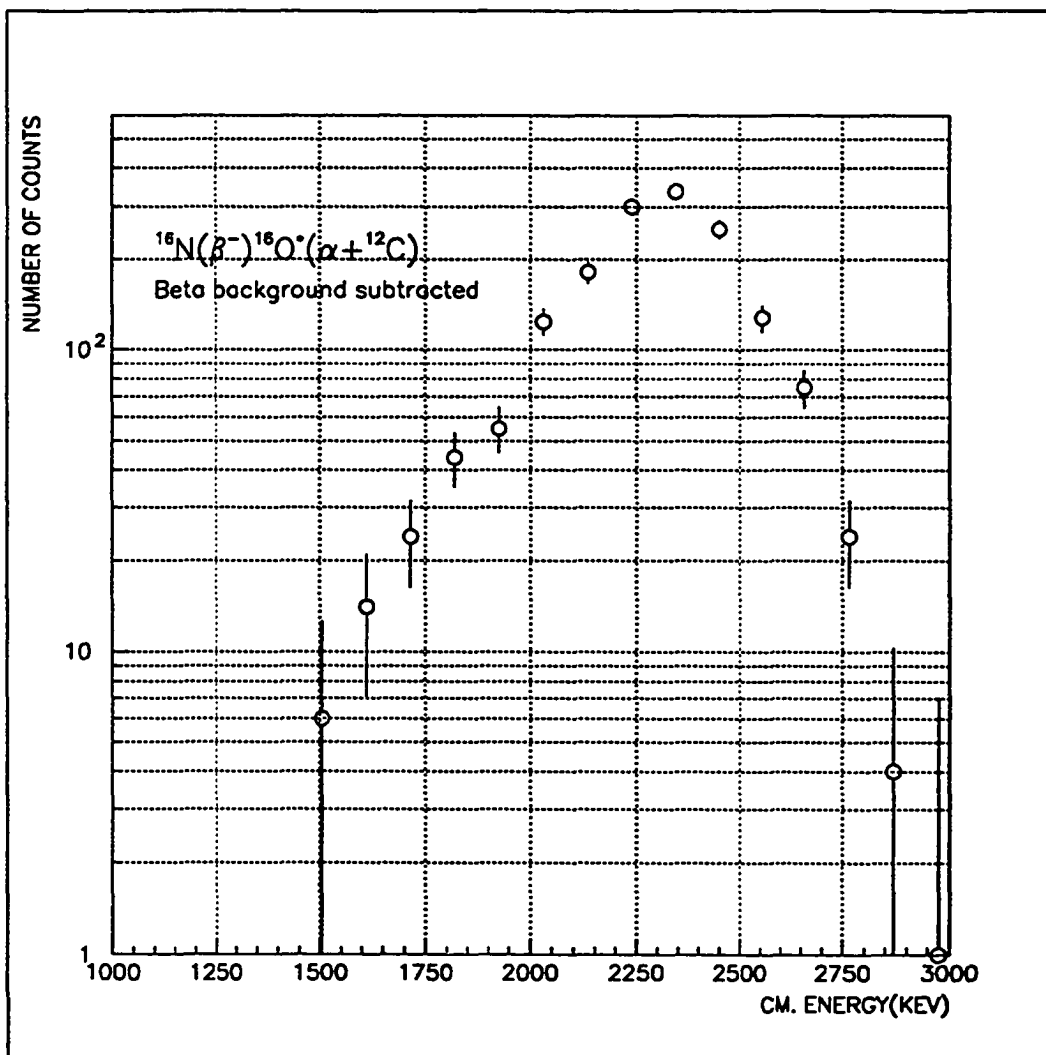


Figure 36: Typical spectrum of beta-delayed alpha-particles from ^{16}N , with beta-particle background subtracted.

thickness (see Fig. 27). However, due to the large background from beta-decays inside the Si detector, one can not observe the low energy secondary maximum in the MSU data. The measured centroid of the alpha-particle spectra and the beta-decay branching ratio are in agreement of the previously published results. Our measured lineshape exhibits a low energy tail due to partial energy collection of alpha-particles. The beta-delayed gamma-ray emission spectrum was collected using Ge detector and is shown in Fig. 37.

The branching ratio of the beta-delayed alpha-particle decay from the broad 1^- state was extracted by comparing the yield of the alpha-particles to the yield of gamma-rays. The ratio of beta-delayed alpha-particle decays to the beta-delayed 2.746 MeV gamma-ray was measured to be $(1.7 \pm 0.3) \times 10^{-3}$, which yields the beta-decay branching ratio to the broad 1^- resonance to be $(1.3 \pm 0.3) \times 10^{-5}$. Note that we include in the estimate of the error the quoted error of the original measurement of the branching ratio of the 2.746 MeV gamma-rays ($\pm 20\%$) [Aj82]. In the above procedure, dead time correction or other effects associated with the beam-on and beam-off cycles were removed by taking the above ratio of alpha-particle and gamma-ray yields. In this way, the extracted branching ratio is solely dependent on the knowledge of the efficiencies and statistical accuracy of the data. The knowledge of the number of ^{16}N nuclei stopped in each detector as defined in Fig. 34, also allows for a measurement of this branching ratio and it yields a consistent results, with larger uncertainty.

The total number of alpha-particles in four Si detectors were summed, weighted

by the gamma-ray efficiency for the location of each Si detector. This sum was then compared to the number of gamma-decays recorded in Ge detector, and the relative branching ratio of alpha-particle decay to the gamma-ray decay was extracted. The source of the errors in this measurement is shown in table 1.

Table 1: Uncertainties in our measurement

Source	
statistical in E1	27%
statistical in E2	13%
statistical in E3	6.8%
statistical in E4	18%
error in Gamma peak	7.4%
Absolute γ eff. for E1	2.1%
Absolute γ eff. for E2	2.1%
Absolute γ eff. for E3	2.2%
Absolute γ eff. for E4	2.1%
weighted subtotal	17%
error in B.R.(2.74MeV)	20%
total	26%

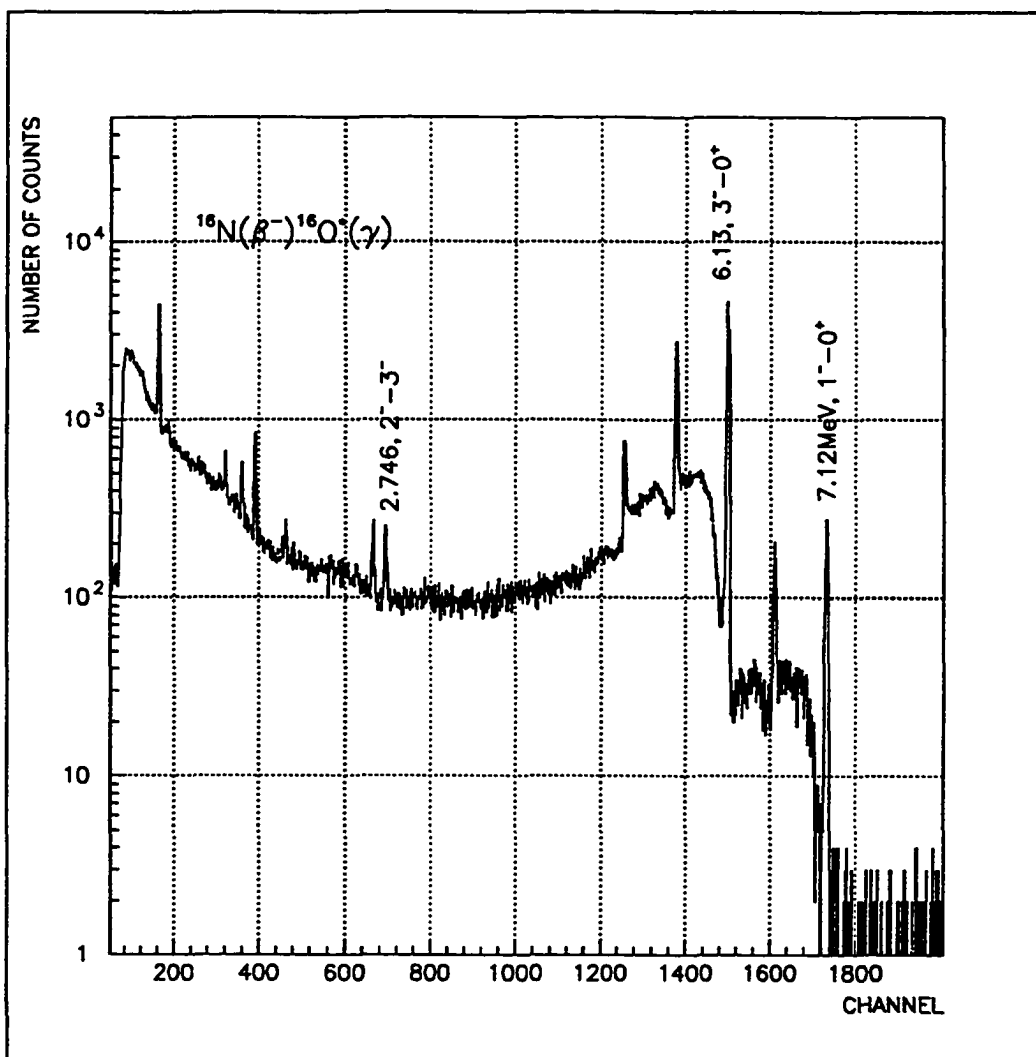


Figure 37: Beta-delayed gamma-rays from ^{16}N . Note the small intensity for the second escape peak, due to the large volume of the detector and the collimator. Scattering of gamma-rays from the collimator is noticeable around 6 MeV.

4 EXTRACTION OF THE ASTROPHYSICAL S-FACTOR

The spectrum of the beta-delayed alpha-particles discussed in the previous chapter (see Fig. 27) was unfolded, to remove effects of target thickness and energy resolution, and was fitted using the R-matrix formalism, discussed in chapter 2.

4.1 UNFOLDING OF THE DATA

The beta-delayed alpha-particle spectrum obtained at the Yale experiment exhibits an asymmetric line shape. This asymmetry is pronounced for thicker targets, and is attributed to the effect of target thickness. In Fig. 38, we show a comparison of our data with the data of reference [Ne74], measured with high statistics and high resolution (better than 30 keV), that we label as the 'zero' target thickness data. The effect of the finite energy resolution of our experiment is clearly observed in Fig. 38.

In the following, we discuss the procedure for unfolding our data and removing the effect of finite energy resolution (foil thickness). The measured spectrum of the beta-delayed alpha-particle $Y(E)$ arises from the convolution of the two functions X and G :

$$Y(E) = \int_{-\infty}^{\infty} X(E')G(E, E - E')dE' \quad (21)$$

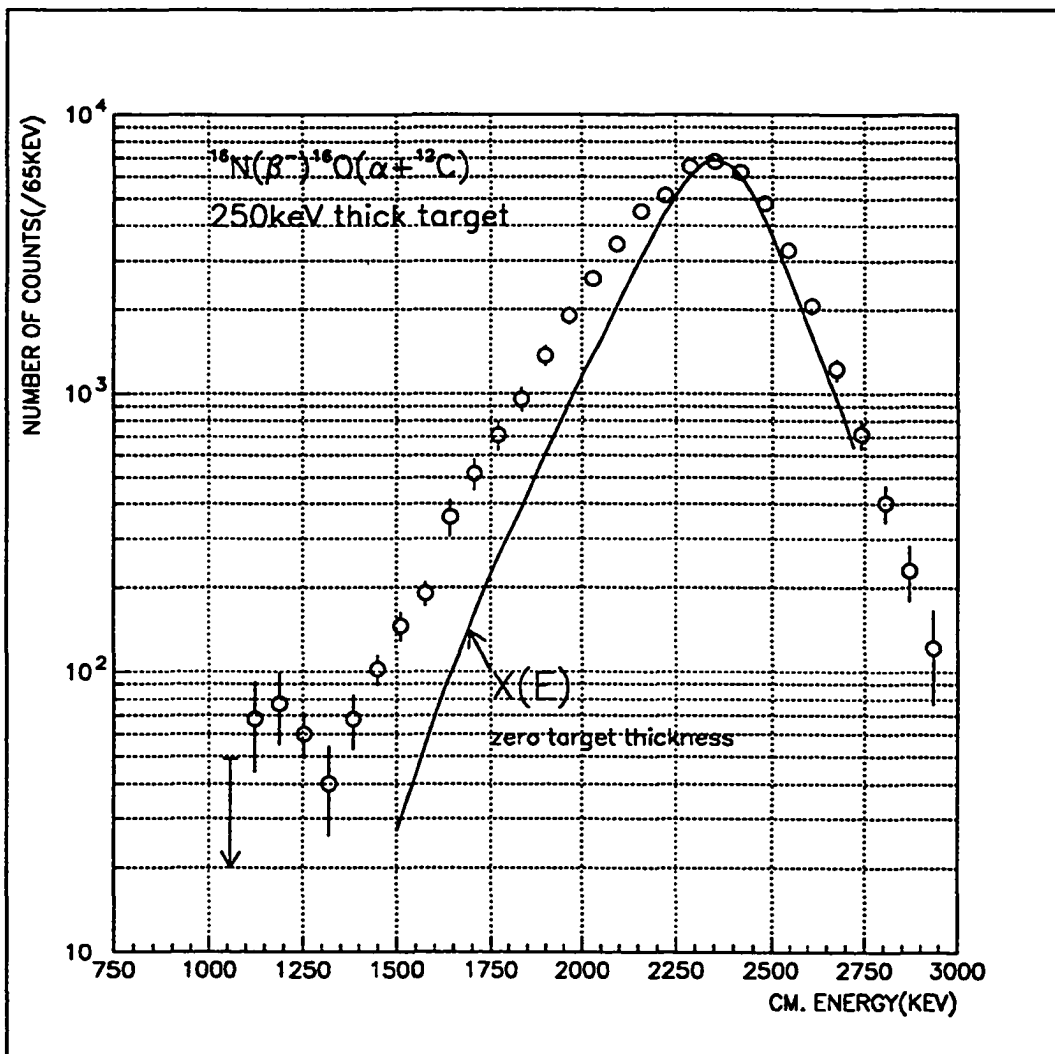


Figure 38: The experimental data compared with 'zero' target thickness data [Ne74].

where $X(E)$ is the 'true' signal ('zero' target thickness signal), and $G(E,E')$ is the response function of the system. For a given response function $G(E,E')$, one needs to solve this integral equation in order to obtain $X(E)$. Note the shape of $X(E)$ is predicted by all three theories [Ji90,Hu91,Ba88] to have a low energy structure whose width is larger than the experimental resolution. We obtained $X(E)$ by construction, using the 'trial and error' method. In this method, we convoluted 'zero target thickness' data with the response function and compare it with experimental data.

The response function of the system can be written as:

$$G(E, E - E') = H(E, E - E')R(E) \quad (22)$$

where $H(E,E-E')$ is a square function convoluted with the gaussian energy response of the Si detectors, as shown in Fig. 39 (with $\int_{-\infty}^{\infty} H(E, E - E')dE' = 1$). Note that the width of the square function is energy dependent. The convolution of the 'zero' target thickness data and the response function with $R(E)\equiv 1$, is shown in Fig. 40 by the smooth curve labeled Y_0 . This convolution reproduces our data at higher energies, but it misses our data at low energies. In Fig. 41, we plot dY/Y , where Y is our measured experimental data and $dY=Y-Y_0$. Note that our data, given by $Y=Y_0/(1-dY/Y)$, is larger than Y_0 . This is mainly due to the fact that our ^{16}N recoiling nuclei are not distributed uniformly throughout the target. A non-uniformity of the order of 10-15%, accounts for the fact that our experimental

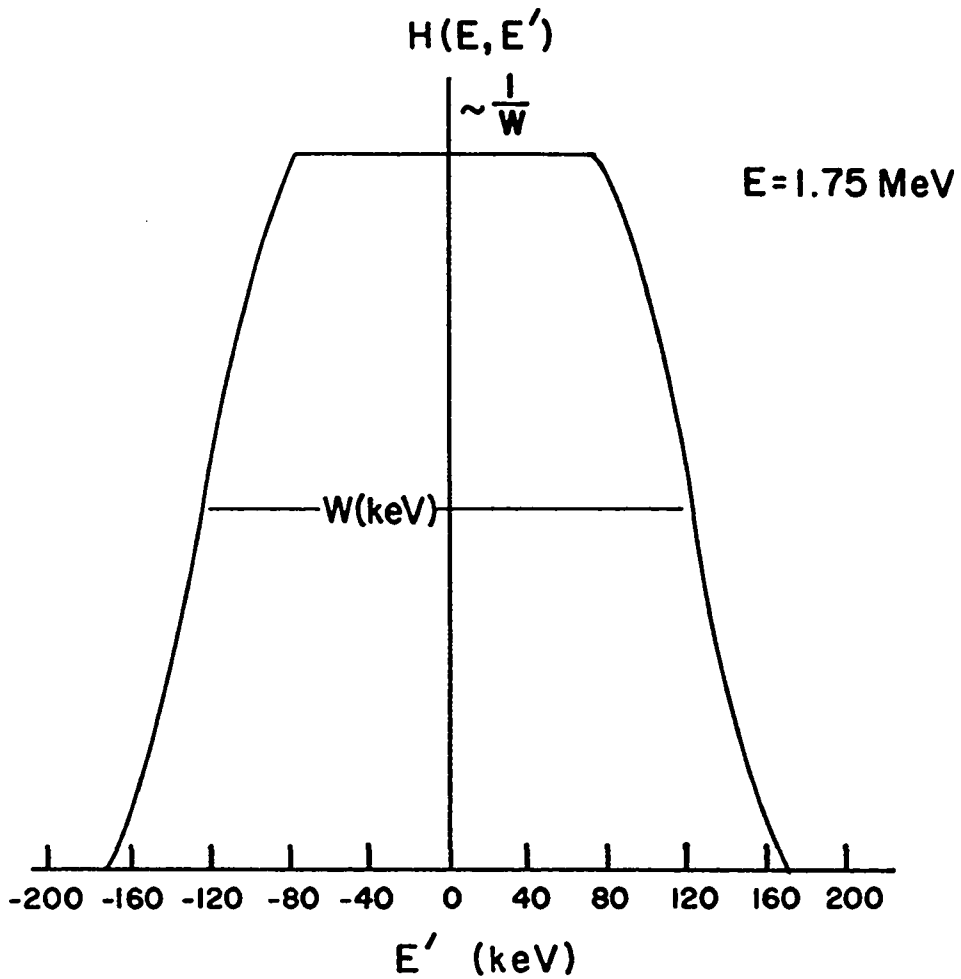


Figure 39: The response function of the system at $E=1.75$ MeV. Note that the width is energy dependent.

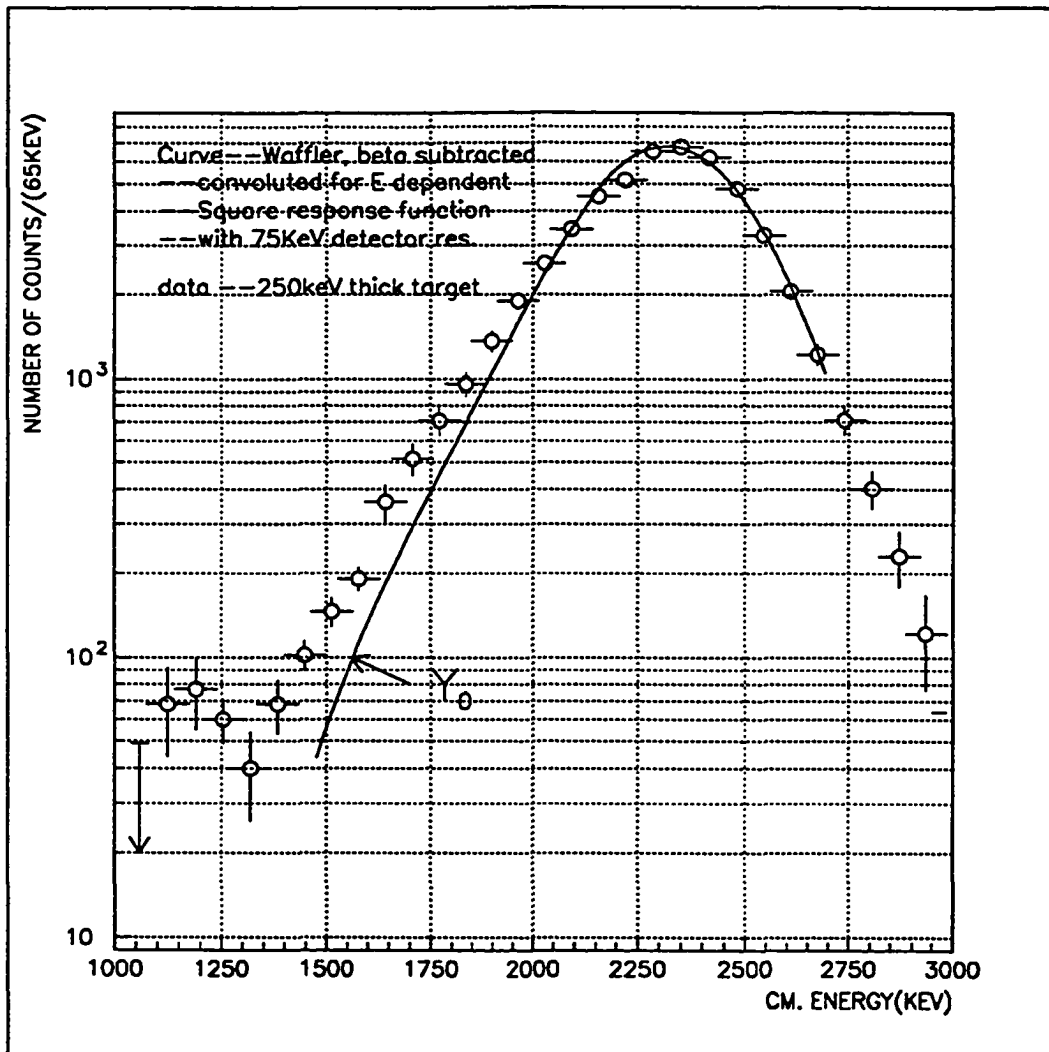


Figure 40: Convolution of 'zero' target thickness data with square response function ($R(E) \equiv 1$) as compared with obtained data.

data does not arise from a mere integration of the 'zero' target thickness data. Consequently, we constructed the response function of our system with:

$$R(E) = [1 - \frac{dY}{Y}(E)]^{-1} \quad (23)$$

The function $R(E)$ is determined empirically, and since the 'zero' target thickness data is very well defined down to 1.5 MeV, the function $R(E)$ is also well defined down to 1.5 MeV. Consequently, the unfolding procedure carries small uncertainty down to 1.5 MeV and we need to further extrapolate it down to 1.1 MeV. Since $R(E)$ reflects a tail from higher energies, the extrapolation is such that $R(E)$ below 1.45 MeV is a constant at a value of 3.6. As we discuss below the unfolding of our data yields the largest source of systematic uncertainties of our results. We, however, emphasize that the extrapolation from 1.4 MeV down to 1.1 MeV does not pose any great difficulty for our unfolding procedure. In Fig. 43, we show the convolution of the theoretical curve corresponding to $S_{E1}=95$ keV-barn with the response function., together with the experimental data.

The unfolded data (with effects of finite energy resolution removed) is shown in Fig. 44. The error bars on the data points are statistical only. While the height of the secondary maximum at low energy, is very well defined by the unfolding procedure (within $\pm 20\%$), the exact position and the value of the one data point at the minimum carries a sizable systematic error. The yield at the minimum arises mainly due to the integration interval, hence the yield for the unfolded

(‘true’) minimum can in fact be smaller (even zero), but not larger than the one shown in Fig. 44.

In Fig. 45 we show the ratio of the yield of the lower energy secondary maximum to the yield of the broad 1^- resonance, as a function of the foil thickness for the three sets of data obtained . This ratio varies with the foil thickness, and we extract the ratio corresponding to zero target thickness to be approximately 0.0025 ± 0.0037 . While this ratio is deduced from Fig. 45 with a large uncertainty, it is consistent with the value of 0.0023 obtained for the unfolded data, see Fig. 44.

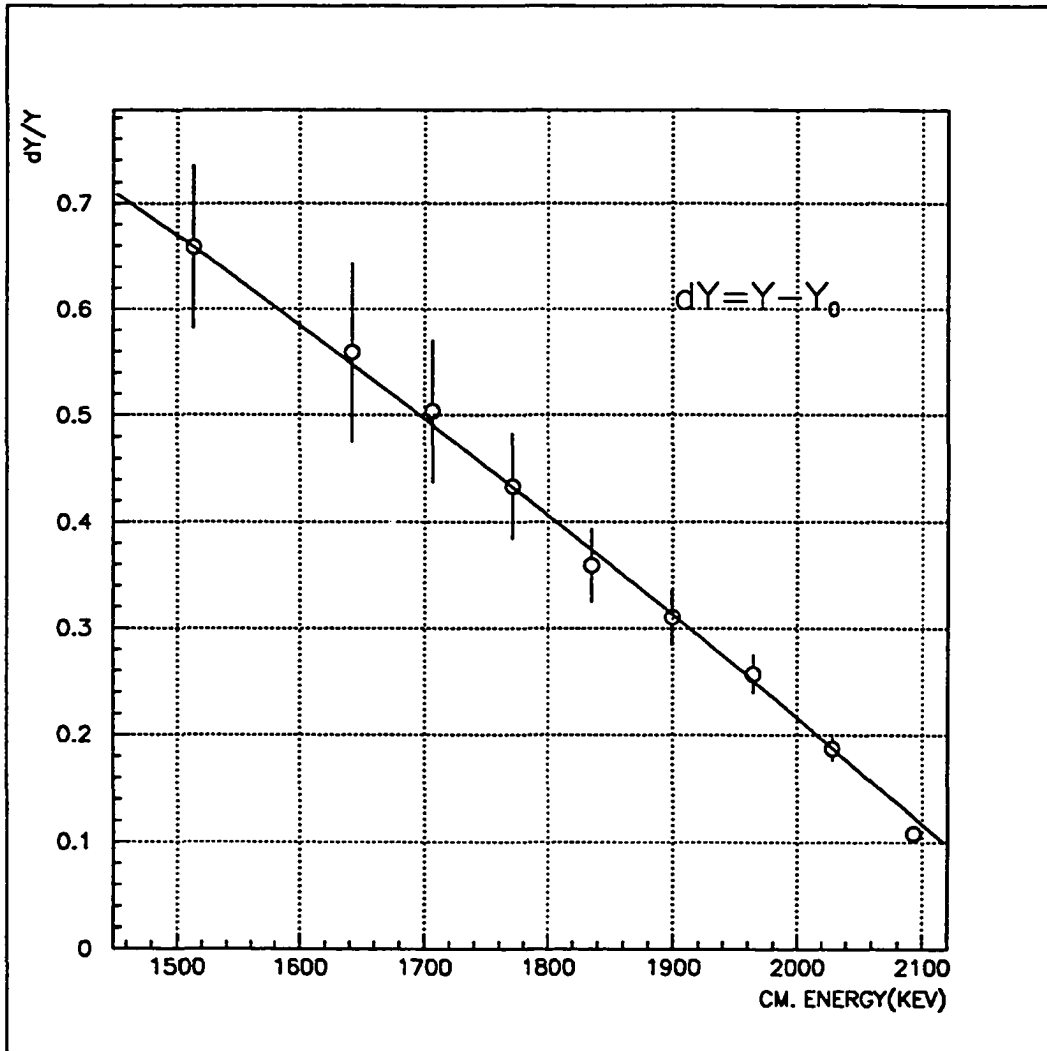


Figure 41: dY/Y as a function of energy as discussed in the text.

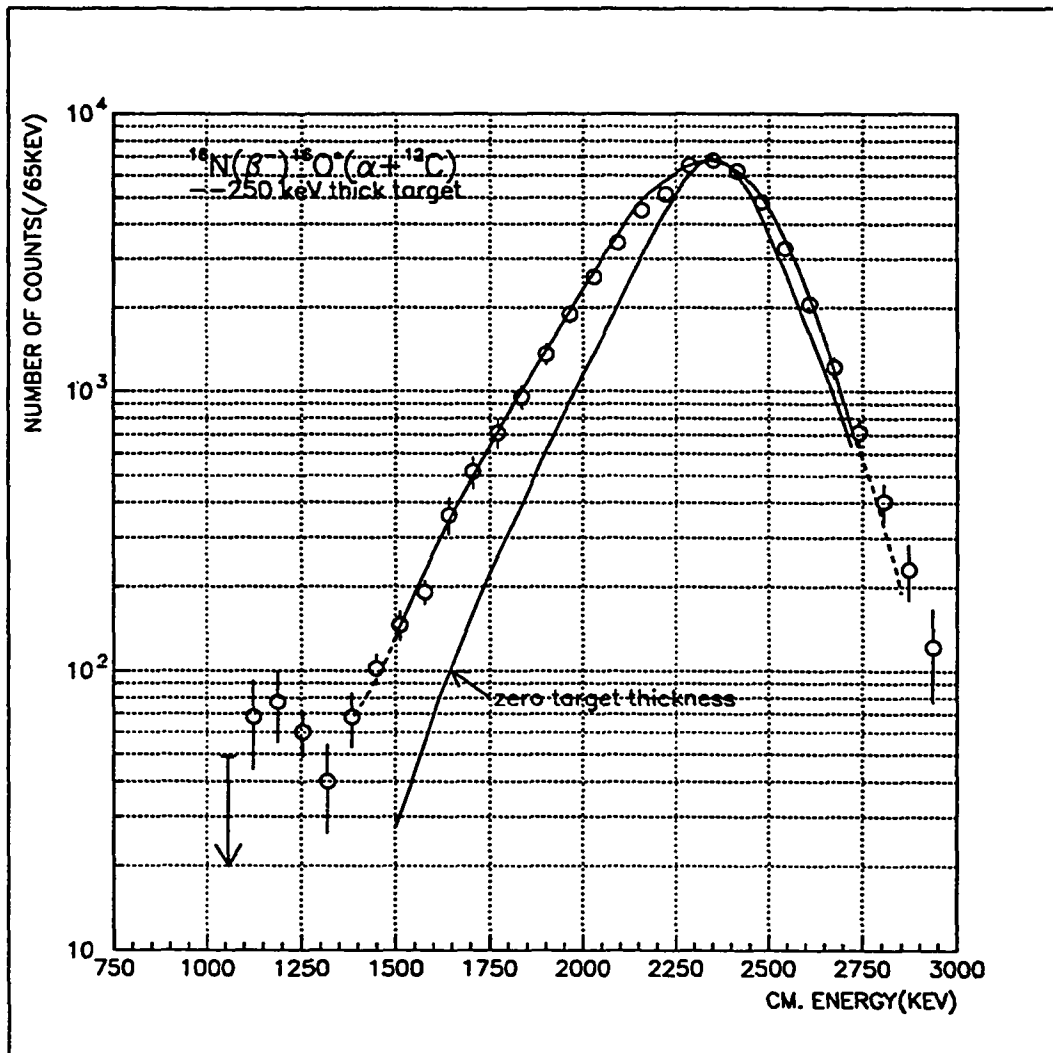


Figure 42: Convolution of 'zero' target thickness data [Ne74] with the response function of our setup as compared to measured data.

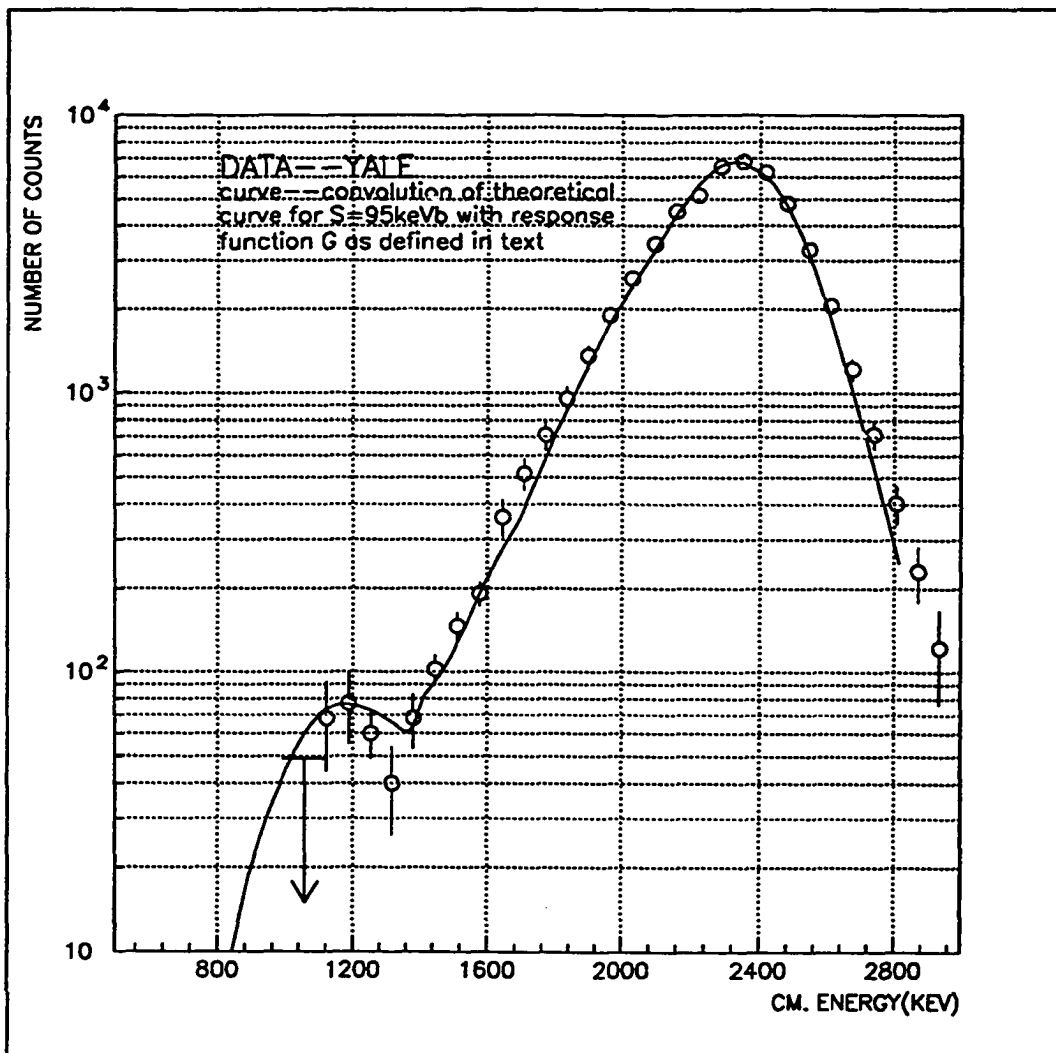


Figure 43: Convolution of theoretical alpha-particle spectrum corresponding to $S_{E1}(300)=95\text{ keV-barn}$ as in Fig.46 with the response function, is plotted together with the experimental data.

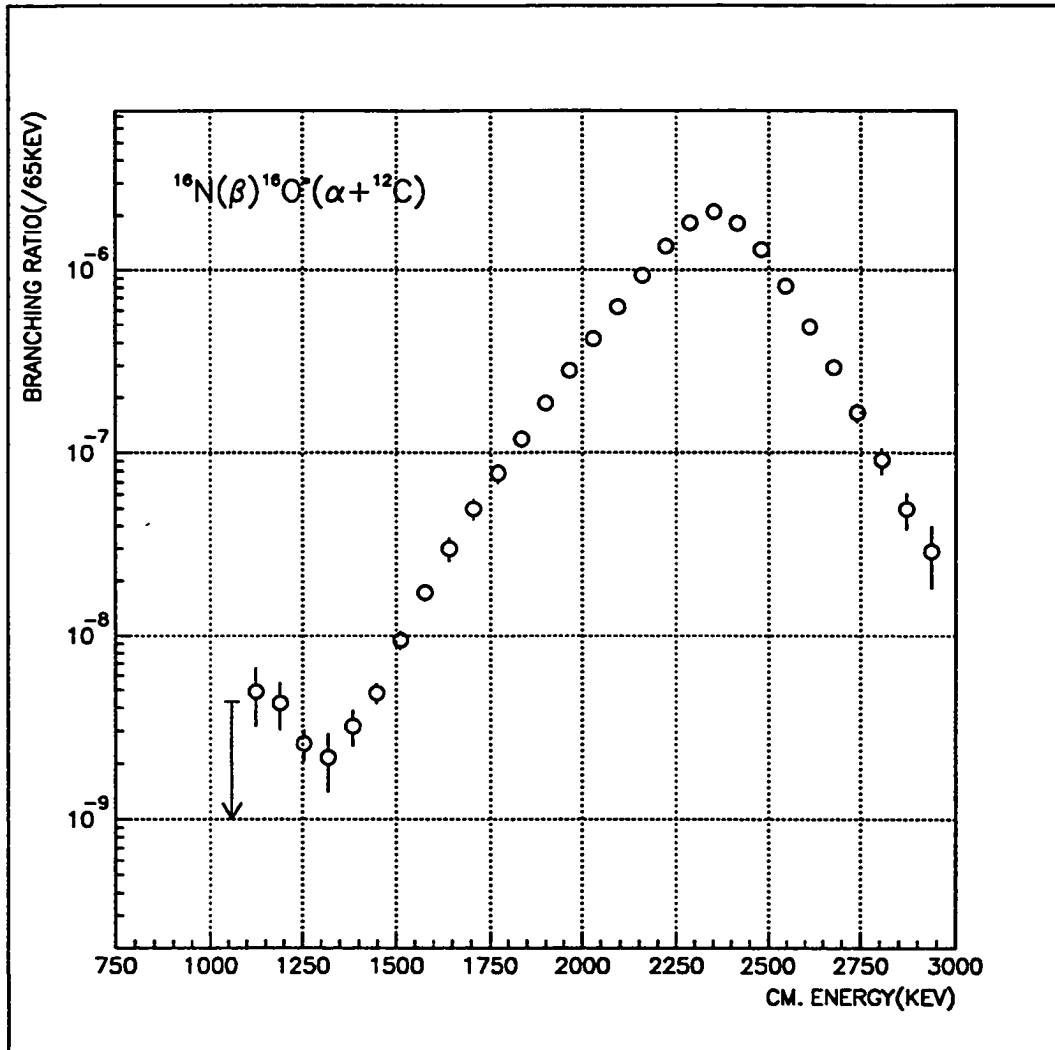


Figure 44: Unfolded spectrum of the beta-delayed alpha-particles from ^{16}N .

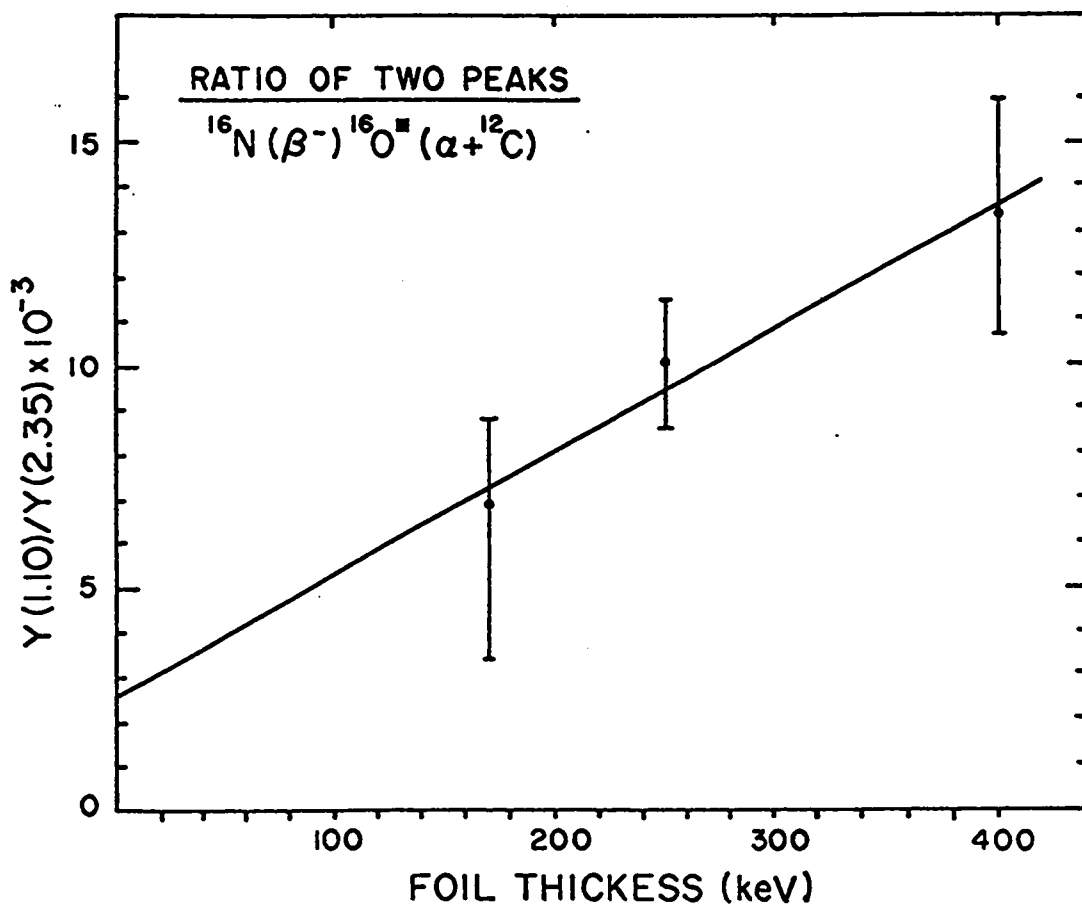


Figure 45: Ratio of the secondary maximum to the peak of the broad resonance, as a function of foil thickness.

4.2 R-MATRIX ANALYSIS

The simultaneous R-matrix theory analysis to our unfolded data (Fig. 44), the previously published data on the $^{12}\text{C}(\alpha, \gamma)^{16}\text{O}$ reaction cross section [Dy74], and the phase shifts of alpha-particles elastic scattering from ^{12}C [Jo62, Cl68, Pl87], was performed using the code developed by Ji et al. [Ji90]. We used the same model parameter space used by Ji et al., including the channel radius $a=5.5$ fm, the beta-decay strength for the background state $A_3 = -6,000 \text{ MeV}^{1/2}$, and the boundary condition parameter $B = -3.504$, used in reference [Ji90]. These parameters were shown to yield the best fit to all previously existing data [Ji90]. As we discussed in chapter 2, we do not intend to carry in this work an in depth study of the model parameter space, including the dependence of the results on the channel radius. We view the theoretical analysis presented in this chapter as preliminary and we refer the reader to [Ba91] for an in depth theoretical discussion of the model parameter space (including the channel radius) and to [Ji90] for an in depth discussion of the detailed fitting procedure. We hope that our results will further promote such detailed theoretical studies of the model parameter space, and at the end of this chapter we present a preliminary study of the dependence of the extracted $S_{E1}(300)$ on the beta-decay strength of the background state (the parameter A_3).

Ji et al. [Ji90] carried out the simultaneous R-matrix fit of the data as discussed in chapter 2, including the data on the beta-delayed alpha-particle emission of ^{16}N [Ne74]. As we discussed earlier, Ji et al. used data on the beta-delayed alpha-

particle emission of ^{16}N that did not extend to low energies [Ne74], but their analysis could be used to fix most of the parameter space of the model, except $S_{E1}(300)$. As we discussed in Ch.2, the three levels used in their R-matrix fit are the sub-threshold 1^- state at 7.12 MeV, the unbound 1^- state at 9.6 MeV and a background level representing contributions from high lying 1^- states. The nine parameters involved in the fit are: $S_{E1}(300)$, the reduced alpha-particle width of the unbound and background states ($\gamma_{2\alpha}$ and $\gamma_{3\alpha}$), the gamma width of the unbound and background states ($\gamma_{2\gamma}$ and $\gamma_{3\gamma}$), the energy of the unbound and background states (E_2 and E_3), and the beta-decay strength for the unbound and background states (A_2 and A_3).

Using the best-fit parameters (including $A_3 = -6,000 \text{ MeV}^{1/2}$) of Ji et al., we performed an R-matrix fit, in search of the parameter $S_{E1}(300)$ that produces the best fit for our data. In Fig. 46 we show the unfolded data together with the R-matrix fit, where the solid curve corresponds to the choice of $S_{E1}(300) = 95 \text{ keV-barn}$. Only with the addition of an $l = 3$ component, was it possible to reproduce the line shape of the unfolded data in the vicinity of the minimum at 1.4 MeV. We emphasize here that the choice of $l = 3$ contribution does not have much of the theoretical basis, it was introduced to reproduce the shape of the beta-delayed alpha-particle emission spectrum. Although the experimental data at the low energy secondary maximum were measured with approximately 25% statistical uncertainty (with a 15% statistical uncertainty in the extracted ratio of two maximum), the uncertainty in the extracted value of S_{E1} is only approximately 7%. This large sensitivity is expected for an interference effect. In

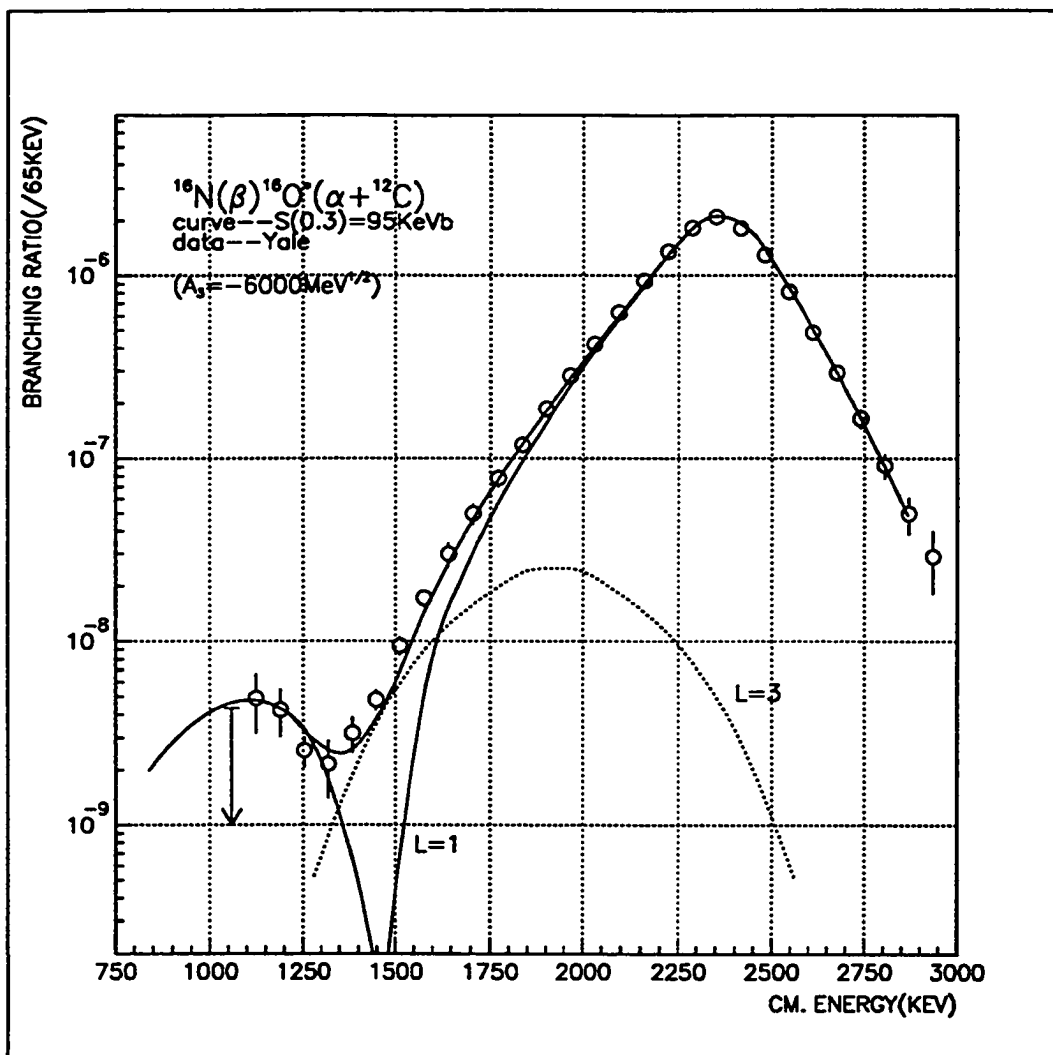


Figure 46: R-matrix fit to the unfolded data.

Fig. 47, we show the best-fit parameter calculations for the value of $S_{E1}(300)=95$ keV-barn, and for the extreme values (dashed lines) of ± 6 keV-barn allowed by the statistics. Note that we do not apply a χ^2 test, since the χ^2 is mainly determined by the data at higher energies, which is measured with high statistics but not sensitive to the value of the S-factor.

One of the major contribution to the systematical uncertainty of our results arises from the unfolding of our data to the 'zero' target thickness. As we demonstrated earlier, the unfolding of the data carries little uncertainty down to 1.4 MeV. We carried out a series of calculations to study the dependence of the yield at the secondary maximum, on the value of $S_{E1}(300)$. In Fig. 48, we show the results of these calculations for several values of $S_{E1}(300)$. Note the position of the minimum change as $S_{E1}(300)$ change. In these calculations all parameters were kept at their best fit value [Ji90] and only $S_{E1}(300)$ was varied, unlike the work of Ji et al. where A_3 is also varied (see Fig. 6).

In Fig. 49, we show the dependence of the extracted S-factor on the choice of the response function $R(E)$. Note that since the function $H(E,E')$ is very well defined, the uncertainty in the unfolding procedure mainly arise from the uncertainties in $R(E)$. The different choices for $R(E)$ produce an secondary maximum of different height. As can be seen from Fig. 48, an uncertainty in $R(E)$ translates directly to an uncertainty in $S_{E1}(300)$. The curve shown in Fig. 49 however, indicates that an uncertainty of $\pm 30\%$ in $S_{E1}(300)$ requires variation of $R(E)$ by a factor of 2 or 3 or more. Our detailed study of the unfolding procedure and the response

function, leads us to conclude that $R(E)$ is well understood to better than a factor of 2 and certainly better than a factor of 3. This conclusion is also supported by the data of Fig. 44. We conclude that the uncertainty in the unfolding procedure can not lead to an uncertainty in $S_{E_1}(300)$ larger than 20%, and we quote the conservative systematic uncertainty of $\pm 30\%$.

Another contribution to the systematical uncertainty of the extraction of the value of $S_{E_1}(300)$ may arise from the uncertainty due to the magnitude of the f wave ($l = 3$) component. Preliminary theoretical estimates [Ji92] indicates that although the f-wave contribution in the vicinity of the minimum is significant, the contribution to the secondary maximum is not larger than 25% of the observed yield at 1.1 MeV. Such a contribution from an $l = 3$ component reduces the value of the best fit $S_{E_1}(300)$ from 95 keV-barn to 89 keV-barn. This uncertainty ($\pm 7\%$) is significantly smaller than the systematical uncertainty due to the unfolding of our data ($\pm 30\%$). If we take a more conservative approach and assume the $l = 3$ contribution at 1.1 MeV is equal to that at 1.4 MeV (unlike shown in Fig. 46), we deduce an S-factor which is only 15% smaller. We conclude that the uncertainty due to the contribution of the $l = 3$ component is significantly smaller than the 30% uncertainty that we quote as our systematic uncertainty. We therefore quote $S_{E_1}(300) = 95 \pm 6(\text{stat}) \pm 28(\text{syst})$ keV-barn.

We emphasize that the predicted height of the secondary maximum, is very sensitive to the value of $S_{E_1}(300)$ if and only if the beta-decay strength of the background state (the parameter A_3 , see eq. 16) is fixed. While in this thesis we do not

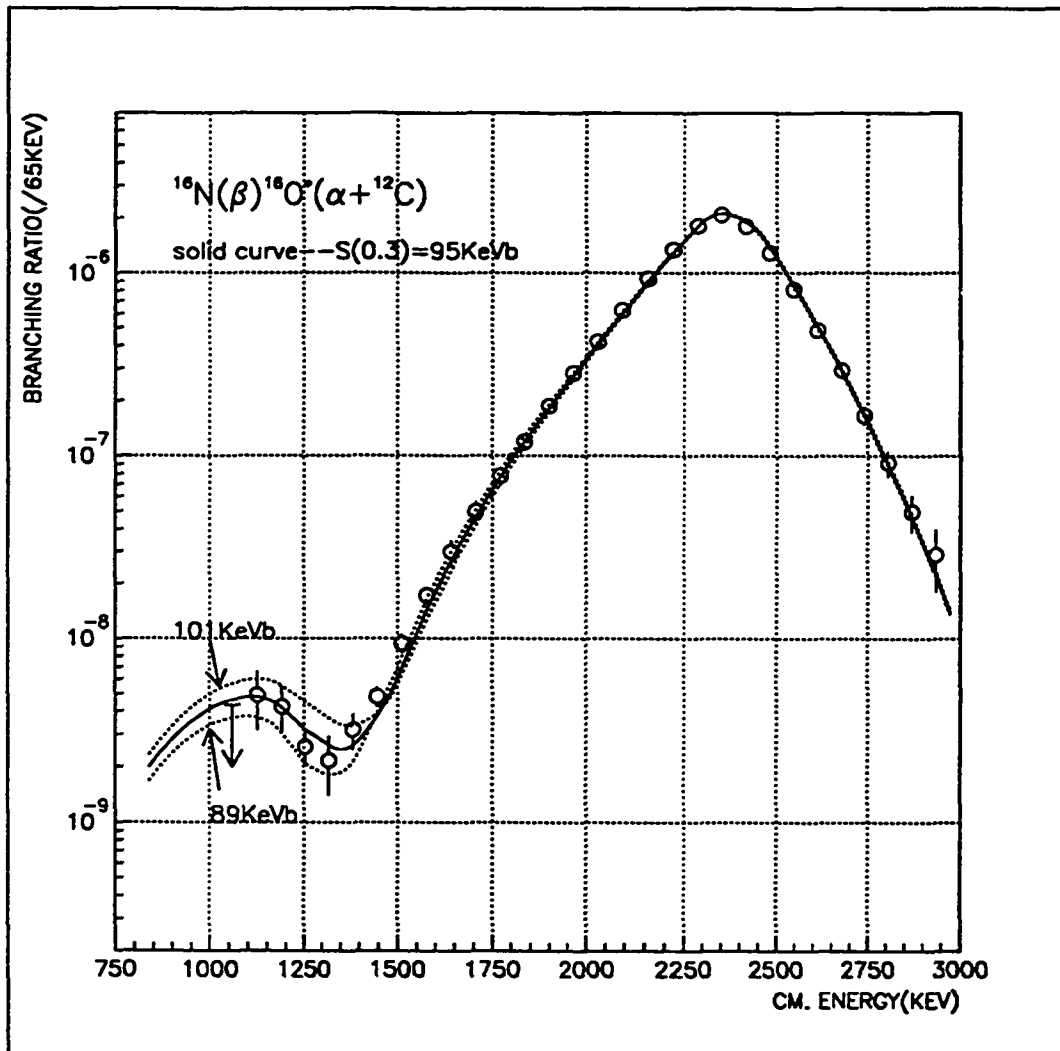


Figure 47: The R-matrix fit to the data with best fit, solid line ($S_{E1}(300)=95$ keV-barn), and dash lines correspond to $S_{E1}(300)=101$ keV-barn and 89 keV-barn, as indicated.

intend to investigate in depth the dependence of the extracted $S_{E_1}(300)$ on the model parameter space, we have carried out a preliminary study of the dependence of the theoretical predictions on variation in the parameter A_3 . We calculated the beta-delayed alpha-particle spectrum using the best-fit parameters obtained by Ji et al. and for $A_3 = -2000, -6000, \text{ and } -10000 \text{ MeV}^{1/2}$. In Fig. 50, we show the theoretical calculation of the ratio of the yield at the broad 1^- resonance to the secondary maximum, as a function of the value of $S_{E_1}(300)$, for two extreme values of A_3 . The area enclosed by the two horizontal lines represents an error of approximately $\pm 15\%$ in determining the height of the secondary maximum. Note that as demonstrated above, the statistical uncertainty in the height of the extracted secondary maximum is of the order of $\pm 15\%$. For this uncertainty (indicated by the two horizontal lines in Fig. 50), we extract an uncertainty in $S_{E_1}(300)$ of -28% and $+36\%$, as indicated by the two vertical lines. We conclude that the uncertainty in the extracted $S_{E_1}(300)$, due to very large variations in the value of the parameter A_3 (by approximately $\pm 67\%$) leads to an uncertainty in the extracted value of $S_{E_1}(300)$ which is comparable or smaller than our quoted systematical uncertainty. It is however clear from this preliminary analysis, that an in depth theoretical analysis is required in order to fully understand the exact dependence of the extracted $S_{E_1}(300)$ on the value of all the parameters used in the R-matrix theory fit. We hope that our data will promote such detailed theoretical analyses.

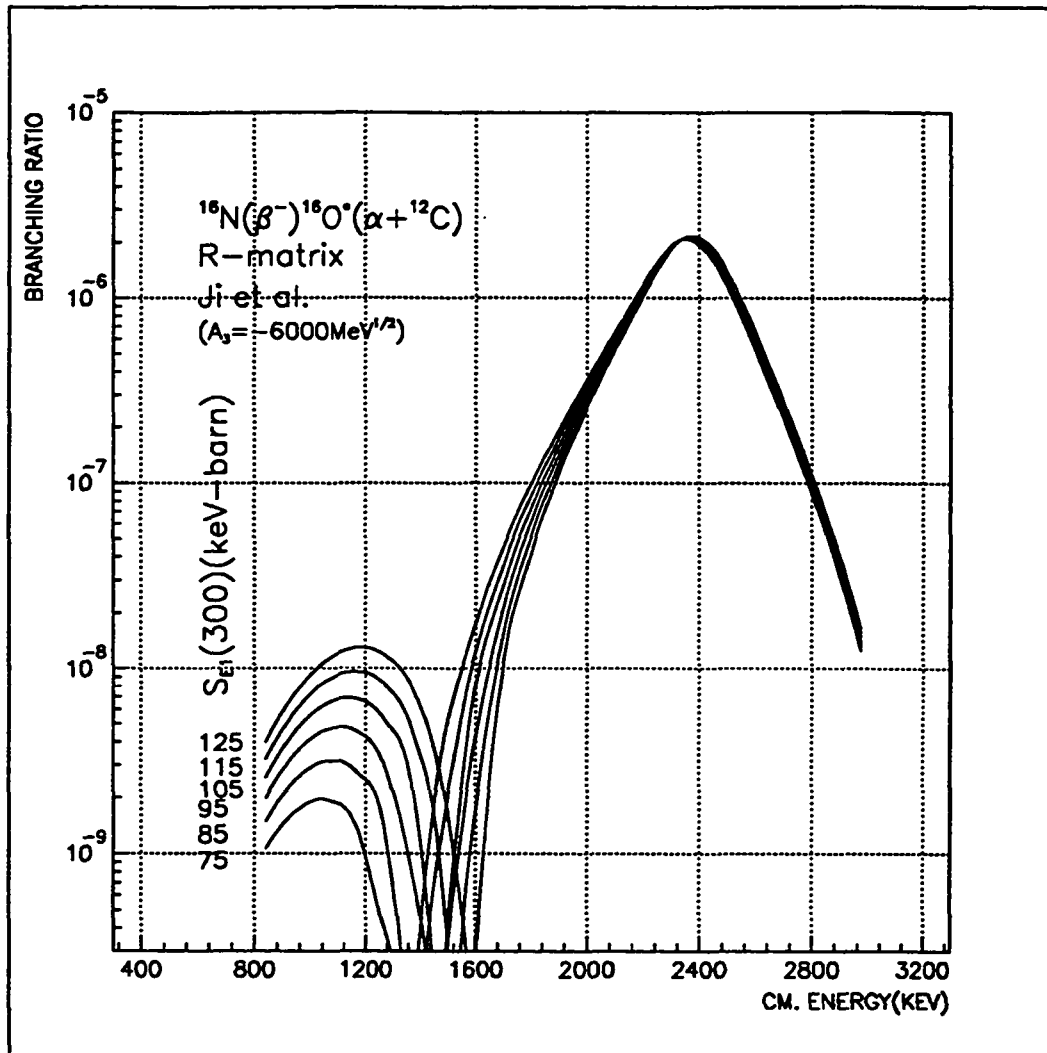


Figure 48: The yield at the secondary maximum for various values of $S_{E1}(300)$. All other parameters are fixed at their best fit value derived by Ji et al. [Ji90]. The large variation in the yield for the secondary maximum are obtained since A_3 is fixed in these calculations.

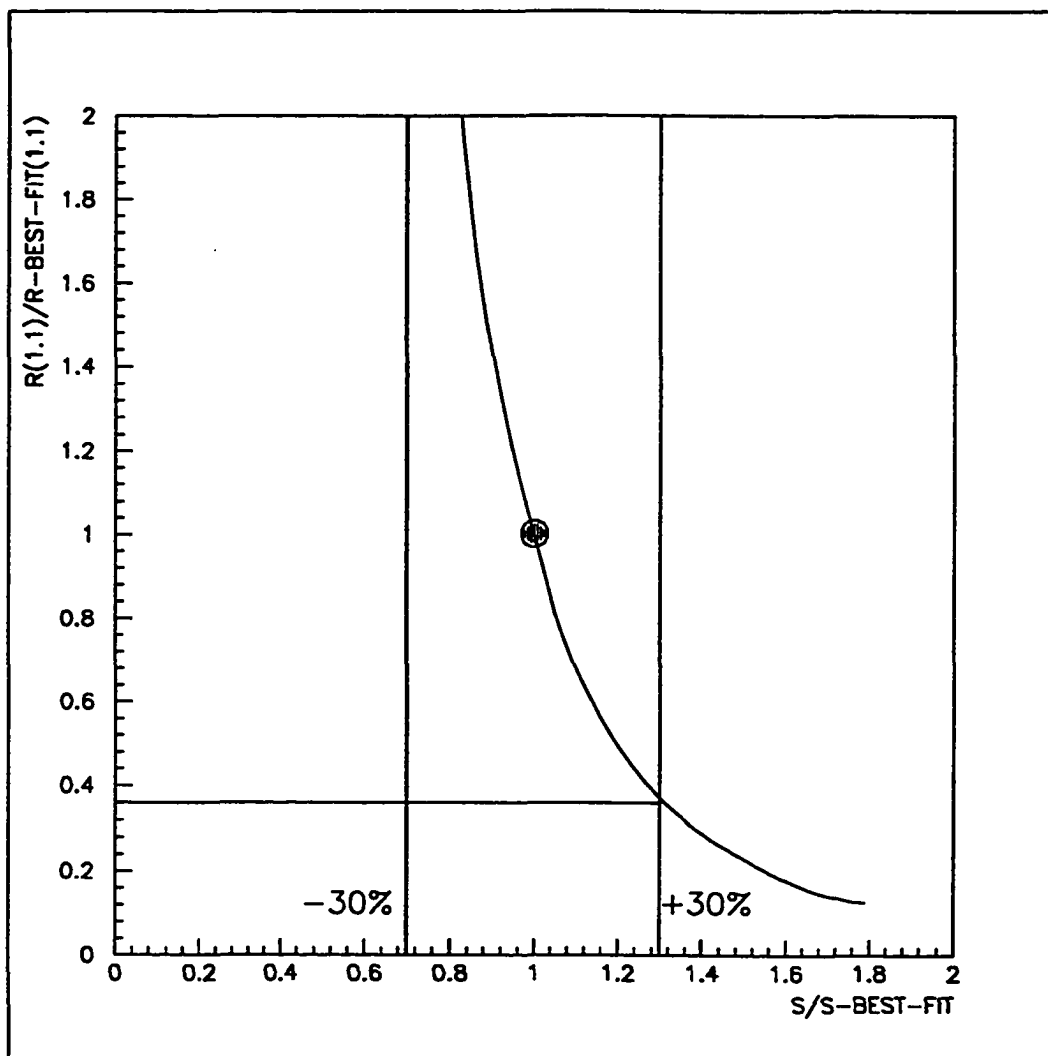


Figure 49: The dependence of the extracted S-factor on the values of the response function $R(E)$ at the secondary maximum ($E_{CM} = 1.1$ MeV). The best fit value $S_{E1} = 95$ keV-barn with its lower and upper bounds ($\pm 30\%$) are shown.

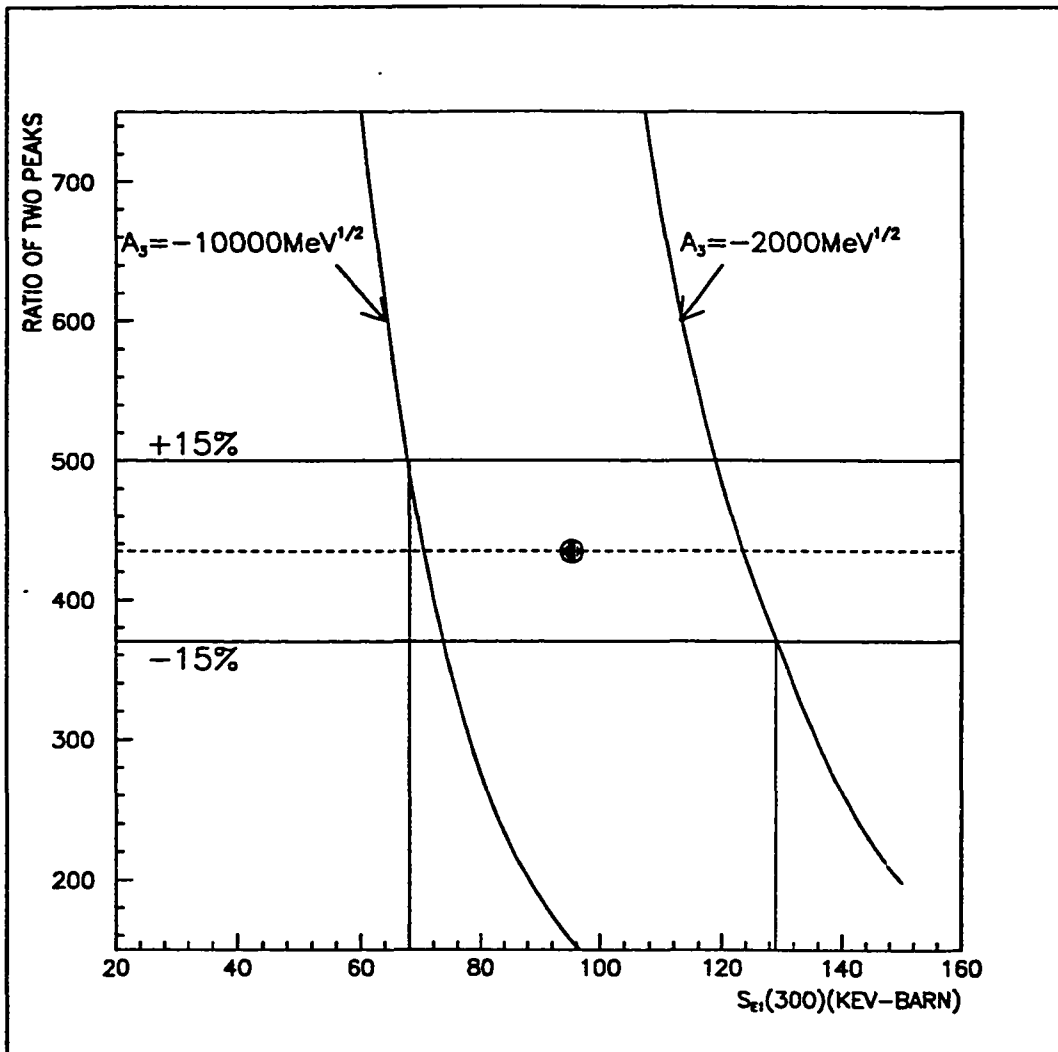


Figure 50: The ratio of the yield for the unbound 1^- resonance to the yield of the secondary maximum, as a function of $S_{E1}(300)$. The two curves corresponds to $A_3 = -2,000$ and $-10,000 MeV^{1/2}$, respectively.

5 CONCLUSIONS

Some of the previously extrapolated $S_{E1}(300)$ values for the $^{12}\text{C}(\alpha, \gamma)^{16}\text{O}$ capture reaction and the results of this work, are shown in table 2, and plotted in Fig. 51.

Table 2: Values of $S_{E1}(300)$ obtained by various experiments.

Analyses	Author	$S_{E1}(300)(keV - barn)$
R-matrix	Dyer and Barnes ^a	140_{-120}^{+140}
	Barker ^b	140_{-50}^{+130}
	Ouellet et al. ^c	1_{-1}^{+6}
	Kremer et al. ^d	0-140
	Kettner et al. ^e	420_{-120}^{+160}
	Redder et al. ^f	200_{-110}^{+270}
K-matrix	Humblet et al. ^g	80_{-70}^{+140}
	Humblet et al. ^h	43_{-16}^{+24}
	Buchmann et al. ⁱ	57 ± 13
Hybrid R-matrix	Koonin et al. ^j	80_{-40}^{+50}
R-matrix	Present work.	95_{-29}^{+29}

- a) $^{12}\text{C}(\alpha, \gamma)^{16}\text{O}$ measurement, from [Dy74].
- b) Reanalysis of experimental data, from [Ba87].
- c) $^{12}\text{C}(\alpha, \gamma)^{16}\text{O}$ measurement, from [Ou92].
- d) $^{12}\text{C}(\alpha, \gamma)^{16}\text{O}$ measurement, from [Kr88].
- e) $^{12}\text{C}(\alpha, \gamma)^{16}\text{O}$ measurement, from [Ke82]. quoted number is for total S factor.
- f) $^{12}\text{C}(\alpha, \gamma)^{16}\text{O}$ measurement, from [Re87].
- g) Reanalysis of experimental data, from [Hu76].
- h) Reanalysis of experimental data, from [Hu91].
- i) Beta-delayed alpha-particle emission measurement, from [Bu92].
- j) Reanalysis of experimental data, from [Ko74].

The result from a similar experiment performed by Buchmann et al. [Bu92] on the

beta-delayed alpha-particle emission of ^{16}N is also included in the table. Buchmann et al. used a low energy ^{16}N beam with the TRIUMF isotope separator TISOL. Therefore the experimental design by Buchmann et al. is very different, so is the sources of systematic errors. The experimental result by Buchmann et al. agrees with our result within the errors.

We conclude that by using spectra of the beta-delayed alpha-particle emission of ^{16}N , we are able to determine the E1 S-factor for the $^{12}\text{C}(\alpha, \gamma)^{16}\text{O}$ reaction at 300 keV. We have studied uncertainties in our quoted value due to: statistics, $l = 3$ components, and the procedures for unfolding the data to yield the 'zero' target thickness data. We quote $S_{E1}(300) = 95 \pm 6(\text{stat}) \pm 28(\text{syst})$ keV-barn.

We have demonstrated that an uncertainty similar or smaller than our systematic uncertainty, could arise from variations in the model parameter space of the R-matrix theory. The shape and the magnitude of the $l = 3$ component is still an open question, and needs to be investigated. The effects of other R-matrix parameters, such as channel radius(a) and the boundary condition constant(B), also needs to be investigated by theorists. We hope our work will promote further theoretical studies of the model parameter space and the theoretical uncertainties involved in extracting $S_{E1}(300)$, from data on the beta-delayed alpha-particle emission of ^{16}N .

The largest uncertainty in our quoted $S_{E1}(300)$ lies in the systematic uncertainty due to the finite thickness of our catcher foil. The importance of measuring this S factor warrants further studies of the beta-delayed alpha-decays from ^{16}N ,

with an improved design to reduce the systematic errors ($\pm 30\%$) of the current measurement.

As we discussed in Ch.1, the last stages in the evolution of a massive star depends critically on the the S-factor for $^{12}\text{C}(\alpha, \gamma)^{16}\text{O}$ reaction at 300 keV. The adopted value of $S_{E_1}(300)$ by Caughlan and Fowler is 60_{-30}^{+60} keV-barn [Ca88]. Weaver and Woosley have performed calculations for a broad mass range of presupernova models over a range of experimentally allowed $^{12}\text{C}(\alpha, \gamma)^{16}\text{O}$ reaction rates. They achieved an excellent agreement between the calculated abundances of all the intermediate mass isotopes ($16 \leq A \leq 32$) and their solar values, if and only if the $^{12}\text{C}(\alpha, \gamma)^{16}\text{O}$ reaction rate is 1.7 ± 0.5 times the adopted value in [Ca88]. Note that our value of $S_{E_1}(300) = 95 \pm 6 \pm 28$ keV-barn is very close to the $S_{E_1}(300) = 102 \pm 31$ keV-barn deduced by Weaver and Woosley from stellar model calculations.

We conclude that the two different laboratory measurements: the one presented here and the one performed at TRIUMF [Bu92], together with an extraction from stellar models, for the first time give a consistent value for $S_{E_1}(300)$. This then allows stellar models to describe the collapse of massive stars without introducing a free parameter for the cross section of $^{12}\text{C}(\alpha, \gamma)^{16}\text{O}$ reaction. The value of $S_{E_1}(300)$ obtained in this work is consistent with the accepted value of the p-wave S-factor, but slightly larger [Ca88]. This implies that massive stars most likely do not skip the carbon and neon burning before supernova explosion [We92] and proceed as show in Fig.1.

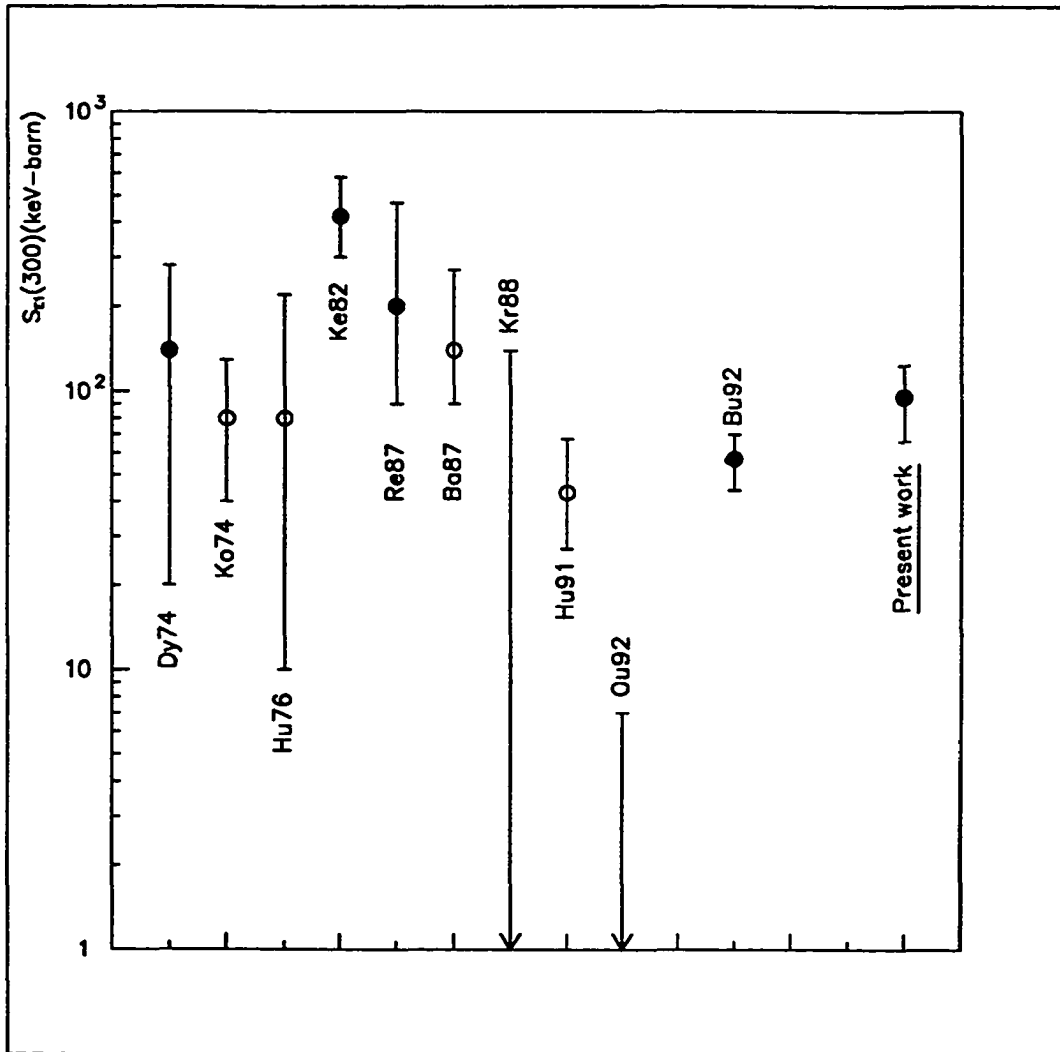


Figure 51: Some of extrapolated values of $S_{E1}(300)$ obtained. The filled circles and upper limits are the extrapolation performed by the experimental groups, the open circles are the reanalysis of the experimental data.

APPENDIX A

In Table 3 we list the experimental data for beta delayed alpha emission from ^{16}N for the 250 keV thick target, corrected for energy dependent target thickness and beta detector efficiency. In Table 4 we list the data for the 170 keV thick target, and in table 5 we list the data for the 400 keV thick target.

Table 3: Experimental data of alpha spectra for the 250 keV thick target, corrected for target thickness and TOF efficiency. The uncertainty of the measured energy is 40 keV.

CM.Energy(keV)	Counts(/65keV)	Error
1058	≤49	
1124	68	24
1189	77	22
1254	60	11
1319	40	14
1384	68	15
1448	102	12.5
1513	146	17
1577	191	18.5
1642	360	54
1706	516	68
1771	707	81
1835	956	92
1900	1359	122
1964	1895	130
2029	2582	149
2093	3442	172
2158	4507	195
2222	5149	202
2287	6522	240
2352	6790	244
2416	6227	232
2481	4807	216
2546	3271	168
2611	2058	131
2676	1219	104
2740	714	81
2805	404	62
2870	231	52
2935	122	45
3001	64	34
3066	27	17

Table 4: Experimental data of alpha spectra for the 170 keV thick target, corrected for target thickness and TOF efficiency. The uncertainty in measured energy is 25 keV.

CM.Energy(keV)	Counts(/157keV)	Error
1004	≤40	
1169	33	19
1333	≤9	
1484	83	12
1641	222	19
1797	380	25
1955	982	38
2111	2289	56
2268	4214	82
2424	4355	88
2581	2225	69
2739	683	43
2896	166	27
3053	53	15

Table 5: Experimental data of alpha spectra for the 400 keV thick target, corrected for target thickness and TOF efficiency. The uncertainty in measured energy is 60 keV.

CM.Energy(keV)	counts(/105keV)	Error
883	≤ 4	
990	≤ 4	
1093	3	4
1200	10	5
1304	≤ 4	
1487	17	3
1616	29	6
1720	49	7
1827	115	13
1929	190	15
2033	313	18
2136	487	28
2240	650	32
2347	715	41
2449	591	34
2553	350	19
2660	170	20
2764	70	11
2867	29	6
2230	≤ 29	

Table 6: Unfolded data, with experimental resolution removed. The uncertainty in the measured energy is 40 keV.

CM.Energy(keV)	B.R.($10^{-9}/65\text{keV}$)	Error
1058	≤ 4.33	
1124	4.9	1.7
1189	4.3	1.2
1254	2.6	0.5
1319	2.1	0.8
1384	3.2	0.7
1448	4.8	0.6
1513	9.4	1.1
1577	17.2	1.7
1642	29.9	4.5
1706	49.6	6.5
1771	77.6	8.9
1835	118.7	11.4
1900	186.3	16.7
1964	282.0	19.3
2029	419.0	24.2
2093	625.9	31.2
2158	932.1	40.4
2222	1349.4	52.8
2287	1811.7	66.5
2352	2078.1	74.7
2416	1803.1	67.3
2481	1290.3	58.0
2546	808.6	41.5
2611	485.3	30.9
2676	291.6	24.8
2740	165.1	18.7
2805	91.4	14.0
2870	49.7	11.2
2935	28.9	10.7

Listed uncertainty are statistical only. Additional uncertainty in the yield of data points between $E= 1124 - 1254$ keV due to unfolding, is approximately $\pm 20\%$. The uncertainty at data point $E = 1319$ keV due to folding is larger. It can be smaller but not larger than the value shown.

References

- [Aj82] F. Ajzenberg-Selove. *Nuclear Physics*, A375(1982)1.
- [Aj84] F. Ajzenberg-Selove. *Nuclear Physics*, A413(1984)1.
- [Aj85] F. Ajzenberg-Selove. *Nuclear Physics*, A433(1985)1.
- [Ba71] F.C. Barker. *Aust. J. Phys.*, 24(1971)777.
- [Ba87] F.C. Barker. *Aust. J. Phys.*, 40(1987)25.
- [Ba91] F.C. Barker and T. Kajino. *Proc. Int. Workshop on Unstable Nuclei in Astrophysics, 7-8 June, 1991, Tokyo*. World Scientific, 1991.
- [Ba88] D. Baye and P. Descouvemont. *Nuclear Physics*, A481(1988)445.
- [Be68] H.A. Bethe. *Physics Today*, 21:9(1968)36.
- [Be85] H.A. Bethe and Gerald Brown. *Scientific American*, 252:5(1985)60.
- [Bl79] J.M. Blatt and V.F. Weisskopf. *Theoretical Nuclear Physics*. Dover Publications Inc. 1979.
- [Bo72] W. Bohne, J. Bommer, H. Fuchs, K.Grabisch, H.Kluge, and G. Röscher. *Nuclear Physics*, A196(1972)41.
- [Bo77] J.E. Bond and F.W.K. Firk. *Nucl. Phys.* A287(1977)317.
- [Br70] C. Brassard. Ph.D. thesis. Yale University. 1970.

- [Bu92] L. Buchmann, R.E. Azuma, C.A. Barnes, J.M. D'Auria, M. Dombsky, U. Giesen, K.P. Jackson, J.D. King, R.G. Korteling, P. McNeely, J. Powell, G. Roy, J. Vincent, T.R. Wang, S.S.M. Wong and P.R. Wrean. TRIUMF preprint.
- [Ca88] G.A. Caughlan and W.A. Fowler. *Atomic Data and Nuclear Data Tables*, 40(1988)238.
- [Ch84] S. Chandrasekhar. *Review of Modern Physics*, 56(1984)137.
- [Cl83] D. D. Clayton. *Principles of Stellar Evolution and Nucleosynthesis*. University of Chicago Press, 1983.
- [Cl68] G.J. Clark, D.J. Sullivan, and P.B. Treacy. *Nuclear Physics*, A110(1968)481.
- [Dy74] P. Dyer and C.A. Barnes. *Nuclear Physics*, A233(1974)495.
- [Fe92] H. Feshbach. *Theoretical Nuclear Physics*. J. Wiley and Sons, 1992.
- [Fo84] W. A. Fowler. *Review of Modern Physics*, 56(1984)149.
- [Ho54] F. Hoyle. *Astrophys. J. Suppl.*, 1(1954)121.
- [Hu76] J. Humblet, P. Dyer, and B.A. Zimmerman. *Nuclear Physics*, A271(1976)210.
- [Hu91] J. Humblet, B.W. Filippone, and S.E. Koonin. *Physical Review*, C44(1991)2530.

- [Ji90] X. Ji, B.W. Filippone, J. Humblet, and S.E. Koonin. *Physical Review*, C41(1990)1736.
- [Ji92] X. Ji. *private communication*.
- [Jo62] C.M. Jones, G.C. Phillips, R.W. Harris, and E.H. Beckner. *Nuclear Physics*, 37(1962)1.
- [Ke82] K.U. Kettner, H.W. Becker, L. Buchmann, J. Görres, H. Kräwinkel, C. Rolfs, P.Schmalbrock, H.P. Trautvetter, and A. Vlieks. *Z. Phys. A-Atomic and Nuclei*, 308(1982)73.
- [Ko74] S.E. Koonin, T.A. Tombrello, and G. Fox. *Nuclear Physics*, A220(1974)221.
- [Kr87] K.S. Krane. *Introductory Nuclear Physics*. John Wiley and Sons. 1987.
- [Kr88] R. M. Kremer, C.A. Barnes, K.H. Chang, H.C. Evans, B.W. Filippone, K.H. Hahn and L.W. Mitchell. *Physical Review Letters*, 60(1988)1475.
- [La58] A.M. Lane and R.G. Thomas. *Rev. Mod. Phys.*, 30(1958)257.
- [La83] K. Langanke and S.E. Koonin. *Nuclear Physics*, A410(1983)334.
- [La85] K. Langanke and S.E. Koonin. *Nuclear Physics*, A439(1985)384.
- [Ma69] P. Marmier and E. Sheldon. *Physics of Nuclei and Particles*. Academic Press, 1969.
- [Ne74] K. Neubeck, H. Schober, and H. Wäffler. *Physical Review*, C10(1974)320.

- [Ou92] J.M.L. Ouellet, H.C. Evans, H.W. Lee, J.R. Leslie, J.D. MacArthur, W. McLatchie, H.-B. Mak, P. Skensved, J.L. Whitton, and X. Zhao. *Physical Review Letters*, 69(1992)1896.
- [Pl87] R. Plaga, H.W. Becker, A. Redder, C. Rolfs, H.P. Trautvetter, and K. Langanke. *Nuclear Physics*, A465(1987)291.
- [Re87] A. Redder, H.W. Becker, C. Rolfs, H.P. Trautvetter, T.R. Donoghue, T.C. Rinckel, J.W. Hammer and K. Langanke. *Nuclear Physics*, A462(1987)385.
- [Sc77] D.N. Schramm and R.V. Wagoner. *Rev. Nucl. Sci*, 27(1977)37.
- [Te52] T. Teichmann and E.P. Wigner. *Phys. Rev.*, 87(1952)123.
- [To82] T.A. Tombrello, S.E. Koonin, and B.A. Flanders. In C.A. Barnes et al., editors, *Essays in Nuclear Astrophysics*, page 233, Cambridge University Press:New York, 1982.
- [Tr52] L.E. Trainor. *Phys. Rev.* 85(1952)962.
- [We92] T.A. Weaver and S.E. Woosley. *preprint*, 1992.
- [We74] D.C. Weisser, J.F. Morgan, and D.R. Tompson. *Nuclear Physics*, A235(1974)460.
- [Wi47] E. P. Wigner and L. Eisenbud. *Physical Review*, 72(1947)29.
- [Zh89] Z. Zhao, M. Gai, B.J. Lund, S.L. Rugari, D. Mikolas, B.A. Brown, J.A. Nolen, Jr., and M. Samuel. *Physical Review*, C39(1989)1985.

- [Zi77a] J.F. Ziegler. *Stopping powers and Range in all elements*. Volume 4, Pergamon Press, 1977.
- [Zi77b] J.F. Ziegler. *Stopping powers and Range in all elements*. Volume 3, Pergamon Press, 1977.
- [Zi91] J.F. Ziegler and J. Biersack *Code TRIM'91*.